
Doctoral Dissertations

Student Theses and Dissertations

Fall 2016

Development of implants composed of bioactive materials for bone repair

Wei Xiao

Follow this and additional works at: https://scholarsmine.mst.edu/doctoral_dissertations

 Part of the [Materials Science and Engineering Commons](#)

Department: Materials Science and Engineering

Recommended Citation

Xiao, Wei, "Development of implants composed of bioactive materials for bone repair" (2016). *Doctoral Dissertations*. 2549.

https://scholarsmine.mst.edu/doctoral_dissertations/2549

This thesis is brought to you by Scholars' Mine, a service of the Missouri S&T Library and Learning Resources. This work is protected by U. S. Copyright Law. Unauthorized use including reproduction for redistribution requires the permission of the copyright holder. For more information, please contact scholarsmine@mst.edu.

DEVELOPMENT OF IMPLANTS COMPOSED OF BIOACTIVE MATERIALS
FOR BONE REPAIR

by

WEI XIAO

A DISSERTATION

Presented to the Faculty of the Graduate School of the
MISSOURI UNIVERSITY OF SCIENCE AND TECHNOLOGY

In Partial Fulfillment of the Requirements for the Degree

DOCTOR OF PHILOSOPHY

in

MATERIALS SCIENCE AND ENGINEERING

2016

Approved by:

Mohamed N. Rahaman, Advisor

Richard K. Brow

Delbert E. Day

Mohsen Asle Zaeem

B. Sonny Bal

PUBLICATION DISSERTATION OPTION

The body of this dissertation has been compiled in the format for publication in peer-reviewed journals. Four papers have been included in the following order. The first paper, pages 3–29 was published in *Acta Biomaterialia* in 2013, Volume 9, Issue 9. The second paper, pages 30–52 was published in *Materials Science and Engineering: C* in 2016, Volume 60. The third paper, pages 53–84 was published in *Materials Science and Engineering: C* in 2016, Volume 68. The fourth paper, pages 85–109 has been submitted to the journal *B Materials Science and Engineering: C*.

One paper not included in the main body of the dissertation is given in the appendix. The paper, pages 113–134 was submitted to the *International Journal of Applied Ceramic Technology*.

ABSTRACT

The purpose of this Ph.D. research was to address the clinical need for synthetic bioactive materials to heal defects in non-loaded and loaded bone. Hollow hydroxyapatite (HA) microspheres created in a previous study were evaluated as a carrier for controlled release of bone morphogenetic protein-2 (BMP2) in bone regeneration. New bone formation in rat calvarial defects implanted with BMP2-loaded microspheres (43%) was significantly higher than microspheres without BMP2 (17%) at 6 weeks postimplantation. Then hollow HA microspheres with a carbonate-substituted composition were prepared to improve their resorption rate. Hollow HA microspheres with ~12 wt. % of carbonate showed significantly higher new bone formation ($73 \pm 8\%$) and lower residual HA ($7 \pm 2\%$) than stoichiometric HA microspheres ($59 \pm 2\%$ new bone formation; $21 \pm 3\%$ residual HA). The combination of carbonate-substituted hollow HA microspheres and clinically-safe doses of BMP2 could provide promising implants for healing non-loaded bone defects. Strong porous scaffolds of bioactive silicate (13-93) glass were designed with the aid of finite-element modeling, created by robocasting and evaluated for loaded bone repair. Scaffolds with a porosity gradient to mimic human cortical bone showed a compressive strength of 88 ± 20 MPa, a flexural strength of 34 ± 5 MPa and the ability to support bone infiltration in vivo. The addition of a biodegradable polylactic acid (PLA) layer to the external surface of these scaffolds increased their load-bearing capacity in four-point bending by ~50% and dramatically enhanced their work of fracture, resulting in a “ductile” mechanical response. These bioactive glass–PLA composites, combining bioactivity, high strength, high work of fracture and an internal architecture conducive to bone infiltration, could provide optimal implants for structural bone repair.

ACKNOWLEDGMENTS

I would like to thank my advisor, Dr. Mohammed N. Rahaman, for his support and guidance during my Ph.D. research and training. The assistance of Dr. Roger F. Brown, Department of Biological Sciences, with in vitro and in vivo experiments is greatly appreciated. I am grateful to members of my PhD advisory committee, Dr. Richard K. Brow, Dr. Delbert E. Day, Dr. Mohsen Asle Zaeem and Dr. B. Sonny Bal for their valuable comments and constructive suggestions during the course of my PhD research.

I would like to thank Dr. Yongxing Liu and Dr. Gregory E. Hilmas for helpful discussions. I would also like to thank Dr. Wenhai Huang (Tongji University, China) for introducing me to the idea of studying in the USA.

Several persons provided assistance to enable me to complete my research or provided guidance with the direction of my research, and I would like to express my thanks to them: Dr. Jeremy Watts, Clarissa Wisner and Ryan Grohsmeyer.

All of my colleagues and friends deserve many thanks as well. Dr. Xin Liu, Dr. Hailuo Fu, Dr. Qiang Fu, Yinan Lin, Youqu Shen, Sixie Huang, Dr. Lina Ma, Dr. Xiaoming Cheng, I greatly appreciated working and learning with you.

Last but not least, I would like to thank those who made this possible: my parents, Hong Xiao and Donglan Liu, and my wife, Yifei Gu. Their love, belief, and encouragement kept me moving forward in the journey of graduate study.

TABLE OF CONTENTS

	Page
PUBLICATION DISSERTATION OPTION	iii
ABSTRACT.....	iv
ACKNOWLEDGMENTS	v
LIST OF ILLUSTRATIONS.....	x
LIST OF TABLES.....	xvi
SECTION	
1. PURPOSE OF THIS DISSERTATION	1
PAPER	
I. Hollow hydroxyapatite microspheres: A novel bioactive and osteoconductive carrier for controlled release of bone morphogenetic protein-2 in bone regeneration....	3
ABSTRACT	3
1. Introduction	4
2. Materials and methods.....	5
2.1. Preparation and characterization of hollow HA microspheres	5
2.2. Loading the hollow HA microspheres with BMP2	7
2.3. Coating the BMP2-loaded microspheres with a biodegradable polymer	7
2.4. Measurement of BMP2 release profile in vitro	7
2.5. Animals and surgery.....	8
2.6. Histology.....	9
2.7. Histomorphometric analysis.....	9
2.8. Statistical analysis.....	10
3. Results	10
3.1. Characteristics of the as-prepared and PLGA-coated HA microspheres	10
3.2. BMP2 release profile in vitro	11
3.3. Bone regeneration in rat calvarial defects implanted with hollow HA microspheres	12
4. Discussion.....	13
4.1. Hollow HA microspheres as a carrier for BMP2	14
4.2. BMP2-loaded hollow HA microspheres as implants in bone regeneration	16
5. Conclusions	19

References	20
II. Preparation of resorbable carbonate-substituted hollow hydroxyapatite microspheres and their evaluation in osseous defects in vivo.....	30
ABSTRACT	30
1. Introduction	31
2. Materials and methods.....	33
2.1. Preparation and characterization of hollow HA microspheres	33
2.2. Degradation of hollow HA and CHA microspheres in vitro	34
2.3. Osteoclastic resorption of hollow HA and CHA microspheres in vitro	34
2.4. Animals and surgery.....	35
2.5. Histologic processing	36
2.6. Histomorphometric analysis.....	36
2.7. Statistical analysis.....	37
3. Results	37
3.1. Characteristics of converted microspheres	37
3.2. Solution mediated degradation in vitro.....	38
3.3. Cell mediated degradation in vitro	39
3.4. Bone regeneration in rat calvarial defects in vivo	39
4. Discussion.....	40
4.1. Properties of carbonate-substituted HA microspheres in vitro.....	41
4.2. Resorption of hollow microspheres and bone regeneration in vivo.....	42
5. Conclusions	44
References	45
III. Creation of bioactive glass (13-93) scaffolds for structural bone repair using a combined finite element modeling and rapid prototyping approach	53
ABSTRACT	53
1. Introduction	54
2. Materials and methods.....	56
2.1 Design of scaffold architecture	56
2.2 Finite element simulations.....	57
2.3 Experimental four-point bending and compression tests	59
2.4 Animal surgery.....	60

2.5 Histology and histomorphometric analysis	61
2.6 Statistical analysis.....	62
3. Results	63
3.1 Finite element simulation of four-point bending.....	63
3.2 Measured flexural strength of scaffolds in four-point bending	64
3.3 Finite element simulations and testing in compression	65
3.4 Assessment of bone regeneration	66
4. Discussion.....	67
4.1 FEM simulations.....	68
4.2 Measured flexural strength of scaffolds and validation of FEM simulations	70
4.3 Compressive strength and capacity to support bone infiltration	72
5. Conclusions	73
References	74
IV. Tough and strong porous bioactive glass–PLA composites for structural bone repair	85
ABSTRACT	85
1. Introduction	86
2. Materials and methods.....	88
2.1 Design of composite structures	88
2.2 Finite element simulations.....	89
2.3 Creation of bioactive glass–PLA composites	90
2.4 Measurement of bioactive glass–PLA adhesive strength.....	91
2.5 Mechanical testing in four-point bending.....	91
2.6 Statistical analysis.....	92
3. Results	92
3.1 Finite element simulations.....	92
3.2 Mechanical response of as-fabricated bioactive glass–PLA composites	93
4. Discussion.....	96
4.1 FEM simulations.....	96
4.2 Observed mechanical response of bioactive glass–PLA composites	97

4.3 Potential of bioactive glass composites for structural bone repair	100
5. Conclusions	101
References	102
SECTION	
2. CONCLUSIONS.....	110
3. SUGGESTIONS FOR FUTURE WORK.....	112
APPENDIX.....	113
VITA.....	135

LIST OF ILLUSTRATIONS

Figure Paper I	Page
Fig. 1. Low- and high-magnification SEM images of the surface of hollow HA microspheres as prepared (a, b), and after coating with solutions containing 50 mg ml ⁻¹ PLGA (c, d), and 200 mg ml ⁻¹ PLGA (e, f), followed by drying. The inset in (a) shows a cross-section of a hollow HA microsphere.	23
Fig. 2. (a) Amount of BMP2 released from hollow HA microspheres into a medium composed of equal volumes of FBS and PBS at selected time periods; (b) average cumulative amount of BMP2 released from the microspheres into the medium as a function of time. Data for the as-prepared microspheres (uncoated), and microspheres coated with 50 mg ml ⁻¹ PLGA solution (50 mg ml ⁻¹), and with 200 mg ml ⁻¹ PLGA solution (200 mg ml ⁻¹).	24
Fig. 3. (a, c) H&E and (b, d) von Kossa stained sections of rat calvarial defects implanted for 6 weeks with (a, b) as-prepared hollow HA microspheres (without BMP2) and (c, d) hollow HA microspheres loaded with BMP2 (1 µg per defect). HB = host (old) bone; NB = new bone.	25
Fig. 4. High-magnification images of H&E stained sections of rat calvarial defects implanted for 6 weeks with (a) as-prepared hollow HA microspheres (without BMP2) and (b) hollow HA microspheres loaded with BMP2 (1 µg per defect). The images shown in (a) and (b) correspond to the boxed area outlined in Fig. 3a and b, respectively. HB = host (old) bone; NB = new bone; red arrows indicate blood vessels; yellow arrows indicate bone marrow-like tissue.	26
Fig. 5. (a, c) H&E and (b, d) von Kossa stained sections of rat calvarial defects implanted for 6 weeks with hollow HA microspheres loaded with BMP2 and coated with different amounts of PLGA formed from solutions containing 50 mg ml ⁻¹ PLGA (a, b) and 200 mg ml ⁻¹ PLGA (c, d). HB = host (old) bone; NB = new bone.	27
Fig. 6. Box plot comparing the percent new bone formed in rat calvarial defects implanted for 3 weeks (3 W) and 6 weeks (6 W) with four groups of implants composed of hollow HA microspheres: (a) as prepared; (b) loaded with BMP2 (denoted BMP2/Uncoated); (c) loaded with BMP2 and coated using a 50 mg ml ⁻¹ PLGA solution (denoted BMP2/Coated(50)); (d) loaded with BMP2 and coated using a 200 mg ml ⁻¹ PLGA solution (denoted BMP2/Coated(200)). The median and mean values, interquartile range, and the high and low values for each group are shown. (n = 5; /P < 0.05).	28

Paper II

- Fig. 1. SEM images of the cross section of a hollow HA microsphere (a, b) and higher magnification images showing differences in surface morphology between the hollow HA and CHA12 microspheres (c, d). 48
- Fig. 2. (a) X-ray diffraction patterns and (b) FTIR spectra of the hollow HA, CHA9 and CHA12 microspheres. The pattern of a reference hydroxyapatite (HA JCPDS 72-1243) is also shown in (a). 48
- Fig. 3. (a) Cumulative amount of Ca^{2+} ion released from hollow HA, CHA9, and CHA12 microspheres into 0.1 M potassium acetate buffer solution (pH = 5.0; 37 °C) as a function of immersion time. (b) Amount of Ca^{2+} ions released from the three groups of microspheres after 1 h in the buffer solution. For comparison, the release of Ca^{2+} ions from a β -TCP reference material is also shown. (*significant difference between groups; $p < 0.05$). 49
- Fig. 4. SEM images of the surface of the HA, CHA9 and CHA12 microspheres after incubation with TIB-71 cells with added RANKL for 1 week (a1–3), and after the cells had been rinsed off (b1–3). (C: cells; P: pitted area after removal of cells)..... 49
- Fig. 5. Transmitted light images of (a, b) H&E stained sections of rat calvarial defects implanted with hollow CHA12 and HA microspheres without BMP2 at 12 weeks postimplantation; (c, d) higher magnification images of the boxed areas in a, b. (Arrowheads: edges of host bone; arrows: open microspheres)..... 50
- Fig. 6. Transmitted light images of (a, b) von Kossa and (c, d) H&E stained sections of rat calvarial defects implanted with hollow CHA12 and HA microspheres loaded with BMP2 at 12 weeks postimplantation; (e, f) higher magnification images of the boxed areas in c, d. (Arrowheads: edges of host bone)..... 51
- Fig. 7. New bone and residual amount of microspheres, as a percentage of the total defect area, in rat calvarial defects implanted with CHA12 and HA microspheres loaded with BMP2 at 12 weeks postimplantation. (*significant difference between groups; $p < 0.05$) 52

Paper III

- Fig. 1. The external shape and dimensions of the models used in FEM simulations of the flexural mechanical response. Each filament had a diameter of 330 μm and the thickness of the partially overlapped region between the filaments in adjacent layers was 90 μm 75

- Fig. 2. The external shape and structure of the models used in FEM simulations of the mechanical response in compression. The properties of the filaments were identical to those used for the simulations in flexure. The center-to-center distance (in μm) between adjacent filaments in each layer of one-half of each structure is shown below each model. 75
- Fig. 3. (a) Three-dimensional and (b) planar view of the four-point loading system used in the FEM simulations. The inner and outer spans were 10 mm and 20 mm, respectively, and the load was applied in a vertical direction (red arrow). 76
- Fig. 4. Shape and microstructure of scaffolds used for implantation in rat calvarial defects in vivo. The scaffolds, corresponding to the L1S1, L3S1 and L4S1 models in the FEM simulations, were 4.6 mm in diameter and 1.5 mm thick and were composed of 7 orthogonal layers of glass filaments. The center-to-center distance (in μm) between adjacent filaments in each layer of the scaffolds is shown on the right. 76
- Fig. 5. Typical deformation of the uniform grid-like (L1S1) model in flexure showing the magnitude and distribution of the stress in the filaments as determined by FEM simulations. The actual deformation of the model has been magnified by a scale factor of 30. The scale on the left gives the maximum principal stress corresponding to specific colors. 77
- Fig. 6. The magnitude and distribution of the tensile stress in the long filaments of the bottom layers of different models when subjected to the same applied load in four-point bending. The scale on the left gives the maximum principal stress corresponding to specific colors. 77
- Fig. 7. Highest tensile stress in the long filaments in the bottom layer of the models (normalized to the L1S1 model) determined from FEM simulations of four-point bending under an applied load of 100 N. The region of highest stress corresponded to the middle region of the bottom filaments between the inner span. 78
- Fig. 8. SEM images of the cross section perpendicular to the long filaments of as-fabricated 13-93 bioactive glass scaffolds with three different microstructures. Scale bar = 500 μm 78
- Fig. 9. (a) Measured load at failure and (b) flexural strength of as-fabricated 13-93 bioactive glass scaffolds with the microstructures shown, tested in four-point bending. 79

- Fig. 10. Weibull plots of the flexural strength data for 13-93 bioactive glass scaffolds with the L3S1 architecture (a) and L4S1 architecture (b). The straight line shows a least-squares fit to the data..... 79
- Fig. 11. SEM images of the fractured surfaces of the scaffolds with the L3S1 architecture (a-c) and L4S1 architecture (d-f) after testing in four-point bending. The plane (a, d) is approximately perpendicular to the direction of the long filaments. Higher magnification images of selected areas in (a), (d) are shown in (b, c) and (e, f). (Top: the side contacting inner span during the bending test; Bottom: the side contacting outer span; Stars: mirror region; M: mist region; H: hackle region; A: arrest line; arrow: crack origin; arrowheads: cantilever curls.) 80
- Fig. 12. Magnitude and distribution of the tensile stress in the filaments (parallel to xy plane) of different models when subjected to the same applied load in compression. The scale on the left gives the maximum principal stress corresponding to specific colors. 81
- Fig. 13. Measured compressive strength of as-fabricated 13-93 bioactive glass scaffolds with the microstructures corresponding to L1S1, L3S1 and L4S1. 81
- Fig. 14. Transmitted light images of H&E-stained sections (a1,b1,c1) and von Kossa-stained sections (a2,b2,c2) of rat calvarial defects implanted for 12 weeks with the three groups of bioactive glass scaffolds with microstructures corresponding to L1S1, L3S1 and L4S1. 82
- Fig. 15. Amount of new bone area determined as a percentage of the total defect area and the available pore are, and the total von Kossa positive area determined as a percentage of the total defect area, for rat calvarial defects implanted for 12 weeks with the three groups of scaffolds with microstructures corresponding to L1S1, L3S1 and L4S1. 82
- Paper IV
- Fig. 1. Three different structures of the glass scaffold analyzed in finite element modeling. Each structure had the external geometry of a beam and was composed of 6 layers of long (L) filaments in the y direction and 7 alternating short (S) filaments in the x direction. The inset under each structure shows the arrangement of the long filaments in the xz plane. 103
- Fig. 2. Cross section of composite composed of glass scaffold and adherent polymer (PLA) surface layer of thickness 200, 400 and 800 μm . The polymer layer was assumed to partially infiltrate the top and bottom surface of the scaffold. 104

- Fig. 3. Typical deformation of glass–polymer composite in four-point bending showing the magnitude and distribution of the stress in the glass filaments and polymer layer as determined by FEM simulations. The actual deformation of the model was magnified by a scale factor of 15 to better show the deformation. The scale on the left gives the maximum principal stress corresponding to specific colors. The box shows the region of most interest in the simulations..... 104
- Fig. 4. Magnitude and distribution of the tensile stress in the long filaments of the bottom layers of different models when subjected to the same applied load in four-point bending. The scale on the left gives the maximum principal stress corresponding to specific colors for each row. The designations of the models are given in Table I. 105
- Fig. 5. Highest tensile stress in the long filaments in the bottom layer of the models (normalized to the L1S1 model) determined from FEM simulations of four-point bending under an applied load of 100 N. The region of highest stress corresponded to the middle region of the bottom filaments between the inner span. 105
- Fig. 6. Magnitude and distribution of the tensile stress in the long filaments of the bottom layers of different models with polymer surface layers of thickness 200 or 800 μm and elastic modulus of 0.65, 2.1, 3.6 and 5.1 GPa when subjected to the same applied load in four-point bending. The scale on the left gives the maximum principal stress corresponding to specific colors..... 106
- Fig. 7. Stress vs. strain curves for PLA sheets of thickness 800 μm measured in tensile testing of dog-bone specimens (inset) at different deformation rates shown. The Young's modulus is also shown for each deformation rate. 106
- Fig. 8. Side view of as-fabricated composed of bioactive glass (13-93) scaffolds with a grid-like (L1S1) structure and adherent PLA surface layer of thickness (a) 200 μm ; (b) 400 μm ; (c) 800 μm 107
- Fig. 9. (a) Schematic diagram illustrating the fixture used in the adhesive strength test; (b) surface of PLA layer (previously in contact with the bioactive glass scaffold) after pullout test; (c) surface of bioactive glass scaffold after pullout test showing residual PLA adhering to the glass. The dashed lines in (b) outline grooves in the PLA layer which replicate the filaments (indicated by solid lines) at the surface of the glass scaffolds in (c)..... 107

- Fig. 10. Typical load vs. strain curves for bioactive glass (without PLA) and composites composed of bioactive glass (13-93) scaffolds with the different scaffold structures with different thickness of PLA coating. 108
- Fig. 11. Measured load at the first peak of the load vs. strain curves in four-point bending for different groups of bioactive glass scaffolds (L1S1, L3S1 and L4S1) and composites of these scaffolds with PLA surface layers of thickness 200, 400 or 800 μm . (* significant difference between groups; $p < 0.05$). 108
- Fig. 12. SEM images of bioactive glass–PLA composites (yz plane) after testing to specific strains in four-point bending. (a) Glass scaffold with the L1S1 structure and PLA layer thickness of 200 μm ; a magnified images of the boxed area in (a) is shown in (b). (c) Glass scaffold with the L4S1 structure and PLA layer thickness of 400 μm ; magnified images of the boxed areas in (c) are shown in (d) and (e). 109

LIST OF TABLES

Table	Page
Paper I	
Table I. Percentage of new bone (mean \pm SD) formed in rat calvarial defects implanted for 3 weeks and 6 weeks with four groups of hollow HA microspheres used in this study: microspheres without BMP2; microspheres with BMP2; BMP2-loaded microspheres coated with 50 mg ml ⁻¹ PLGA solution; BMP2-loaded microspheres coated with 200 mg ml ⁻¹ PLGA solution.	28
Table II. Comparison of percent new bone (mean \pm SD) formed in rat calvarial defects implanted with the hollow HA microspheres (106–150 μ m) used in this study, and with selected bioactive ceramic and glass implants.	29
Paper II	
Table I. Characteristics of hollow hydroxyapatite (HA) and carbonate-substituted hydroxyapatite (CHA) microspheres prepared by converting borate glass microspheres (150–250 μ m) in 0.02 M K ₂ HPO ₄ solution containing different concentrations of KHCO ₃ at 37 °C. Data for commercial β -TCP granules used as the control group are included for reference.	52
Paper III	
Table I. Summary of models analyzed in FEM simulations of the mechanical response in flexure. The models, with the shape of beams, were composed of alternating layers of long glass filaments (L) and short glass filaments (S) arranged orthogonally along the x and y axes. The designations LiSi are used to describe the different distribution of the filaments in the models. Each model was composed of 6 layers of long filaments and 7 layers of short filaments. All the models were composed of the same number of long filaments (48) and short filaments (259), except for the L4S1 model (66 long filaments and 259 short filaments). The cross section of the long filaments in the models is also shown. In addition, a model (S45°) with same porosity as L1S1, but with filaments at 45° to the x and y axes was also analyzed. The S45° model was composed of layers with different porosity as shown.	83
Table II. Geometrical parameters of the LiSi models (Table 1) analyzed in FEM simulations of the mechanical response in flexure. The center-to-center distance (μ m) between adjacent glass filaments in the each layer of the models is shown. In the S45° model, the center-to-center distance was 581 μ m and 1054 μ m, respectively, for the denser layers and more porous layers.	84
Paper IV	
Table I. Summary of models analyzed in FEM simulations.	109

SECTION

1. PURPOSE OF THIS DISSERTATION

The purpose of this Ph.D. research was to address the clinical need for synthetic bioactive materials to heal defects in non-loaded bone and structural (loaded) bone. The research focused on two areas:

(1) Creation and evaluation of biodegradable hollow hydroxyapatite (HA) microspheres that could serve as devices for local delivery of therapeutics to enhance healing of non-loaded bone defects;

(2) Design, creation and evaluation of bioactive silicate glass (13-93) scaffolds with suitable mechanical properties and internal architecture to heal large (critical-size) defects in structural bone.

Hydroxyapatite is the main inorganic constituent of human bone. Synthetic HA has several attractive properties as a scaffold material for bone regeneration. It is biocompatible, bioactive, and osteoconductive, with a proven ability to support bone regeneration and to bond to surrounding tissue. Previous studies in our research group determined the process variables for the preparation of hollow HA microspheres with controlled characteristics such as surface area, shell thickness and pore size of the shell. The ability of these hollow HA microspheres to serve as a device for controlled delivery of proteins such as bovine serum albumin was evaluated. In the present study, the ability of these hollow HA microspheres to release a potent growth factor, bone morphogenetic protein-2 (BMP2), and enhance bone healing in rat calvarial defects was studied. While bone regeneration was significantly improved, the HA microspheres themselves showed little ability to degrade. Ideally, implants for bone regeneration should degrade (or resorb) and remodel into bone. A follow-up study was undertaken to develop resorbable hollow HA microspheres. By modifying the process variables, hollow HA microspheres with the same geometry as those used previously but with a carbonate-substituted composition were prepared and evaluated in vitro and in vivo.

There is a need for synthetic biomaterials to heal large defects in structural bone because the available treatments based on the use of autogenous bone grafts, allografts and porous metals have limitations. Bioactive glass particles and weak scaffolds have been used to heal small contained bone defects but the development of bioactive glass

scaffolds with the requisite mechanical properties and internal architecture to heal large (critical size) defects in structural bone has been a challenge. Previous studies in our research group showed the ability to create strong porous bioactive silicate glass (13-93) scaffolds with a uniform grid-like microstructure using a robotic deposition technique. The scaffolds showed a compressive strength comparable to human cortical bone and a microstructure conducive to supporting bone infiltration in vivo. However, the flexural strength of the scaffolds was much lower than human cortical bone. As bending is an important loading mode in structural bone, a study was undertaken to improve the flexural strength of the scaffolds. Finite element modeling was used to re-design the scaffold architecture. Then 13-93 glass scaffolds with the optimal microstructures were created and evaluated in vitro and in vivo. Scaffolds created with a porosity gradient to mimic cortical bone showed a nearly 200% increase in flexural strength with no adverse effect on their compressive strength or ability to regenerate bone. However, the scaffolds still showed a brittle mechanical response typical of glass. Consequently, the addition of a biodegradable polymer layer to the external surface of the scaffold was studied as an approach to modify the brittle mechanical response of the glass scaffold. Composites formed from 13-93 glass scaffolds and adherent surface layers of polylactic acid (PLA) of varying thickness were created and tested to study their mechanical response in four-point bending.

I. Hollow hydroxyapatite microspheres: A novel bioactive and osteoconductive carrier for controlled release of bone morphogenetic protein-2 in bone regeneration

Wei Xiao ^a, Hailuo Fu ^a, Mohamed N. Rahaman ^a, Yongxing Liu ^a, B. Sonny Bal ^b

^a Department of Materials Science and Engineering, Missouri University of Science and Technology, Rolla, MO 65409, USA

^b Department of Orthopaedic Surgery, University of Missouri, Columbia, MO 65212, USA

ABSTRACT

The regeneration of large bone defects is a common and significant clinical problem. Limitations associated with existing treatments such as autologous bone grafts and allografts have increased the need for synthetic bone graft substitutes. The objective of this study was to evaluate the capacity of novel hollow hydroxyapatite (HA) microspheres to serve as a carrier for controlled release of bone morphogenetic-2 (BMP2) in bone regeneration. Hollow HA microspheres (106–150 μm) with a high surface area ($>100 \text{ m}^2 \text{ g}^{-1}$) and a mesoporous shell wall (pore size 10–20 nm) were created using a glass conversion technique. The release of BMP2 from the microspheres into a medium composed of diluted fetal bovine serum in vitro was slow, but it occurred continuously for over 2 weeks. When implanted in rat calvarial defects for 3 or 6 weeks, the microspheres loaded with BMP2 (1 μg per defect) showed a significantly better capacity to regenerate bone than those without BMP2. The amount of new bone in the defects implanted with the BMP2-loaded microspheres was 40% and 43%, respectively, at 3 and 6 weeks, compared to 13% and 17%, respectively, for the microspheres without BMP2. Coating the BMP2-loaded microspheres with a biodegradable polymer, poly(lactic-co-glycolic acid), reduced the amount of BMP2 released in vitro and, above a certain coating thickness, significantly reduced bone regeneration in vivo. The results indicate that these hollow HA microspheres could provide a bioactive and osteoconductive carrier for growth factors in bone regeneration.

1. Introduction

The regeneration of large bone defects resulting from trauma, malignancy or congenital diseases represents a common and significant clinical problem [1]. Autologous bone grafts are the gold standard for treatment because they possess all the ideal characteristics for bone growth: osteoconductivity, osteoinductivity and osteogenicity [1–3]. However, autografts suffer from problems such as donor site morbidity and limited supply [4–6]. Bone allografts are alternatives, but they are expensive and carry the risk of disease transmission and adverse host immune reaction. These problems associated with autografts and allografts have increased the need for synthetic bone graft substitutes.

A variety of synthetic bone graft substitutes have been developed over the last 30 years, including hydroxyapatite (HA), betatricalcium phosphate (β -TCP), biphasic calcium phosphate (BCP), calcium phosphate cements, bioactive glass and biodegradable polymers [1–3]. However, synthetic bone graft substitutes currently see limited use clinically because of their inferior in vivo performance when compared to autogeneous bone grafts [3]. Most synthetic bone grafts have a limited capacity to reconstitute bone in large defects because they lack the osteoinductivity and osteogenicity of autologous bone grafts.

The osteoinductive properties of bone morphogenetic proteins (BMPs) have been evaluated extensively both in vitro and in vivo [7,8]. Among the recombinant proteins, BMP2 and BMP7 have been tested in a number of orthopedic and dental applications, and they are now used clinically. Because direct injection of a growth factor in soluble form into a defect site is generally not effective for bone regeneration due to rapid diffusion away from the site, delivery is often provided through a carrier material. A wide range of materials in various forms such as particles, granules, sponges and porous three-dimensional (3-D) scaffolds have been tested as carriers for BMPs. They include biodegradable polymers, natural and synthetic, such as collagen and poly(lactic-co-glycolic acid) (PLGA), hydrogels and calcium phosphates such as HA and betatricalcium phosphate (β -TCP), as well as composites of these materials [8,9].

In the last few years, we have investigated the development of a hollow HA microsphere technology to meet the need for bone graft substitutes that could approach the combined osteoconductive, osteoinductive and osteointegrative properties of

autologous bone grafts. Hollow HA microspheres prepared by a novel glass conversion technique [10,11] have a high surface area ($>100 \text{ m}^2 \text{ g}^{-1}$) and a mesoporous shell wall (pore size = 10–20 nm) composed of nanocrystalline HA particles [12]. The hollow core and the mesopores can provide reservoirs for loading growth factors into the microspheres, while the shell wall can provide methods for controlled release by desorption and migration of the protein through the mesopores.

Our previous work showed that the hollow HA microspheres can be loaded with bovine serum albumin (BSA), used as a model protein, and that the microspheres could function as a carrier for controlled delivery of BSA into phosphate-buffered saline (PBS) or a poly(ethylene glycol) (PEG) hydrogel in vitro [13,14]. Our more recent work showed that loading the hollow HA microspheres with transforming growth factor beta 1 (TGF β 1) (5 μg per defect) can enhance bone regeneration in rat calvarial defects at 6 weeks but not at 12 weeks [15]. However, the amount of new bone formed in the defects implanted with the TGF-loaded microspheres was only ~20% of the total defect area after 6 or 12 weeks.

The objective of this study was to evaluate the capacity of the hollow HA microspheres to serve as a carrier for BMP2 in the regeneration of bone in an osseous defect model. BMP2 was used in the present study because of its more potent ability to stimulate bone formation when compared to TGF β 1 [16,17]. The use of a biodegradable polymer coating to modify the release of BMP2 from the microspheres was studied in vitro. Bone regeneration in rat calvarial defects implanted with the BMP2-loaded hollow HA microspheres was evaluated using histomorphometric techniques. The rat calvarial defect model was used because it is a standard inexpensive assay for evaluating new bone formation in an osseous defect [18].

2. Materials and methods

2.1. Preparation and characterization of hollow HA microspheres

Hollow HA microspheres were prepared by reacting solid glass microspheres in an aqueous phosphate solution as described in detail in our previous study [12]. Briefly, borate glass with the composition 15CaO, 11Li₂O, 74B₂O₃ (wt.%), designated CaLB3-15, was prepared by melting reagent grade CaCO₃, Li₂CO₃ and H₃BO₃ (Alfa Aesar, Haverhill, MA, USA) in a Pt crucible at 1200 °C for 45 min, and quenching the melt between cold

stainless steel plates. Particles of size 106–150 μm were obtained by grinding the glass in a hardened steel mortar and pestle, and sieving through 100 and 140 mesh sieves. Glass microspheres were obtained by dropping the crushed particles down a vertical tube furnace at 1000 °C [19]. Hollow HA microspheres were obtained by reacting the solid glass microspheres for 2 days in 0.02 M K_2HPO_4 solution at 37 °C and a starting pH = 9.0. In the conversion process, 1 g of glass microspheres was placed in 200 ml solution, and the system was gently stirred continuously. The converted microspheres were washed three times with distilled water, soaked in anhydrous ethanol to displace residual water and dried for at least 12 h at room temperature, then for at least 12 h at 90 °C.

Characterization of the converted microspheres was performed using the methods described in our previous studies [12–15]. Briefly, the microstructure of the surface and cross-section of the microspheres was examined using scanning electron microscopy (SEM; S4700; Hitachi, Tokyo, Japan). The phase composition of the converted microspheres (ground into a powder) was checked using X-ray diffraction XRD; D/mas 2550 v; Rigaku; The Woodlands, TX, USA) and Fourier transform infrared (FTIR) spectroscopy (NEXUS 670; Thermo Nicolet; Madison, WI, USA). XRD was performed using $\text{Cu K}\alpha$ radiation ($\lambda = 0.15406 \text{ nm}$) at a scan rate of $1.8^\circ \text{ min}^{-1}$ in the 2θ range 20–70°, while FTIR was performed in the wavenumber range 400–4000 cm^{-1} , (resolution = 8 cm^{-1}) on pellets pressed from a mixture of 2 mg powder and 198 mg KBr.

The carbon content of the microspheres was measured by a combustion technique at a commercial laboratory (LECO Corp., St Joseph, MI, USA) and used to determine the carbonate content of the microspheres.

The specific surface area of the microspheres and the pore size distribution of the shell wall were measured using nitrogen adsorption (Autosorb-1; Quantachrome, Boynton Beach, FL, USA). A mass of 300–500 mg of microspheres was weighed and evacuated for 15 h at 120 °C to remove adsorbed moisture; then the volume of nitrogen adsorbed and desorbed at different relative gas pressures was measured and used to construct adsorption-desorption isotherms. The first five points of the adsorption isotherm, which initially followed a linear trend implying monolayer formation of the adsorbate, were fitted to the Brunauer-Emmett-Teller (BET) equation to determine the specific surface area. The pore size distribution was calculated using the Barrett-Joiner-

Halenda (BJH) method applied to the desorption isotherm [20]. After they were loaded with BMP2 and after the conclusion of the BMP2 release experiments *in vitro* (described later), the dried microspheres were also characterized by SEM and the BET method using the procedures described above.

2.2. Loading the hollow HA microspheres with BMP2

After sterilization by soaking in anhydrous ethanol and drying in an incubator at 120 °C, some of the hollow HA microspheres were loaded with BMP2 (Shenandoah Biotechnology Inc., Warwick, PA, USA) and used to study the release profile of the BMP2 *in vitro*. A method described previously was used to load the microspheres with BMP2 [21,22]. Briefly, 10 mg of hollow HA microspheres were placed in a 1 ml centrifuge tube, and 10 μ l of BMP2 solution, formed by dissolving 10 μ g BMP2 in 100 μ l sterile citric acid (pH = 3.0), was pipetted onto the microspheres. A small vacuum was applied to the system to replace the air in the hollow HA microspheres with the BMP2 solution. The BMP2-loaded microspheres were dried overnight in a refrigerator at 4 °C and used immediately without further sterilization.

2.3. Coating the BMP2-loaded microspheres with a biodegradable polymer

The ability to modify the release profile of BMP2 from the hollow HA microspheres was studied by coating some of the BMP2-loaded microspheres with a biodegradable polymer, poly(DL-lactic- co-glycolic acid), PLGA (50/50; inherent viscosity = 0.17 dl g⁻¹; Birmingham Polymers, Inc., Birmingham, AL, USA). In the coating process, 20 μ l of a PLGA solution in chloroform was added to 10 mg hollow HA microspheres in a centrifuge tube, and the system was dried at 4 °C for 24 h. Two different concentrations of the PLGA solution (50 mg ml⁻¹ and 200 mg ml⁻¹) were used to form coatings with different thicknesses.

2.4. Measurement of BMP2 release profile in vitro

In measuring the release of BMP2 from the microspheres, 500 μ l of a sterile solution (pH = 7.4) composed of equal volumes of fetal bovine serum (FBS) and PBS was added to 10 mg microspheres (coated with PLGA or uncoated) in a micro-centrifuge

tube, and the samples were incubated at 37 °C. At selected times, the solution was removed as completely as possible for testing, and replaced with fresh solution. Control samples containing known amounts of BMP2 in the solution composed of FBS and PBS were also incubated at 37 °C. The amount of BMP2 present in the control samples was measured using an enzyme-linked immunosorbent assay (ELISA) kit (PeproTech, Rocky Hill, NJ, USA). The concentrations of the unknown samples were quantified relative to a BMP2 standard curve run on the same plate. Three samples of each group were tested at each time point, and the amount of BMP2 released was expressed as an average \pm standard deviation (SD).

2.5. Animals and surgery

All animal experimental procedures were approved by the Missouri University of Science and Technology Animal Care and Use Committee, in compliance with the NIH Guide for Care and Use of Laboratory Animals (1985). 25 Sprague Dawley rats (3 months old; 350 ± 30 g) were housed in the animal care facility and acclimated to diet, water and housing under a 12 h/12 h light/dark cycle. The rats were anesthetized with an intramuscularly injected mixture of ketamine and xylazine (0.15 μ l per 100 g). The surgical area was shaved, scrubbed with 70% ethanol, and then draped. With sterile instruments and an aseptic technique, a cranial skin incision was sharply made in an anterior-to-posterior direction along the midline. The subcutaneous tissue, musculature and periosteum were dissected and reflected to expose the calvarium. Bilateral full-thickness defects 4.6 mm in diameter were created in the central area of each parietal bone using a trephine (4.6 mm outer diameter) attached to an electric drill. The sites were constantly irrigated with sterile PBS to prevent overheating of the bone margins and to remove the bone debris.

The calvarial defects were implanted with four groups of implants composed of hollow HA microspheres:

- (1) hollow HA microspheres (positive control);
- (2) hollow microspheres loaded with BMP2 (1 μ g per defect);
- (3) hollow microspheres loaded with BMP2 (1 μ g per defect) and coated with PLGA (50 mg ml⁻¹);

(4) hollow microspheres loaded with BMP2 (1 lg per defect) and coated with PLGA (200 mg ml⁻¹).

The defects were randomly implanted with five implants per group, but mixing of the implants with and without BMP2 was avoided in the same animal. Defects left empty served as the negative control group. The hollow HA microspheres without BMP2 and the unfilled defects were randomly assigned to ten animals, while the three groups of microspheres loaded with BMP2 were randomly assigned to 15 animals. Each animal received an intramuscular injection of ~200 µl penicillin and ~200 µl buprenorphine post-surgery. The animals were monitored daily for condition of the surgical wound, food intake, activity and clinical signs of infection. After 3 or 6 weeks, the animals were sacrificed by CO₂ inhalation, and the calvarial defect sites with surrounding bone and soft tissue were harvested.

2.6. Histology

The calvarial samples consisting of the defect sites with surrounding bone and soft tissue were washed with PBS and fixed in 10% formalin solution for 5 days. The fixed tissue samples were each cut transversely in half; half of each sample was for paraffin embedding and the other half for methyl methacrylate embedding. The samples for paraffin sections were decalcified for 4 weeks in EDTA (14 wt.%) under mild agitation on a rocking plate. After the samples were dehydrated in ethanol and embedded in paraffin using standard histological techniques, 5 µm thick sections were cut and stained with hematoxylin and eosin (H&E) [23]. The undecalcified samples were dehydrated through a graded series of ethanol solutions, and embedded in methyl methacrylate. Sections were ground to a thickness of 30–40 µm using a micro-grinding system (EXAKT 400CS, Norderstedt, Germany), and stained using the von Kossa technique to observe mineralization [24].

2.7. Histomorphometric analysis

Stained sections were examined in a transmitted light microscope (Model BX51; Olympus America, Center Valley, PA, USA) fitted with a digital color camera (Model DP71; Olympus). Images were analyzed on a computer using the ImageJ software

(National Institutes of Health, USA). Sections stained with H&E were used to analyze the percentage of new bone formed within the defect. The newly formed bone was identified by outlining the edge of the defect, with the presence of original and new bone being identified by lamellar and woven bone, respectively. The total defect area was measured from one edge of the old calvarial bone, including the entire implant and tissue within it, to the other edge of the old bone. The newly formed bone within this area was then outlined and measured; the amount of new bone was expressed as a percentage of the total defect area.

2.8. Statistical analysis

Measurements ($n = 5$) of the percentage of new bone were expressed as a mean \pm SD. Analysis for differences between groups was performed using one-way analysis of variance (ANOVA) with Tukey's post hoc test; differences were considered significant for $P < 0.05$.

3. Results

3.1. Characteristics of the as-prepared and PLGA-coated HA microspheres

SEM images of the surface of the as-prepared microspheres are shown in Fig. 1a and b. Examination of the cross-section of the microspheres in the SEM confirmed that they were hollow (Fig. 1a, inset). As prepared, the hollow microspheres (external diameter = 106–150 μm) had a surface area of $102 \pm 5 \text{ m}^2 \text{ g}^{-1}$, a hollow core equal to 0.6 the microsphere diameter and a mesoporous shell wall (pore size = 10–20 nm). SEM examination and the BET method did not show any measurable differences in the microstructure and surface area of the microspheres after loading with BMP2 or after the conclusion of the BMP2 release experiments in vitro at 14 days.

The X-ray and FTIR patterns of the as-prepared microspheres were similar to those described in our previous work [12], confirming that the microspheres were composed of HA. The patterns are omitted for the sake of brevity. Briefly, the XRD patterns showed broad peaks at 2θ values which corresponded to those of a reference HA (JCPDS 72-1243). The broad peaks indicated that the HA was composed of nanometer-

sized crystals, which is consistent with the fine, needle-like particles seen in the SEM image (Fig. 1b).

The most dominant resonances in the FTIR spectrum were the phosphate ν_3 resonance, centered at $\sim 1040\text{ cm}^{-1}$, and the phosphate ν_4 resonance, with peaks at ~ 605 and 560 cm^{-1} , which are associated with crystalline HA. The FTIR spectrum also showed a weak C–O resonance at $1420\text{--}1460\text{ cm}^{-1}$ corresponding to the $(\text{CO}_3)^{2-}$ group substituting for $(\text{PO}_4)^{3-}$ in HA [25], which resulted presumably from CO_2 dissolved in the aqueous medium used in the glass conversion process. The carbonate content of the HA microspheres determined using a combustion technique described earlier was 2.1 wt.%.

SEM images of the hollow HA microspheres after they were coated with a solution composed of 50 mg ml^{-1} or 200 mg ml^{-1} PLGA are shown in Fig. 1c–f. The microspheres coated with the 50 mg ml^{-1} PLGA solution consisted of aggregates bonded at their contact areas by the PLGA (Fig. 1c). The distribution of the PLGA coating on the surface of the microspheres was inhomogeneous, with no observable coating on some parts of the surface (Fig. 1d). When coated with the more concentrated PLGA solution (200 mg ml^{-1}), a larger amount of PLGA was apparent at the necks between the particles in the aggregates, and higher-magnification SEM images showed that a larger surface area of microspheres was coated with a thicker layer (Fig. 1e and f).

3.2. BMP2 release profile *in vitro*

The amount of BMP2 released at selected time points from the as-prepared and PLGA-coated HA microspheres into a medium composed of FBS and PBS is shown in Fig. 2a. As described earlier, at each time point, the medium was removed as completely as possible and fresh medium was added. The data were used to determine the cumulative amount of BMP2 released into the medium as a function of time (Fig. 2b). The uncoated microspheres showed an initial “burst” release at 1 h, followed by a more continuous release at longer times. In comparison, there appeared to be a delay in the release of BMP2 from the microspheres coated with the 50 mg ml^{-1} PLGA solution. The average amount of BMP released from the coated microspheres at 1 h was significantly smaller than that for the uncoated microspheres, but it became higher at day 1 and day 3 (Fig. 2a). Thereafter, the average amount of BMP2 released was lower or comparable to that for the

uncoated microspheres. The average amount of BMP released from the microspheres coated with the thicker PLGA solution (200 mg ml^{-1}) at 1 h was significantly lower than that for the uncoated microspheres, and the amount released into the medium remained low thereafter.

The average cumulative amount of BMP-2 released into the medium at any time decreased with increasing concentration of the PLGA coating solution (Fig. 2b). When the release experiments were terminated after 14 days, the cumulative amount of BMP-2 released from the three groups of microspheres into the medium, determined as a fraction of the amount initially loaded into the microspheres, was 1.8%, 1.5% and 1.0%, respectively, for the as-prepared microspheres, the microspheres coated with the 50 mg ml^{-1} solution and the microspheres coated with the 200 mg ml^{-1} solution.

3.3. Bone regeneration in rat calvarial defects implanted with hollow HA microspheres

Fig. 3 shows H&E and von Kossa stained sections of rat calvarial defects implanted for 6 weeks with the hollow HA microspheres without and with BMP2. New bone growth in the defects implanted with the microspheres without BMP2 was limited ($17 \pm 10\%$), and occurred mainly at the periphery with the host (old) bone (Fig. 3a and b). In comparison, new bone formation in the defects implanted with the BMP2-loaded microspheres was markedly greater ($43 \pm 6\%$), and the new bone bridged the defect within the 6 week implantation period (Fig. 3c and d).

Higher-magnification images of the boxed areas in the H&E stained sections in Fig. 3 showed limited new bone formation in the pore space between the microspheres without BMP2 (Fig. 4a). Instead, most of the pore space was filled with fibrous tissue that contained some blood vessels (red arrow). It appeared that fibrous tissue also infiltrated the hollow cores of the microspheres.

In comparison, along with the considerable amount of new bone in the pore space between the BMP2-loaded microspheres (Fig. 4b), blood vessels (red arrow) and bone marrow-like tissue (yellow arrow) were also present in the new bone.

Von Kossa and H&E stained sections of the defects implanted for 6 weeks with BMP2-loaded hollow HA microspheres that were coated with PLGA are shown in Fig. 5. For the microspheres coated with the less concentrated solution (50 mg ml^{-1} PLGA),

considerable new bone ($46 \pm 8\%$) was formed in the defects, and it almost completely bridged the defect. In comparison, for the microspheres coated with the more concentrated solution (200 mg ml^{-1} PLGA), the amount of new bone formed in the defects was significantly lower ($19 \pm 13\%$). New bone infiltrated the periphery (edge) of the implants and also formed on the dural (bottom) size.

Since considerable new bone formation was observed at 6 weeks in the defects implanted with the BMP2-loaded microspheres, uncoated or coated with the 50 mg ml^{-1} PLGA solution, an implantation time of 3 weeks was also used to examine the time-dependence of the new bone formation. The von Kossa and H&E stained sections are omitted for the sake of brevity. In general, for the same group of implants, the stained sections at 3 weeks did not show a marked difference from those at 6 weeks.

A box plot of the percent new bone formed in the defects implanted with the four groups of HA microspheres at 3 and 6 weeks is shown in Fig. 6; the data for the mean \pm SD are summarized in Table I. For each group, the average percent new bone increased from 3 weeks to 6 weeks, but the difference was not significant. The results also showed that new bone formation in the defects implanted with the BMP2-loaded implants, either uncoated or coated with the 50 mg ml^{-1} PLGA solution, was significantly higher than in the implants without BMP2 or the BMP2-loaded implants coated with the 200 mg ml^{-1} PLGA solution. The amount of new bone formed in the BMP2-loaded implants coated with the 200 mg ml^{-1} PLGA solution was not significantly different from that for the implants without BMP2.

4. Discussion

With a hollow core, high surface area and a mesoporous shell wall, the HA microspheres used in this study could provide a novel growth factor carrier that is bioactive and osteoconductive. BMP2 is a potent growth factor for stimulating bone formation, but it is limited by high cost and increasing concerns about adverse biological effects associated with the use high doses [26,27]. Consequently, the ability to control the sustained release of BMP-2 at clinically desirable rates is relevant in bone regeneration. The feasibility of combining the hollow HA microspheres with a biodegradable polymer coating to control the release profile of BMP2 was shown. This study also showed that

when loaded with BMP2, the hollow HA microspheres had a considerable capacity to regenerate bone in vivo, despite a slow and limited capacity to release BMP2 in vitro.

4.1. Hollow HA microspheres as a carrier for BMP2

The results showed that BMP2 was released continuously but slowly from the hollow HA microspheres into the medium in vitro (Fig. 2b). BMP2 has a high affinity for HA and, consequently, its release rate from HA in vitro is often low. The adsorbed BMP2 is reported to be strongly immobilized on the surface of the HA by electrostatic and other interactions, such as hydrogen bonding [28]. This strong interaction makes it difficult for the BMP2 to be displaced from the HA surface by competitive adsorption from other proteins [29]. In one study, 23% of the BMP2 initially adsorbed on a nanostructured HA coating was released at 21 days, but the release rate was almost doubled from a coarse-grained HA coating [30]. In another study, after an initial release of 22% within the first 24 h, subsequent release of BMP2 from a porous calcium phosphate cement was limited [29]; the addition of a carrier protein, BSA, had little effect on the BMP2 release profile.

While there is a tendency for low release of BMP2 from calcium phosphate bioceramics in vitro, the amount released from the hollow HA microspheres used in this study was still lower than those observed from more conventional HA materials [29,30]. A few factors might have contributed to the much lower release rate, but the unique structural features of the hollow HA microspheres, such as the high-surface-area mesoporous shell, might be the most important. The theoretical amount of BMP2 that can be adsorbed onto the surface of HA has been estimated to be $\sim 800 \mu\text{g m}^{-2}$ [30]. The specific surface area of the hollow HA microspheres used in this study was $\sim 100 \text{ m}^2 \text{ g}^{-1}$. Consequently, $\sim 800 \mu\text{g}$ of BMP-2 could theoretically be adsorbed on the surface of the 10 mg of HA microspheres used in these experiments. Since the total amount of BMP2 initially loaded into the hollow HA microspheres was 1 μg , therefore a large amount of the HA surface area would remain available for adsorption. Presumably the desorbed BMP2 could be readily re-adsorbed on the largely free HA surface, which would markedly reduce the amount of BMP2 released into the medium. Furthermore, the tortuous mesopores of the shell wall could make migration of BMP2 from the hollow

core or from the pores to the external surface of the microspheres difficult because of the large surface area available for adsorption.

Other factors that could also contribute to the limited amount BMP2 released in vitro are the limited flow of the liquid media used in the release experiments, and the tendency of the microspheres to aggregate. However, a higher release rate of BMP2 from the microspheres can be expected in vivo because of a higher degradation rate of the HA due to cell-mediated degradation in addition to dissolution-mediated degradation [31,32] and the higher solubility of proteins in vivo. If required, the release of BMP2 from the as-prepared microspheres can be improved by increasing the dissolution or degradation rate of the HA [28–30], which is dependent on the composition and structure of the HA [33,34]. The HA microspheres used in the present study had a nearly stoichiometric composition and, consequently, a low degradation rate. As described earlier, no measurable degradation of the microspheres was observed after the two-week BMP2 release experiments in vitro. Our previous experiments showed no measurable degradation of the microspheres at 12 weeks in rat calvarial defects [15]. In our ongoing experiments, hollow HA microspheres with varying amounts of carbonate substitution are being prepared by a similar glass conversion process and they are being evaluated in vitro and in vivo.

The rate at which the BMP2 is released with time is also relevant in the use of these hollow HA microspheres as a carrier in bone regeneration. In particular, a high initial burst release of BMP2 has often been observed from HA carrier materials [35]. A burst release of BMP2 can induce inflammatory reactions which are believed to be beneficial for promoting bone formation, but it can also cause significant adverse biological effects. While a reduction in the BMP2 dose delivered in vivo could reduce those side effects, a high dose is often required to induce significant bone formation [26,36].

In order to test the ability to modify the BMP2 release rate, the hollow HA microspheres were coated with PLGA after they were loaded with BMP2. PLGA solutions with two different concentrations (50 mg ml^{-1} and 200 mg ml^{-1}) were used to control the thickness or the amount of the PLGA deposited on the microspheres. It is expected that the PLGA could reduce the size of the mesopores in the shell wall of the

microspheres or completely block the pores, depending on the concentration of the coating solution. Consequently, the initial release of any unadsorbed BMP-2 from the microspheres would be impeded.

The results showed that both coatings were effective in reducing the amount of BMP2 released during the first hour when compared to the uncoated microspheres (Fig. 2a); the amount of BMP2 released from the coated microspheres was 4–5 times lower than that for the uncoated microspheres. Subsequently, the amount of BMP2 released from the microspheres coated with the 50 mg ml⁻¹ PLGA solution increased, and the cumulative amount of BMP2 released was not significantly different from that of the uncoated microspheres (Fig. 2b). In comparison, the amount of BMP2 released from the microspheres coated with the 200 mg ml⁻¹ solution remained at a much lower value, presumably because the larger PLGA coverage provided a greater barrier to the release of BMP2.

The results showed the feasibility of combining the hollow HA microspheres with a biodegradable polymer coating to control the release profile of BMP2. However, it is expected that optimization of the coating will depend on the clinical application. For example, the use of a much higher BMP2 dose (1500 µg ml⁻¹), as in some clinical applications [37], will require the coating thickness to be adjusted accordingly in order to achieve optimum control on the release profile.

4.2. BMP2-loaded hollow HA microspheres as implants in bone regeneration

The in vivo experiments showed the effectiveness of using the hollow HA microspheres as a carrier to deliver BMP2 in the stimulation of bone regeneration. Loading the microspheres with BMP2 significantly enhanced new bone formation in the rat calvarial defects at 3 weeks and the amount of new bone did not change significantly at 6 weeks (Fig. 6). This indicates that the BMP2-induced new bone formation was almost completed as early as 3 weeks, although bone remodeling could continue thereafter. As the pore space between the microspheres was almost completely infiltrated with new bone at 3 weeks, there was little opportunity for a significant further increase at 6 weeks.

An interesting observation was the effect of the PLGA coating on the capacity of the BMP2-loaded microspheres to regenerate bone. New bone formation in the implants coated with the PLGA solution of lower concentration (50 mg ml^{-1}) was not significantly different from that in the uncoated implants whereas new bone formation in the implants coated with the PLGA solution of higher concentration (200 mg ml^{-1}) was significantly lower (Fig. 6). In fact, the percent new bone formed in the BMP2-loaded implants coated with the 200 mg ml^{-1} PLGA solution was comparable to that for the microspheres without BMP2. The reason for the difference in bone generation among the uncoated and coated implants loaded with BMP is not clear at present and it is the subject of ongoing studies. However, a few factors that could contribute to the difference are briefly discussed at this stage.

The BMP2 release profiles in vitro showed that while the average BMP2 release rate (amount per period) was fairly similar among the three groups of microspheres after 3 days, there appeared to be more pronounced differences at earlier times (Fig. 2a). A possible explanation therefore is that differences in the initial release within the first 3 days could be responsible for the differences in new bone formation in the three implant groups loaded with BMP2. The cumulative amount of BMP2 released from the uncoated microspheres and the microspheres coated with the 50 mg ml^{-1} solution ($8\text{--}10 \text{ }\mu\text{g}$) was more than twice the value ($\sim 4 \text{ }\mu\text{g}$) for microspheres coated with the 200 mg ml^{-1} solution. The higher dose of BMP2 in the defect site released in the initial time period from the uncoated microspheres and the microspheres coated with the 50 mg ml^{-1} PLGA solution might have reached the threshold value to trigger the repairing cascades. In comparison, the lower BMP2 dose released from the microspheres coated with the 200 mg ml^{-1} PLGA solution might have been below the threshold value. The time at which exogenous BMP2 is administered can be critical. In a previous study [38], the administration of BMP2 at day 0 or day 4 post-fracture was found to enhance periosteal callus formation, bone mineral content, and biomechanical properties when compared to later administration of BMP2 (day 8).

Another factor that could contribute to the difference in bone regeneration among the BMP2-loaded implants is the modification of the surface properties of the HA by the PLGA coating. As described earlier, the coating produced by the 50 mg ml^{-1} PLGA

solution was inhomogeneous and mainly concentrated at the necks between the microspheres, leaving a large area of the microsphere surface uncoated (Fig. 2c and d). The microspheres could still provide a large area of osteoconductive surface for bone regeneration. This, combined with the release of BMP2, apparently did not reduce the capacity of the coated microspheres to regenerate bone. In comparison, a larger fraction of the microsphere surface was coated with the 200 mg ml⁻¹ PLGA solution (Fig. 2e and f), which markedly reduced the osteoconductive surface area. The slow release of BMP2 from the microspheres presumably compensated for the reduction in osteoconductive surface area, resulting a similar capacity to regenerate bone as the uncoated microspheres without BMP2 (Fig. 6).

It is also possible that the coating process could reduce the bioactivity of the BMP2 in the microspheres. At 14 days when the in vitro release experiments were concluded, the difference in the cumulative amount of BMP2 released from the microspheres coated with the 50 mg ml⁻¹ and the 200 mg ml⁻¹ solution was small (1.5% vs. 1.0%). A greater reduction in the bioactivity of the BMP2 released from the microspheres coated with the more concentrated solution could contribute to the significantly lower bone regeneration in those implants.

Another possible explanation for the difference in bone regeneration among the BMP2-loaded implants might be the critical role played by the immobilized BMP2 in bone repair (when compared to the released BMP2). It has been suggested that BMPs immobilized in extracellular matrices are essential for the osteoblastic differentiation of cells [39]. The BMP2 in the uncoated microspheres or the microspheres coated with 50 mg ml⁻¹ PLGA solution was presumably able to interact with cells. In comparison, the thicker coating on the microspheres coated with the 200 mg ml⁻¹ PLGA solution presumably made the BMP2 in those microspheres inaccessible to the cells. Further studies are required to elucidate the mechanism.

Table II gives a comparison of the amount of new bone formed in rat calvarial defects implanted with the hollow HA microspheres (with or without BMP2) used in this study and with a variety of biomaterials implanted in the same animal model. This list is not meant to be exhaustive; instead it provides data for a few selected bioactive materials: hollow HA microspheres, similar to those used in this study, loaded with TGFb1 (5 µg

per defect) [15]; particles (150–250 μm) of silicate 45S5 bioactive glass [40]; 3-D scaffolds of a borate bioactive glass (designated 13-93B3) with a microstructure similar to dry human trabecular bone [41]; 3-D scaffolds of a calcium-deficient HA (CDHA) without or with BMP2 (2 μg per defect) [42]; and 3-D scaffolds of a commercial biphasic calcium phosphate (BCP) without or with BMP2 (2.5 μg per defect) [43]. Silicate 45S5 glass is included in this comparison because it is considered to be the gold standard for bioactive glasses, whereas the 13-93B3 bioactive glass scaffolds are receiving interest for bone repair applications. In common with the HA used in the present study, the CDHA and BCP are calcium phosphate biomaterials.

For implants composed of the hollow HA microspheres used in this study, the data show that BMP2 is considerably more effective in stimulating new bone formation than TGF β 1. The data also indicate that the hollow HA microspheres loaded with BMP2 have a greater capacity to regenerate bone when compared to silicate 45S5 bioactive glass particles and porous scaffolds of borate 13-93B3 bioactive glass. The hollow HA microspheres also showed a better capacity to regenerate bone at 6 weeks when compared to highly porous scaffolds of the CDHA implanted for 8 weeks; when loaded with BMP2, the microspheres also showed a better capacity to regenerate bone than the CDHA scaffolds loaded with twice the amount of BMP2. New bone formation in the defects implanted with the hollow HA microspheres (without BMP2) for 6 weeks was comparable to that in highly porous commercial BCP scaffolds at 8 weeks. When loaded with BMP2, new bone formation in the BCP scaffolds was higher than that in the BMP2-loaded hollow HA microspheres. However, the implantation time was longer and the BMP2 loading was 2.5 times the amount used in the present work.

5. Conclusions

Hollow HA microspheres with a high-surface-area mesoporous shell wall can provide a potential novel carrier for BMP2 in bone regeneration. The capacity of the microspheres to deliver BMP2 in vitro was shown, although the amount of BMP2 released into the medium was small (1.8% after 2 weeks). The release of BMP2 from the hollow HA microspheres, particularly at early times, can be reduced and controlled by coating the microspheres with different amounts of a biodegradable polymer, PLGA,

indicating the feasibility of controlling the initial burst release of BMP2 typically observed from HA implants. When loaded with BMP2 (1 μg per defect), the hollow HA microspheres, uncoated or coated with a 50 mg ml^{-1} PLGA solution, significantly enhanced bone regeneration in rat calvarial defects within 3–6 weeks. Bone regeneration in those two groups of BMP2-loaded HA microspheres was considerably higher than in 45S5 glass particles (150–250 μm), the gold standard of bioactive glasses.

References

- [1] Giannoudis PV, Dinopoulos H, Tsiridis E. Bone substitutes: an update. *Injury* 2005;36S:S20–37.
- [2] Moore WR, Graves SE, Bain GI. Synthetic bone graft substitutes. *ANZ J Surg* 2001;71:354–61.
- [3] Laurencin C, Khan Y, El-Amin SF. Bone graft substitutes. *Expert Rev Med Devices* 2006;3:49–57.
- [4] Fernyhough JC, Schimandle JJ, Weigel MC. Chronic donor site pain complicating bone graft harvesting from the posterior iliac crest for spinal fusion. *Spine* 1992;17:1474–80.
- [5] Perry CR. Bone repair techniques, bone graft and bone graft substitutes. *Clin Orthop Relat Res* 1999;360:71–86.
- [6] Fleming JE, Cornell CN, Muschler GE. Bone cells and matrices in orthopedic tissue engineering. *Orthop Clin North Am* 2000;31:357–74.
- [7] Devescovi V, Leonardi E, Ciapetti G, Cenni E. Growth factors in bone repair. *Chir Organi Mov* 2008;92:161–8.
- [8] Kirker-Head CA. Potential applications and delivery strategies for bone morphogenetic proteins. *Adv Drug Deliv Rev* 2000;43:65–92.
- [9] Babensee JE, McIntire LV, Mikos AG. Growth factor delivery for tissue engineering. *Pharm Res* 2000;17:497–504.
- [10] Day DE, Conzone SA. Method for preparing porous shells or gels from glass particles. US Patent No. 6,358,531, March 19, 2002.
- [11] Conzone SD, Day DE. Preparation and properties of porous microspheres made from borate glass. *J Biomed Mater Res A* 2009;88:531–42.
- [12] Fu H, Rahaman MN, Day DE, Fu Q. Effect of process variables on the microstructure of hollow hydroxyapatite microspheres prepared by a glass conversion method. *J Am Ceram Soc* 2010;93:3116–23.
- [13] Fu H, Rahaman MN, Day DE, Brown RF. Hollow hydroxyapatite microspheres as a device for controlled delivery of proteins. *J Mater Sci Mater Med* 2011;22:579–91.

- [14] Fu H, Rahaman MN, Brown RF, Day DE. Evaluation of BSA protein release from hollow HA microspheres into PEG hydrogel. *Mater Sci Eng C* 2013;33:2245–50.
- [15] Fu H, Rahaman MN, Brown RF, Day DE. Evaluation of bone regeneration in implants composed of hollow HA microspheres loaded with transforming growth factor 1 in a rat calvarial defect model. *Acta Biomater* 2013;9:5718–9.
- [16] Liberman JR, Daluiski A, Einhorn TA. The role of growth factors in the repair of bone. *J Bone Joint Surg Am* 2002;84:1032–44.
- [17] Ruhé P, Kroese-Deutman H, Wolke J, Spauwen P, Jansen J. Bone inductive properties of rhBMP-2 loaded porous calcium phosphate cement implants in cranial defects in rabbits. *Biomaterials* 2004;25:2123–32.
- [18] Wang J, Glimcher MJ, Mah J, Zhou HY, Salih E. Expression of bone microsomal casein kinase ii, bone sialoprotein, and osteopontin during the repair of calvarial defects. *Bone* 1998;22:621–8.
- [19] Day DE, White JE, Brown RF, McMenamin KD. Transformation of borate glasses into biologically useful materials. *Glass Technol* 2003;44:75–81.
- [20] Barrett EP, Joyney LG, Halenda PP. The determination of pore volume and area distributions in porous substances I: computations from nitrogen isotherms. *J Am Chem Soc* 1951;73:373–80.
- [21] Nandi SK, Kundu B, Basu D. Protein growth factors loaded highly porous chitosan scaffold: a comparison of bone healing properties. *Mater Sci Eng C* 2013;33:1267–75.
- [22] Van de Watering FCJ, Molkenboer-Kuenen JDM, Boerman OC, van den Beucken JJJP, Jansen JA. Differential loading methods for BMP-2 within injectable calcium phosphate cement. *J Control Release* 2012;164:283–90.
- [23] Feng JQ, Zhang J, Dallas SL, Lu Y, Chen S, Tan X, et al. Dentin matrix protein 1, a target molecule for Cbfa1 in bone, is a unique bone marker gene. *J Bone Miner Res* 2002;17:1822–31.
- [24] Bonewald LF, Harris SE, Rosser J, Dallas MR, Dallas SL, Camacho NP, et al. Von Kossa staining alone is not sufficient to confirm that mineralization in vitro represents bone formation. *Calcif Tissue Int* 2003;72:537–47.
- [25] Vignoles M, Bonel G, Holcomb DW, Young RA. Influence of preparation conditions on the composition of type B carbonated hydroxyapatite and on the localization of the carbonate ions. *Calcif Tissue Int* 1988;43:33–40.
- [26] Carragee EJ, Hurwitz EL, Weiner BK. A critical review of recombinant human bone morphogenetic protein-2 trials in spinal surgery: emerging safety concerns and lessons learned. *Spine J* 2011;11:471–91.
- [27] Woo EJ. Does bone morphogenetic protein increase the incidence of perioperative complications in spinal fusion? A comparison of 55,862 cases of spinal fusion with and without bone morphogenetic protein. *Spine* 2012;37:259.

- [28] Boix T, Gomez-Morales J, Torrent-Burgues J, Monfort A, Puigdomenech P, Rodriguez-Clemente R. Adsorption of recombinant human bone morphogenetic protein rhBMP-2 onto hydroxyapatite. *J Inorg Biochem* 2005;99:1043–50.
- [29] Ruhe PQ, Boerman OC, Russel FG, Mikos AG, Spauwen PH, Jansen JA. In vivo release of rhBMP-2 loaded porous calcium phosphate cement pretreated with albumin. *J Mater Sci Mater Med* 2006;17:919–27.
- [30] Autefage H, Briand-Mesange F, Cazalbou S, Drouet C, Fourmy D, Goncalves S, et al. Adsorption and release of BMP-2 on nanocrystalline apatite-coated and uncoated hydroxyapatite/beta-tricalcium phosphate porous ceramics. *J Biomed Mater Res B Appl Biomater* 2009;91:706–15.
- [31] Donnyi Y, Iwanaga H, Shibutani T, Moriwaki Y, Iwayama Y. Osteoclastic responses to various calcium phosphates in cell cultures. *J Biomed Mater Res* 1999;47:424–33.
- [32] Leeuwenburgh S, Layrolle P, Barrère F, de Bruijn J, Schoonman J, van Blitterswijk CA, et al. Osteoclastic resorption of biomimetic calcium phosphate coatings in vitro. *J Biomed Mater Res* 2001;56:208–15.
- [33] LeGeros RZ. Biodegradation/bioresorption of CaP materials. *Clin Mater* 1993;14:65–88.
- [34] Dorozhkin SV. Calcium orthophosphates. Occurrence properties biomineralization, pathological, calcification, and biomimetic applications. *Biomater* 2011;1:121–64.
- [35] Rohanizadeh R, Chung K. Hydroxyapatite as a carrier for bone morphogenetic protein. *J Oral Implantol* 2011;37:659–72.
- [36] Perri B, Cooper M, Lauryssen C, Anand N. Adverse swelling associated with use of rhBMP-2 in anterior cervical discectomy and fusion: a case study. *Spine J* 2007;7:235–9.
- [37] Boden SD. Bioactive factors for bone tissue engineering. *Clin Orthop Relat Res* 1999;367:S84–94.
- [38] Murnaghan M, McIlmurray L, Mushipe MT, Li G. Time for treating bone fracture using rhBMP-2: a randomised placebo controlled mouse fracture trial. *J Orthop Res* 2005;23:625–31.
- [39] Suzawa M, Takeuchi Y, Fukumoto S, Kato S, Ueno N, Miyazono K, et al. Extracellular matrix-associated bone morphogenetic proteins are essential for differentiation of murine osteoblastic cells in vitro. *Endocrinology* 1999;140:2125–33.
- [40] Bi L, Jung SB, Day DE, Neidig K, Dusevich V, Eick JD, et al. Evaluation of bone regeneration, angiogenesis, and hydroxyapatite conversion in critical-sized rat calvarial defects implanted with bioactive glass scaffolds. *J Biomed Mater Res A* 2012;100:3267–75.
- [41] Bi L, Rahaman MN, Day DE, Brown Z, Samujh C, Liu X, et al. Effect of borate bioactive glass microstructure on bone regeneration, angiogenesis, and hydroxyapatite conversion in a rat calvarial defect model. *Acta Biomater* 2013;9:8015–26.

- [42] Zhao J, Shen G, Liu C, Wang S, Zhang W, Zhang X, Zhang Ye D, Wei J, Zhang Z, Jiang X. Enhanced healing of rat calvarial defects with sulfated chitosan-coated calcium-deficient hydroxyapatite/bone morphogenetic protein 2 scaffolds. *Tissue Eng A* 2012;18:185–97.
- [43] Jang J-W, Yun JH, Lee K-I, Jang J-W, Jung U-W, Kim C-S, et al. Osteoinductive activity of biphasic calcium phosphate with different rhBMP-2 doses in rats. *Oral Surg Oral Med O* 2011;113:480–7.

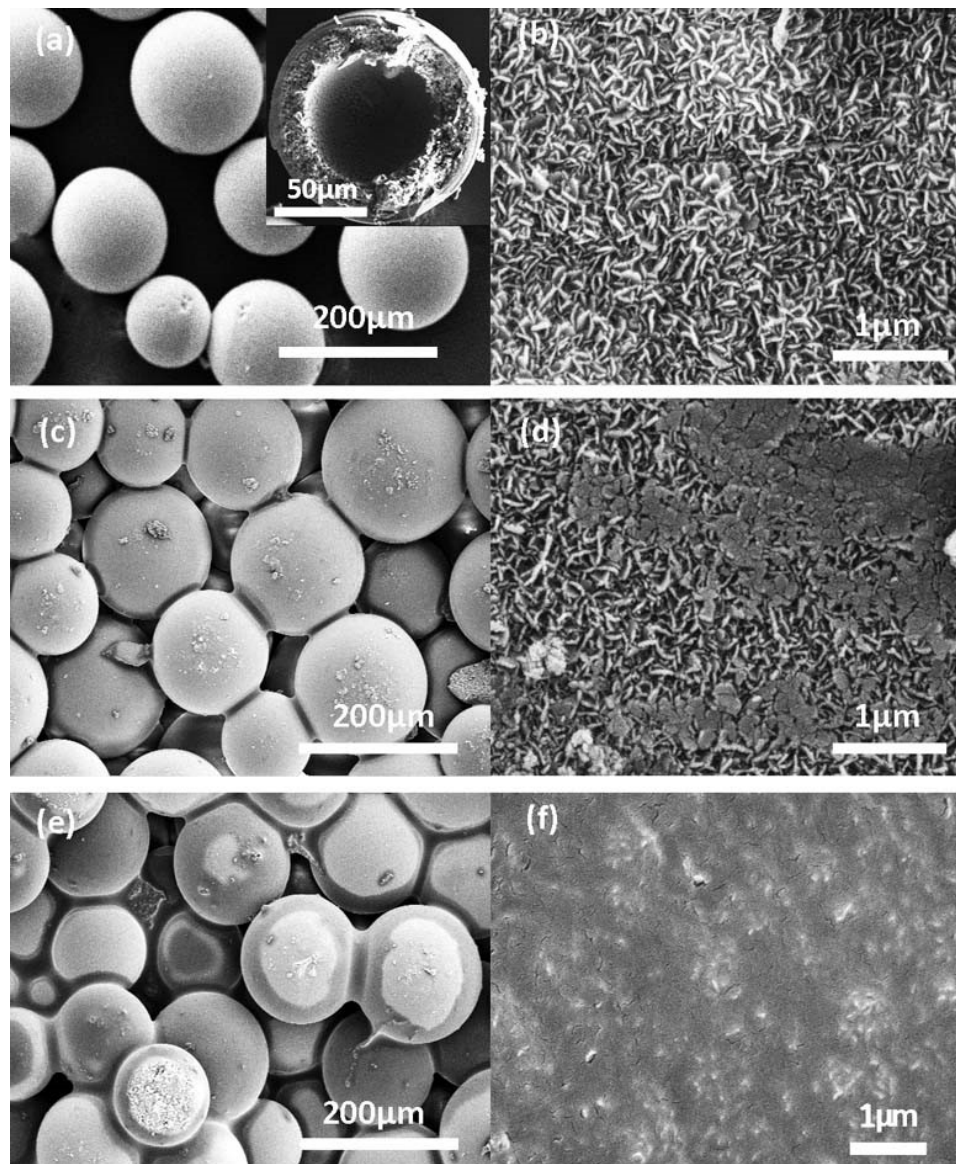


Fig. 1. Low- and high-magnification SEM images of the surface of hollow HA microspheres as prepared (a, b), and after coating with solutions containing 50 mg ml⁻¹ PLGA (c, d), and 200 mg ml⁻¹ PLGA (e, f), followed by drying. The inset in (a) shows a cross-section of a hollow HA microsphere.

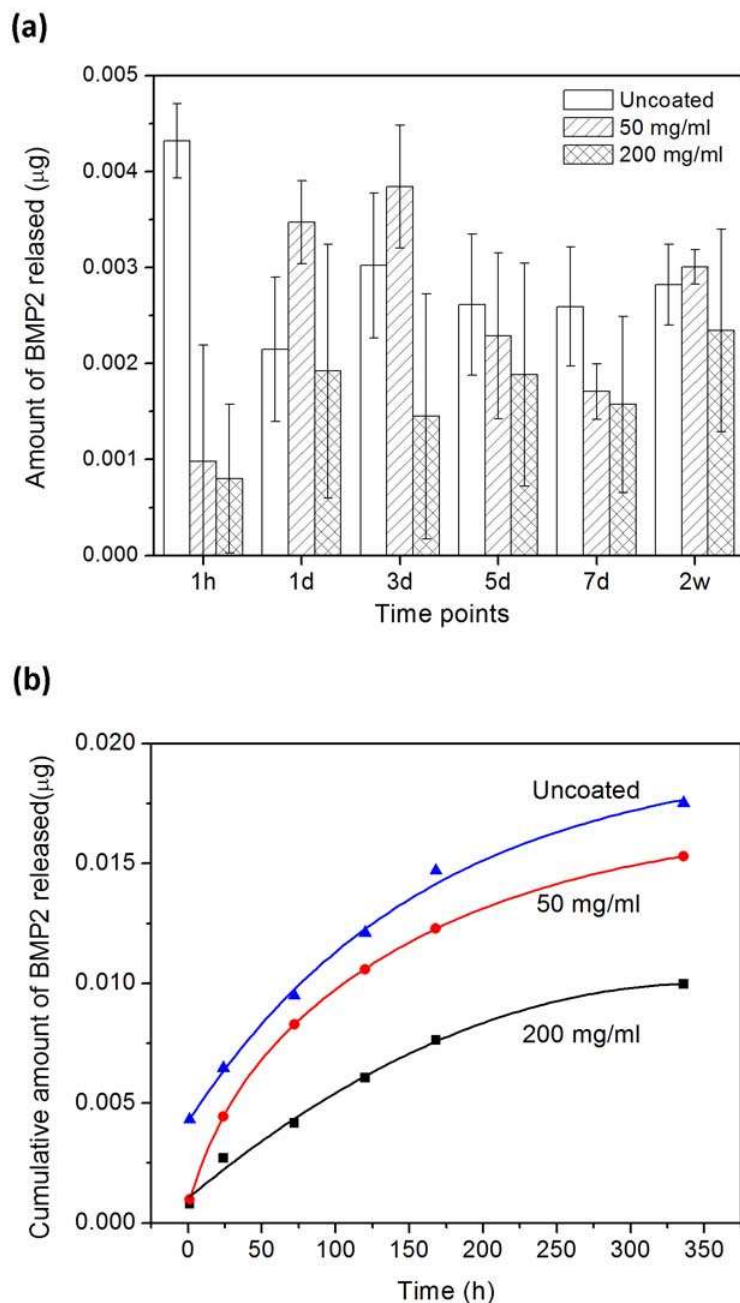


Fig. 2. (a) Amount of BMP2 released from hollow HA microspheres into a medium composed of equal volumes of FBS and PBS at selected time periods; (b) average cumulative amount of BMP2 released from the microspheres into the medium as a function of time. Data for the as-prepared microspheres (uncoated), and microspheres coated with 50 mg ml⁻¹ PLGA solution (50 mg ml⁻¹), and with 200 mg ml⁻¹ PLGA solution (200 mg ml⁻¹).

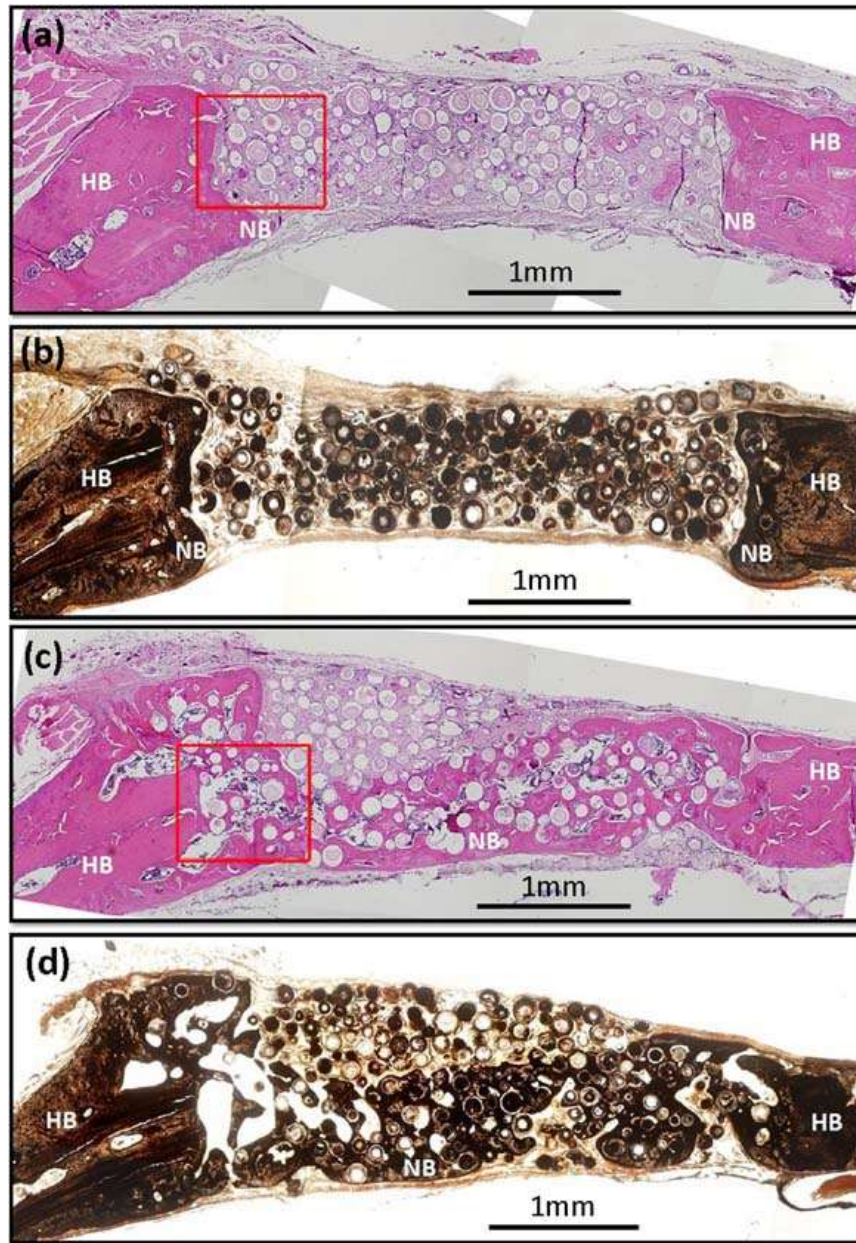


Fig. 3. (a, c) H&E and (b, d) von Kossa stained sections of rat calvarial defects implanted for 6 weeks with (a, b) as-prepared hollow HA microspheres (without BMP2) and (c, d) hollow HA microspheres loaded with BMP2 (1 µg per defect). HB = host (old) bone; NB = new bone.

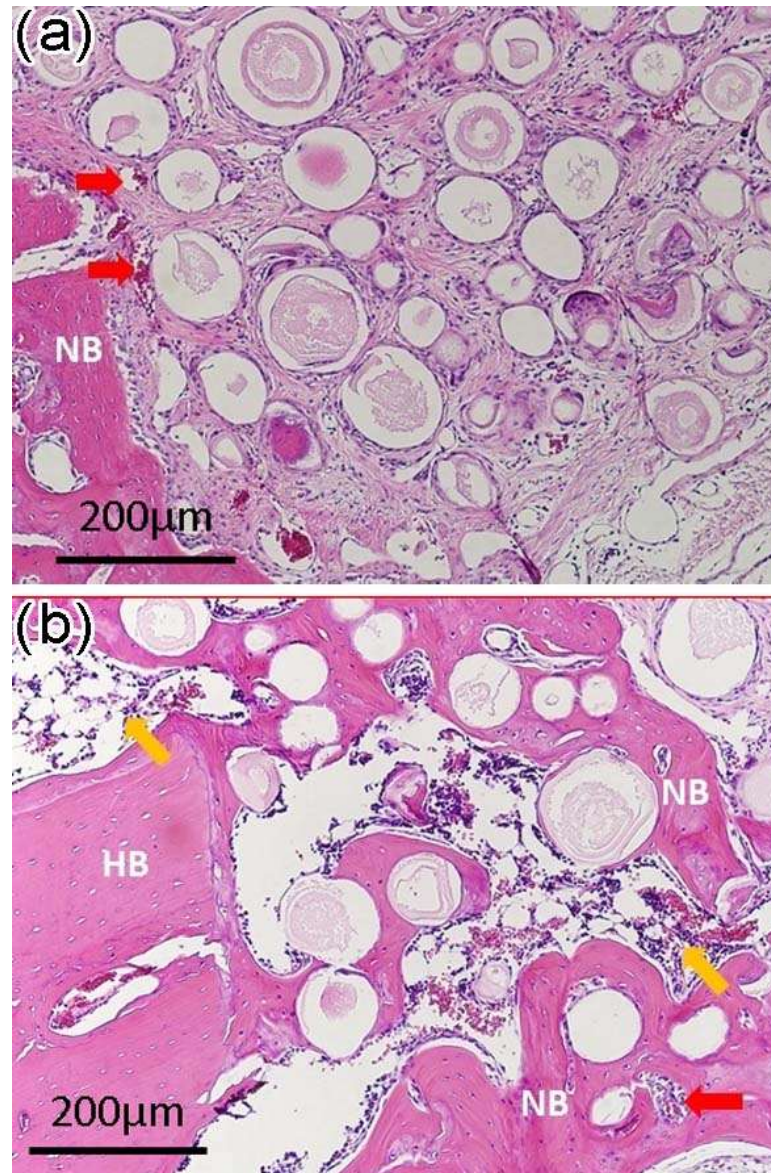


Fig. 4. High-magnification images of H&E stained sections of rat calvarial defects implanted for 6 weeks with (a) as-prepared hollow HA microspheres (without BMP2) and (b) hollow HA microspheres loaded with BMP2 (1 μ g per defect). The images shown in (a) and (b) correspond to the boxed area outlined in Fig. 3a and b, respectively. HB = host (old) bone; NB = new bone; red arrows indicate blood vessels; yellow arrows indicate bone marrow-like tissue.

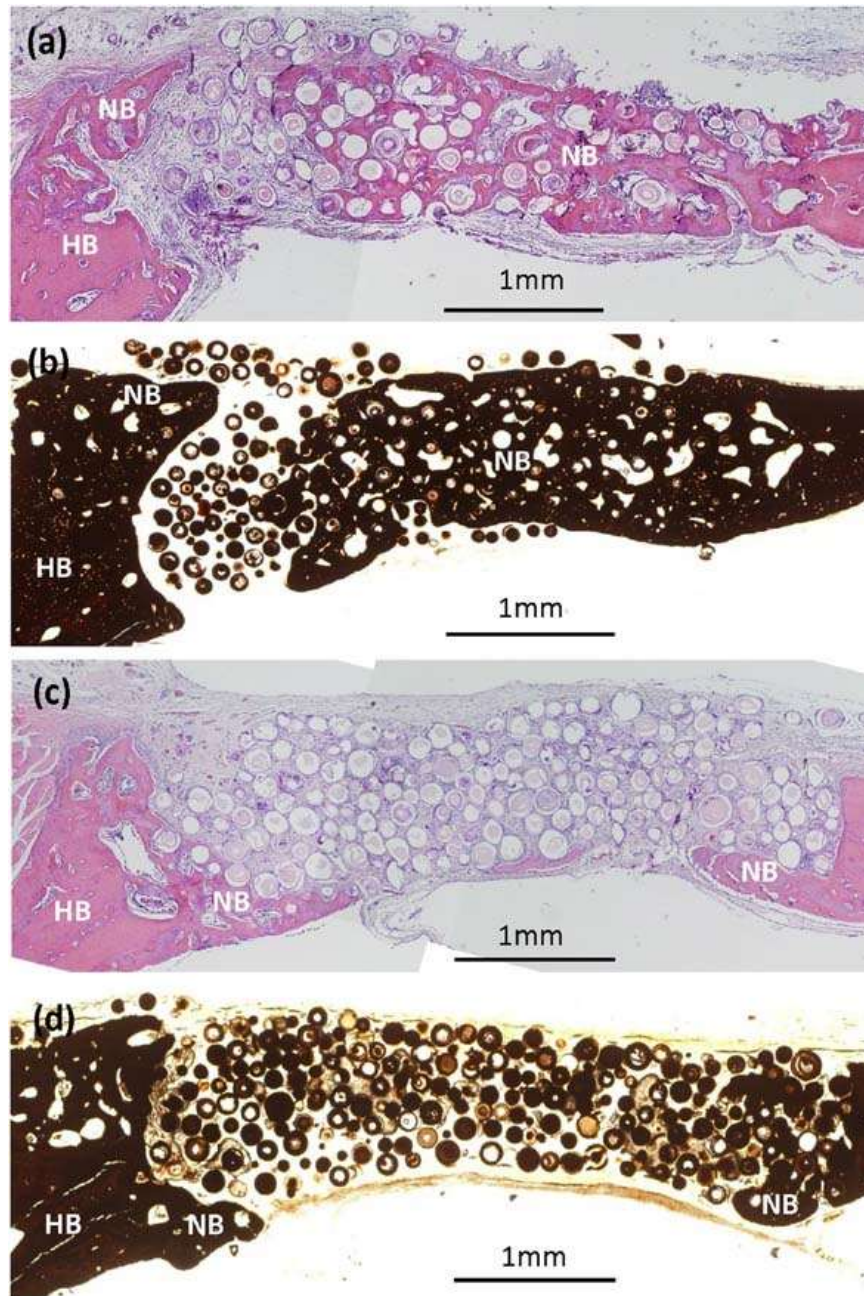


Fig. 5. (a, c) H&E and (b, d) von Kossa stained sections of rat calvarial defects implanted for 6 weeks with hollow HA microspheres loaded with BMP2 and coated with different amounts of PLGA formed from solutions containing 50 mg ml^{-1} PLGA (a, b) and 200 mg ml^{-1} PLGA (c, d). HB = host (old) bone; NB = new bone.

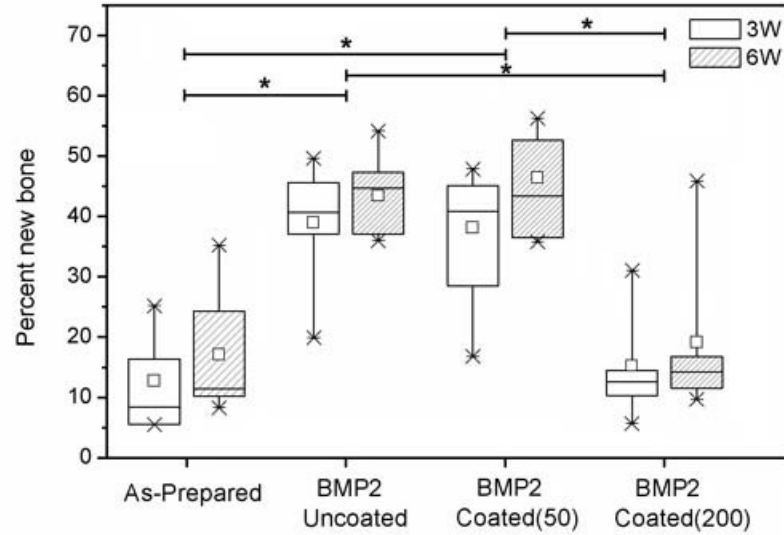


Fig. 6. Box plot comparing the percent new bone formed in rat calvarial defects implanted for 3 weeks (3 W) and 6 weeks (6 W) with four groups of implants composed of hollow HA microspheres: (a) as prepared; (b) loaded with BMP2 (denoted BMP2/Uncoated); (c) loaded with BMP2 and coated using a 50 mg ml⁻¹ PLGA solution (denoted BMP2/Coated(50)); (d) loaded with BMP2 and coated using a 200 mg ml⁻¹ PLGA solution (denoted BMP2/Coated(200)). The median and mean values, interquartile range, and the high and low values for each group are shown. (n = 5; /P < 0.05).

Table I. Percentage of new bone (mean ± SD) formed in rat calvarial defects implanted for 3 weeks and 6 weeks with four groups of hollow HA microspheres used in this study: microspheres without BMP2; microspheres with BMP2; BMP2-loaded microspheres coated with 50 mg ml⁻¹ PLGA solution; BMP2-loaded microspheres coated with 200 mg ml⁻¹ PLGA solution.

HA microspheres	Implantation time	
	3 weeks	6 weeks
Without BMP2	13 ± 5	17 ± 10
With BMP2	39 ± 10	43 ± 6
With BMP2; PLGA coating (50 mg ml ⁻¹)	38 ± 11	46 ± 8
With BMP2; PLGA coating (200 mg ml ⁻¹)	15 ± 8	19 ± 13

Table II. Comparison of percent new bone (mean \pm SD) formed in rat calvarial defects implanted with the hollow HA microspheres (106–150 μm) used in this study, and with selected bioactive ceramic and glass implants.

Implant	Growth factor	Implantation time (weeks)	% new bone	Reference
Hollow HA microspheres	–	6	17 ± 10	This study
Hollow HA microspheres	BMP2 (1 $\mu\text{g}/\text{defect}$)	6	43 ± 6	This study
Hollow HA microspheres	TGF β 1 (5 $\mu\text{g}/\text{defect}$)	12	19 ± 4	[15]
45S5 silicate glass particles (150-250 μm)	–	12	19 ± 3	[40]
13-93B3 borate glass scaffold (porosity = 77%; pore size = 200-400 μm)	–	12	15 ± 3	[41]
Calcium-deficient HA (porosity = 75%; pore size = 400-500 μm)	–	8	10 ± 3	[42]
Calcium-deficient HA (porosity = 75%; pore size = 400-500 μm)	BMP2 (2 $\mu\text{g}/\text{defect}$)	8	27 ± 4	[42]
BCP (porosity = 70%; pore size = 300-600 μm and <10 μm) ^a	–	8	23 ± 5	[43]
BCP (porosity = 70%; pore size = 300-600 μm and <10 μm) ^a	BMP2 (2.5 $\mu\text{g}/\text{defect}$)	8	55 ± 8	[43]

^a BCP: biphasic calcium phosphate (HA: β TCP = 20:80); two-thirds of the porosity in the range 300-600 μm ; one-third of the porosity <10 μm .

II. Preparation of resorbable carbonate-substituted hollow hydroxyapatite microspheres and their evaluation in osseous defects in vivo

Wei Xiao ^a, B. Sonny Bal ^b, Mohamed N. Rahaman ^a

^a Department of Materials Science and Engineering, Missouri University of Science and Technology, Rolla, MO 65409, USA

^b Department of Orthopaedic Surgery, University of Missouri, Columbia, MO 65212, USA

ABSTRACT

Hollow hydroxyapatite (HA) microspheres, with a high-surface-area mesoporous shell, can provide a unique bioactive and osteoconductive carrier for proteins to stimulate bone regeneration. However, synthetic HA has a slow resorption rate and a limited ability to remodel into bone. In the present study, hollow HA microspheres with controllable amounts of carbonate substitution (0–12 wt.%) were created using a novel glass conversion route and evaluated in vitro and in vivo. Hollow HA microspheres with ~12 wt.% of carbonate (designated CHA12) showed a higher surface area ($236 \text{ m}^2 \text{ g}^{-1}$) than conventional hollow HA microspheres ($179 \text{ m}^2 \text{ g}^{-1}$) and a faster degradation rate in a potassium acetate buffer solution. When implanted for 12 weeks in rat calvarial defects, the CHA12 and HA microspheres showed a limited capacity to regenerate bone but the CHA12 microspheres resorbed faster than the HA microspheres. Loading the microspheres with bone morphogenetic protein-2 (BMP2) ($1 \mu\text{g}$ per defect) stimulated bone regeneration and accelerated resorption of the CHA12 microspheres. At 12 weeks, the amount of new bone in the defects implanted with the CHA12 microspheres ($73 \pm 8\%$) was significantly higher than the HA microspheres ($59 \pm 2\%$) while the amount of residual CHA12 microspheres ($7 \pm 2\%$ of the total defect area) was significantly lower than the HA microspheres ($21 \pm 3\%$). The combination of these carbonate-substituted HA microspheres with clinically safe doses of BMP2 could provide promising implants for healing non-loaded bone defects.

1. Introduction

The healing of large bone defects resulting from trauma, resection of tumors or congenital diseases represents a common and significant problem in craniofacial and orthopedic surgery. Clinically those defects are reconstructed using autologous bone grafts, allografts and biocompatible synthetic materials [1–3]. Autologous bone grafts are the gold standard for treatment while bone allografts are the most commonly used bone grafts. However, they suffer from limitations such as limited supply, donor site morbidity (autografts), high cost, uncertain healing and risk of infection (allografts) [4]. Because of these limitations, the need for synthetic biomaterials continues to grow.

A variety of synthetic bone graft substitutes have been developed over the last several decades [1,2]. They include calcium phosphate bioceramics such as hydroxyapatite (HA), beta-tricalcium phosphate (β -TCP), biphasic calcium phosphate (BCP), calcium phosphate cements, bioactive glass and biodegradable polymers. However, synthetic bone graft materials generally lack the osteoinductivity and osteogenicity of autogenous bone grafts, functioning mainly as osteoconductive implants [1,5–7]. The use of synthetic biomaterials by themselves commonly fails to produce clinically significant bone formation in a clinically relevant time [7,8]. In practice, synthetic biomaterials are often combined with autologous bone, osteogenic growth factors or cells in order to achieve reliable reconstruction of bone [7,9–11].

Calcium phosphate bioceramics such as HA, β -TCP and BCP have been used in dentistry and medicine for bone repair and augmentation for over 30 years [12,13]. They have a high affinity for binding and concentrating proteins which make them ideal carriers for growth factors such as bone morphogenetic protein-2 (BMP2) and bioactive peptides [14,15]. Several studies have shown that when combined with BMP2, calcium phosphate bioceramics in the form of porous particles, granules or three-dimensional scaffolds enhanced osteogenesis in animal models when compared to the calcium phosphate bioceramics without BMP2 [16–21].

HA is often considered to be a prototype biomaterial for bone repair and augmentation because of its similarity to the mineral constituent of living bone [22]. However, synthetic HAs with a nearly stoichiometric composition often have a low resorption rate, resulting in the material remaining nearly bioinert in vivo over a long

period [23,24]. In comparison, biological HAs contain minor and trace elements and are therefore not pure HA. The most important minor substituents are CO_3 , Mg and Sr. The ability of the implant to remodel into bone within a clinically relevant time is desirable for bone repair. The degradation of HA and other calcium phosphate bioceramics can occur by two processes: solution-mediated dissolution [14,23], and cell-mediated degradation resulting from the activities of osteoclastic cells [25–27]. Ionic substitution by $(\text{CO}_3)^{2-}$, Mg^{2+} and Sr^{2+} , fine particle size, high surface area and high porosity have been shown to improve the solution-mediated degradation rate of HA [14,27–30] whereas $(\text{CO}_3)^{2-}$ substitution and fine grain size have been found to be desirable for osteoclastic resorption [25,26].

In the last few years, we have been developing a hollow HA microsphere technology to address the need for bone graft substitutes that could approach the combined osteoconductive, osteoinductive and osteointegrative properties of autologous bone grafts. The hollow HA microspheres, prepared by a novel glass conversion route near room temperature, have a high surface area ($>100\text{m}^2\text{ g}^{-1}$) and a mesoporous shell wall (pore size=10–20nm) composed of nanocrystalline HA particles[31]. Our previous studies showed that hollow HA microspheres can function as a carrier for the controlled delivery of proteins and growth factors [32,33]. When loaded with BMP2 (1 μg per defect), the hollow HA microspheres (106–150 μm) enhanced bone regeneration in rat calvarial defects (4.6mm in diameter) when compared to similar microspheres without BMP2, resulting in bridging of the defects by new bone within 6 weeks [33]. However, little resorption of the HA microspheres was observed in the defects within the six-week implantation period.

The objective of this study was to create hollow HA microspheres with a faster degradation rate and test their performance in vitro and in vivo. The glass conversion process used in our previous studies was modified to create hollow HA microspheres with controllable amounts of $(\text{CO}_3)^{2-}$ substitution. Carbonate-substituted HA compositions were used because they have been shown to result in enhanced degradation or resorption rates. The dissolution of the microspheres in a potassium acetate buffer solution and their degradation by osteoclastic cells was studied in vitro. Microspheres with or without BMP2 were implanted in rat calvarial defects in vivo and their ability to

resorb and to regenerate bone was evaluated at 12 weeks postimplantation using histomorphometric methods.

2. Materials and methods

2.1. Preparation and characterization of hollow HA microspheres

Hollow HA microspheres with a nearly stoichiometric composition were prepared by reacting solid glass microspheres in an aqueous phosphate solution, as described in detail in our previous study [31]. Briefly, borate glass microspheres (150–250 μm) with the composition 15CaO, 11Li₂O, 74B₂O₃ (wt.%) were reacted for 7 days in 0.02 M K₂HPO₄ solution at 37 °C and starting pH = 9.0. A mass of 4 g glass microspheres was reacted in 800 ml of the phosphate solution in all of the conversion experiments. The converted microspheres were washed 3 times with deionized water, soaked in anhydrous ethanol to displace residual water, and dried for at least 12 h at room temperature then for at least 12 h at 90 °C. Carbonate-substituted HA (CHA) microspheres with varying carbonate content were prepared using the same method but the phosphate solution used in the conversion process contained different concentrations of carbonate ions by adding KHCO₃ to the solution (Table I).

Characterization of the converted microspheres (HA and CHA) was performed using the methods described previously [31]. Briefly, the microstructure of the surface and cross section of the microspheres was examined using scanning electron microscopy (SEM) (S4700; Hitachi, Tokyo, Japan). X-ray diffraction (XRD) (D/mas 2550 v; Rigaku; The Woodlands, TX, USA) was used to check for the presence of crystalline phases in the converted microspheres while Fourier transform infrared (FTIR) spectroscopy (NEXUS 670; Thermo Nicolet; Madison, WI, USA) was used to determine the chemical groups in the composition. The specific surface area, average pore size and pore size distribution of the shell of the converted microspheres were measured using nitrogen adsorption (Autosorb-1; Quantachrome, Boynton Beach, FL, USA). In addition, the carbon content of the converted microspheres was determined at a commercial laboratory using a Carbon/Sulfur Analyzer (CS844; LECO Corp.; St. Joseph, MI, USA) designed to measure the carbon and sulfur content in metals and ceramics using a combustion method. Three samples from each group of microspheres were analyzed and the carbonate content

was determined by assuming that all the measured carbon in the microspheres was present as carbonate (CO_3).

2.2. Degradation of hollow HA and CHA microspheres in vitro

The solubility of the converted microspheres was determined by measuring the concentration of Ca^{2+} ions released from the microspheres as a function of immersion time in an acidic buffer (0.1 M potassium acetate; pH = 5.0) at 37 °C [23,34], using inductively coupled plasma optical emission spectrometry (ICP-OES) (Optima 2000DV; Perkin Elmer, Waltham, MA). A fixed surface area to volume ratio ($50 \text{ m}^2 \text{ l}^{-1}$) of HA microspheres to potassium acetate solution was used. Three samples from each group were analyzed at each time point. The solubility of granules composed of medical grade beta-tricalcium phosphate (β -TCP) (Himed; Old Bethage, NY) was used as a reference for comparison.

2.3. Osteoclastic resorption of hollow HA and CHA microspheres in vitro

Cell-mediated degradation of the converted microspheres was studied using induced osteoclast cultures [26,35]. The human monocyte-like cell line TIB-71 (ATCC, USA) was cultured in Dulbecco's modified Eagle's medium (DMEM) supplemented with 10 vol.% fetal bovine serum (FBS) (Sigma-Aldrich, St. Louis, MO) and 1 vol.% penicillin/streptomycin (Invitrogen) at 37 °C in a humidified atmosphere of 5% CO_2 . The microspheres were sterilized by soaking in anhydrous ethanol and exposure to ultraviolet light. Then TIB-71 cells were seeded at a concentration of 10^5 cells/ml and incubated at 37 °C in a humidified CO_2 atmosphere. At day 1, 50 ng/ml RANKL (Biolegend, San Diego, CA) was added to the culture media to induce the differentiation of the TIB-71 cells to osteoclasts. The media was replaced with fresh media containing 50 ng/ml RANKL every 2 days for the remainder of the experiment.

The microspheres were removed from the culture media at day 7 and rinsed with 0.1 M phosphate-buffered saline (PBS). Then the cells were fixed with 2% paraformaldehyde plus 2% glutaraldehyde in 0.1 M cacodylate buffer overnight at 4 °C. Each sample was rinsed with 0.1 M cacodylate buffer and fixed in 2% osmium tetroxide for 2 h at room temperature. The fixed samples were dehydrated in a graded ethanol

series, soaked in hexamethyldisilazane (HMDS) and dried in air to allow the liquid to fully evaporate. The dried samples were sputter-coated with gold and observed in a scanning electron microscope (S-4700; Hitachi) at an accelerating voltage of 15 kV and a working distance of 13 mm.

2.4. Animals and surgery

Hollow HA and CHA microspheres, as-prepared or loaded with BMP2, were implanted in rat calvarial defects to evaluate their response in osseous defects. After being sterilized by soaking in anhydrous ethanol and exposure to ultraviolet light, the microspheres were loaded with BMP2 using a procedure described in detail in our previous study [33]. Briefly, 10 mg of hollow microspheres were placed in a 1 ml centrifuge tube, and 10 μ l of BMP2 solution, formed by dissolving 10 μ g BMP2 (Shenandoah Biotechnology Inc., Warwick, PA) in 100 μ l sterile citric acid (pH = 3.0), was pipetted onto the microspheres. A small vacuum was applied to the system to replace the air in the hollow microspheres with the BMP2 solution. The BMP2 solution was completely absorbed in the microspheres. The BMP2-loaded microspheres were dried overnight in a refrigerator at 4 °C until used in the animal experiments the following day.

All animal experimental procedures were approved by the Missouri University of Science and Technology Animal Care and Use Committee, in compliance with the NIH Guide for Care and Use of Laboratory Animals (1985). Sprague Dawley rats (3 months old; 350 ± 30 g) were housed in the animal care facility and acclimated to diet, water and housing under a 12 h/12 h light/dark cycle. The rats were anesthetized with an intramuscularly injected mixture of ketamine and xylazine (1.5 μ l/kg). The surgical area was shaved, scrubbed with 70% ethanol and iodine, and then draped. With sterile instruments and an aseptic technique, a cranial skin incision was sharply made in an anterior to posterior direction along the midline. The subcutaneous tissue, musculature and periosteum were dissected and reflected to expose the calvarium. Bilateral full-thickness defects 4.6 mm in diameter were created in the central area of each parietal bone using a PBS-cooled trephine drill without disturbing the dura mater. The sites were constantly irrigated with sterile PBS to prevent overheating of the bone margins and to remove the bone debris. The bilateral defects were randomly implanted with 7 replicates

per group but microspheres with and without BMP2 were not mixed in the same animal. Each defect was implanted with the same mass of microspheres (10 mg). The number of replicates per group ($n = 7$) was based on our previous studies [33]. The periosteum and skin were repositioned and closed using wound clips. The animals were given a dose of ketoprofen (3 mg/kg mass of the animal) intramuscularly and 0.2 ml penicillin subcutaneously post-surgery, and they were monitored daily for the condition of the surgical wound, food intake, activity and clinical signs of infection. After 12 weeks, the animals were sacrificed by CO₂ inhalation and the calvarial defects with surrounding bone and soft tissue were harvested for subsequent evaluation. This implantation time was used because our previous study showed that for the same animal model, the amount of new bone in the defects implanted with the HA microspheres without BMP2 was limited at 6 weeks [33].

2.5. Histologic processing

The harvested calvarial samples were fixed in 10% formaldehyde for 5 days, washed with deionized water and then cut in half. Half of each sample was for paraffin embedding while the other half was for poly(methyl methacrylate) (PMMA) embedding. The samples for paraffin embedding were decalcified in 14% ethylenediaminetetraacetic acid (EDTA) for 2 weeks, dehydrated in a graded series of ethanol and embedded in paraffin using routine histological techniques [36]. Then the samples were sectioned to 5 μ m using a microtome and stained with hematoxylin and eosin (H&E). The undecalcified samples were dehydrated in a graded series of ethanol and embedded in PMMA. Sections were affixed to acrylic slides, ground down to 40 μ m using a surface grinder (EXAKT 400CS, Norderstedt, Germany) and stained using the von Kossa method. Transmitted light images of the stained sections were taken with an Olympus BX 50 microscope connected to a CCD camera (DP70, Olympus, Japan).

2.6. Histomorphometric analysis

Histomorphometric analysis was carried out using optical images of the stained sections and the ImageJ software (National Institutes of Health, USA). One section across the diameter of each defect was analyzed. The amount of new bone and residual HA (or

CHA) microspheres in the defects was evaluated from the H&E stained sections. The entire defect area was determined as the area between the two defect margins, including the HA microspheres and the tissues. The newly formed bone and residual microspheres within the defect area were then outlined and measured. The area of new bone and residual HA microspheres was expressed as a percentage of the total defect area. The von Kossa positive area in the defects implanted with microspheres was determined from the von Kossa stained sections, which yielded the combined amount of mineralized bone and hydroxyapatite as both bound the silver nitrate.

2.7. Statistical analysis

The data are presented as a mean \pm standard deviation (SD). Analysis for differences between groups was performed using one-way analysis of variance (ANOVA) with Tukey's post hoc test. Differences were considered significant for $p < 0.05$.

3. Results

3.1. Characteristics of converted microspheres

The BET surface area, average pore size (diameter or width) and carbonate content of the three groups of converted microspheres used in the present study (external diameter = 150–250 μm) are summarized in Table I. The microspheres designated HA, corresponded to the microspheres used in our previous studies [31–33]. The carbonate content of those HA microspheres was not determined previously but the results of the present study showed that they contained 2.1 wt.% carbonate. The carbonate substitution presumably resulted from dissolved CO_2 in the aqueous phosphate solution used in converting the glass microspheres to hydroxyapatite microspheres. However, for consistency with our previous studies, we will continue to refer to those microspheres as HA microspheres. The microspheres formed by conversion in the aqueous phosphate solutions that contained 0.135 and 0.27 M KHCO_3 , with a carbonate content of 8.6 and 12.4 wt.%, respectively, will be referred to as CHA9 and CHA12. The surface area of the CHA9 and CHA12 microspheres was higher than the HA microspheres, presumably because of a finer particle (or pore) size. The average pore size of the shell was 11, 8 and 7 nm, respectively, for the HA, CHA9 and CHA12 microspheres.

SEM images of the cross section of the microspheres confirmed that they were hollow (Fig. 1). The surface of the HA microspheres showed needle-like particles, similar to those for the HA microspheres prepared previously [31–33]. In comparison, the surface of the CHA9 and CHA12 microspheres was composed of nearly spherical particles. The peaks in the XRD patterns of the HA, CHA9 and CHA12 microspheres corresponded to a reference hydroxyapatite (JCPDS 72-1243) (Fig. 2a). However, the height of the major peak for the CHA9 and CHA12 groups decreased by 30% and 40%, respectively, and the half-width increased by 10% and 15%, respectively, relative to the major peak for the HA group.

The most dominant resonances in the FTIR spectra (Fig. 2b) of the three groups of microspheres were the phosphate ν_3 resonance, centered at $\sim 1040\text{ cm}^{-1}$, and the phosphate ν_4 resonance with peaks at ~ 605 and 560 cm^{-1} that are associated with crystalline HA [37,38]. The peaks at $\sim 1450\text{--}1490\text{ cm}^{-1}$ are associated with the C–O ν_3 resonance while the peak at 875 cm^{-1} is associated with the $\text{CO}_3^{2-}\nu_2$ resonance [39]. The increase in peak area from HA to CHA12 indicated an increase in carbonate content, in accordance with the results of Table I. These resonances also indicated that a B-type substitution in which carbonate ions substitute for the phosphate ions in the hydroxyapatite lattice [40].

3.2. Solution mediated degradation *in vitro*

The solution-mediated degradation of hydroxyapatite is generally considered to be a congruent process, so the dissolution rate can be described by the rate of Ca^{2+} ion release. The cumulative amount of Ca^{2+} ions released from the HA, CHA9 and CHA12 microspheres into the potassium acetate buffer solution (at a constant surface area to volume ratio) is shown as a function of immersion time in Fig. 3a. The release profiles of the three groups of microspheres showed the same trend. The release was more rapid initially (up to $\sim 10\text{ h}$), slowed considerably thereafter and almost ceased after $\sim 24\text{ h}$. At any immersion time, the amount of Ca^{2+} ions released into the medium increased with the carbonate content of the microspheres. However, the amount of Ca^{2+} ions released from the CHA12 microspheres was still considerably lower than the β -TCP reference material. The amount of Ca^{2+} ions released into the medium at an immersion time of 1 h (Fig. 3b)

showed a significant increase with increasing carbonate substitution but the amount of Ca^{2+} ions released from the CHA12 microspheres was significantly smaller than the β -TCP reference material.

3.3. Cell mediated degradation in vitro

After 7 days of incubation, giant cells with multiple nuclei were found on the surface of the microspheres (Fig. 4a1–3). These osteoclast-like cells had an average size of $\sim 50 \mu\text{m}$. After the cells were rinsed off, pits became visible on the surface of the microspheres (Fig. 4b1–3), showing degradation of the microspheres by the osteoclastic cells. The surface of the CHA12 microspheres appeared to have deeper pits than the HA and CHA9 microspheres. However, because of curved surface of the microspheres and the size of the cells relative to the microsphere diameter, the amount of the pitted area, as a fraction of the surface area of the microspheres could not be readily quantitated.

3.4. Bone regeneration in rat calvarial defects in vivo

Optical images of the H&E stained sections of the rat calvarial defects implanted with the HA and CHA12 microspheres without BMP2 are shown in Fig. 5. For both implant groups, new bone formation was limited and it was confined mainly to the edge (periphery) of the defect. Although the same mass of HA and CHA12 microspheres was implanted in the defects, the amount of CHA12 microspheres remaining in the defects ($28 \pm 8\%$ of the total defect area) was smaller than the HA microspheres ($34 \pm 10\%$) but the difference was not significant (Fig. 5a, b). Several CHA12 microspheres were composed of open (or incomplete) microspheres (Fig. 5a; arrows) in which a large segment of the shell was missing. These open microspheres were filled with fibrous (soft) tissue. They were presumably formed as a result of resorption in vivo. The number of open microspheres normalized to the total number of microspheres was $27 \pm 4\%$ and $4 \pm 4\%$, respectively, for the CHA12 and HA groups. Higher magnification images (Fig. 5c, d) of the boxed areas in Fig. 5a, b show a comparison of the open CHA12 microspheres and the closed HA microspheres. While it is possible that the CHA12 microspheres could have a lower strength than the HA microspheres, it appears unlikely that the higher percent of open CHA12 microspheres was due to a lower strength. The calvarial defect is

a non-loaded site and implantation of the microspheres required little force. Furthermore, no broken pieces of CHA12 or HA microspheres were observed during preparation and implantation of the microspheres.

H&E and von Kossa stained sections of the defects implanted with BMP2-loaded CHA12 and HA microspheres for 12 weeks are shown in Fig. 6. Loading the microspheres with BMP2 significantly enhanced their capacity to heal the defects. New bone almost completely infiltrated the pore space between the microspheres and bridged the ends of the defect. The percent new bone in the defects implanted with the BMP2-loaded CHA12 microspheres ($73 \pm 9\%$) was significantly greater than the BMP2-loaded HA microspheres ($59 \pm 2\%$) (Fig. 7). The percent CHA12 microspheres remaining in the defects at 12 weeks ($7 \pm 2\%$ of the total defect area) was significantly lower than the HA microspheres ($21 \pm 3\%$). The images of the H&E stained sections showed that some marrow-like tissue was present in the defect space not occupied by new bone and residual HA or CHA microspheres which is often a feature of bone regeneration stimulated by the use of BMP2 [41–43].

4. Discussion

Hollow HA microspheres, with a high-surface-area mesoporous shell, can provide a unique osteoconductive and bioactive carrier for the local delivery of therapeutics (such as proteins) in bone repair [32,33]. However, HA with a nearly stoichiometric composition has a slow resorption rate and its ability to remodel into bone is limited. The results of the present study showed that partial substitution of the phosphate (PO_4)³⁻ ions with carbonate (CO_3)²⁻ ions in the HA enhanced the degradation or resorption rate of the microspheres. The enhanced resorption rate of the carbonate-substituted hydroxyapatite (CHA) microspheres did not enhance their capacity to regenerate bone in rat calvarial defects when compared to the HA microspheres. Loading the HA and CHA microspheres with BMP2 significantly improved bone regeneration. Defects implanted with the BMP2-loaded CHA microspheres showed significantly higher new bone formation and lower residual microsphere material at 12 weeks when compared to the BMP2-loaded HA microspheres. These CHA microspheres, when loaded with clinically safe doses of

BMP2, are promising implants for regenerating bone in non-loaded defects, such as defects in the craniofacial region.

4.1. Properties of carbonate-substituted HA microspheres in vitro

The conversion of borate glass microspheres to hollow HA microspheres in an aqueous phosphate solution near room temperature has been described in detail previously [31]. As the glass degrades, the Ca^{2+} ions released from the glass react with the $(\text{PO}_4)^{3-}$ ions from the solution to form an amorphous calcium phosphate product on the glass surface which subsequently crystallizes to HA. In the present study, varying concentrations of $(\text{CO}_3)^{2-}$ ions were added to the phosphate solution with the objective of forming hollow microspheres composed of carbonate-substituted hydroxyapatite (CHA). The results showed that hollow CHA microspheres were formed and that the amount of carbonate substitution increased with higher amounts of $(\text{CO}_3)^{2-}$ ions in the starting phosphate solution.

The amount of carbonate in human bone mineral is ~ 8 wt.% [44]. In the present study, hollow HA microspheres, similar to the microspheres used in our previous studies (which contained 2.1 wt.% carbonate) and hollow CHA microspheres with 8.6 and 12.4 wt.% carbonate were prepared and evaluated. It is likely that the higher amounts of carbonate could be incorporated into the hollow HA microspheres but that was not investigated. Substitution of Mg^{2+} and Sr^{2+} has also been shown to enhance the degradation rate of HA [27–30] and it is expected that substitution of those ions could also be achieved in the glass conversion route used in the present study.

The FTIR data indicated a B-type substitution in which $(\text{CO}_3)^{2-}$ ions substituted for the $(\text{PO}_4)^{3-}$ ions in the hydroxyapatite lattice [40] which is generally found in typical biological HAs and synthetic HAs formed by precipitation from solution [39]. XRD indicated that the carbonate substitution reduced the crystallinity of the HA. The major hydroxyapatite peak in the XRD pattern showed a decrease in height and an increase in half-width with increasing carbonate (Fig. 2a). SEM showed that the needle-like particle morphology on the surface of the hollow HA microspheres changed to a more rounded morphology on the surface of the CHA microspheres (Fig. 1), while the BET surface area of the CHA microspheres were higher than the HA microspheres. A reduction in

crystallinity and particle size has been observed previously for B-site substituted HA [45,46].

The solubility of the hollow HA microspheres, as measured by the release of Ca^{2+} ions in a potassium acetate buffer solution (pH = 5.0) at 37 °C increased with higher carbonate content (Fig. 3a), which is compatible with the results of previous studies [23,30,47]. As a constant surface area to volume ratio was used in the experiments, the increase in solubility was presumably due to a reduction in crystallinity of the hollow CHA microspheres. The amount of Ca^{2+} ions released from the CHA12 microspheres into the buffer solution at 1 h was more than twice the value from the HA microspheres (Fig. 3b). However, it was still only approximately half the value for a reference β -TCP material with the same surface area.

Degradation of the hollow HA and CHA microspheres by osteoclast-like cells was also observed in vitro, indicating that the microspheres were susceptible to both solution-mediated and cell-mediated resorption. Previous studies showed that osteoclastic degradation of HA was dependent on its composition, crystallinity and grain size [27–30]. Carbonate-substituted HAs with an amorphous structure or a fine grain size were found to be more susceptible to degradation. In the present study, the hollow CHA microspheres with 12 wt.% carbonate appeared to show more extensive degradation than the HA microspheres by osteoclast-like cells but the amount of degradation could not be readily quantitated. There was no observable difference in osteoclast adhesion to the surface of the HA and CHA microspheres. While surface roughness and grain size can influence cell adhesion [48,49], the osteoclasts (~50 μm) were much larger than differences in the surface roughness, grain size and pore size of the microspheres (less than a few tens of nanometers).

4.2. Resorption of hollow microspheres and bone regeneration in vivo

Resorption of the hollow HA and CHA12 microspheres without BMP2 in rat calvarial defects was evaluated at 12 weeks postimplantation from the number of open microspheres as a percentage of the total number of microspheres in the defect site. Degradation of the microspheres was clearly visible in the form of open microspheres in which a segment of the shell was missing (Fig. 5a, b). The percent open microspheres in

the defect implanted with the CHA12 microspheres was significantly greater than the HA group. Solution-mediated resorption of the hollow microspheres is expected to be approximately homogeneous, leading to a gradual reduction in the shell thickness. In comparison, osteoclastic resorption is expected to be more rapid, resulting in more rapid degradation of the portions of the shell where the osteoclasts were attached. The combination of solution-mediated and cell-mediated resorption presumably resulted in the formation of the open microspheres within the twelve-week implantation period.

Bone regeneration in the defects implanted with the HA or CHA12 microspheres (without BMP2) was limited, as observed in our previous study for HA microspheres implanted in the same osseous defect model [33]. Loading the HA and CHA12 microspheres with BMP2 (1 μg per defect) significantly enhanced the capacity of both groups to regenerate bone in the defects. The enhancement of bone regeneration in the defects implanted with the BMP2-loaded HA microspheres is consistent with the results of our previous study [33].

It was also found that the BMP2-loaded CHA12 microspheres had a faster resorption rate than the HA microspheres with BMP2 and the CHA12 microspheres without BMP2. The amount of residual BMP2-loaded CHA12 microspheres in the defects at 12 weeks postimplantation ($7 \pm 2\%$) was significantly lower than the BMP2-loaded HA microspheres ($21 \pm 3\%$) and the CHA12 microspheres without BMP2 ($28 \pm 8\%$). The faster resorption of the BMP2-loaded CHA12 microspheres (when compared to the CHA12 microspheres without BMP2) could be explained in terms of the dual function of BMP2 in controlling bone formation and bone resorption [50]. Briefly, the Smad pathways activated by BMPs play a central role in BMP signaling by activating osteoblastogenesis [51]. However, the Smad pathways activated by BMPs also activate the bone resorption process which involves the expression of BMP antagonists such as Noggin and Sclerostin (SOST), both of which are also secreted from osteoblasts [52]. SOST eventually enhances resorption by triggering receptor activator of nuclear factor-kappa B ligand (RANKL)-osteoprotegerin pathway-induced osteoclastogenesis [53]. In the present study, the enhancement of osteoclastic differentiation by BMP2 can lead to faster degradation of the BMP2-loaded CHA12 microspheres in the rat calvarial defects when compared to the CHA12 microspheres without BMP2.

The percent new bone in the defects implanted with the BMP2-loaded CHA12 microspheres ($73 \pm 9\%$) was significantly greater than the BMP2-loaded HA microspheres ($59 \pm 2\%$). Because of the faster degradation of the CHA12 microspheres, a larger amount of pore space was available for new bone infiltration, resulting in a significantly larger amount of new bone in the defects implanted with the CHA12 microspheres.

The BMP2 dose used in the present study ($1 \mu\text{g}$ per defect) was identical to the dose used in our previous study [33] and within the range of doses used in previous studies for the rat calvarial defect model [54–56]. It is also well below the dose found to cause adverse biological effects in the same animal model [57]. However, the optimal BMP2 dose for the CHA microspheres and the animal model used in the present study was not investigated. Furthermore, the amount of carbonate in the CHA12 microspheres evaluated in vitro ($12.4 \text{ wt.}\%$) was higher than the value ($\sim 8 \text{ wt.}\%$) in human bone. A range of BMP2 doses and CHA microspheres with different carbonate content should be investigated in future studies. In general, the results of the present study indicate that the combination of carbonate-substituted hydroxyapatite microspheres and a clinically safe dose of BMP2 could provide a promising system to stimulate bone regeneration and enhance implant resorption in healing non-loaded bone defects.

5. Conclusions

Hollow hydroxyapatite (HA) microspheres, with a high-surface area mesoporous shell, were prepared with controllable amounts of carbonate substitution ($0\text{--}12 \text{ wt.}\%$) using a novel glass conversion route at 37°C . Hollow HA microspheres with $12.4 \text{ wt.}\%$ of carbonate (designated CHA12) showed a higher surface area ($236 \text{ m}^2 \text{ g}^{-1}$) than hollow HA microspheres prepared conventionally ($179 \text{ m}^2 \text{ g}^{-1}$) and a faster degradation rate in a potassium acetate buffer solution in vitro. When implanted for 12 weeks in rat calvarial defects, the CHA12 and HA microspheres showed a limited capacity to regenerate bone but the CHA12 microspheres resorbed faster than the HA microspheres. Loading the microspheres with bone morphogenetic protein-2 (BMP2) ($1 \mu\text{g}$ per defect) stimulated bone regeneration and accelerated the resorption of the CHA12 microspheres in the defects. The amount of new bone in the defects implanted with the BMP2-loaded CHA12

microspheres was significantly greater than the HA microspheres while the amount of residual CHA12 microspheres was significantly lower than the HA microspheres. The combination of these carbonate substituted HA microspheres with clinically safe doses of BMP2 could provide promising implants for healing non-loaded bone defects.

References

- [1] C. Laurencin, Y. Khan, E.I.-A. SF, *Expert Rev. Med. Devices* 3 (2006) 49–57.
- [2] P.V. Giannoudis, H. Dinopoulos, E. Tsiridis, *Injury* 36 (Suppl. 3) (2005) S20–S27.
- [3] E. Neovius, T. Engstrand, *J. Plast. Reconstr. AES* 63 (2010) 1615–1623.
- [4] C. Dahlin, A. Johansson, *Clin. Implant Dent. Relat.* 13 (2011) 305–310.
- [5] S.S. Stahl, S.J. Froum, *J. Periodontol.* 58 (1987) 689–695.
- [6] T. Turunen, J. Peltola, A. Yli-Urpo, R.P. Happonen, *Clin. Oral Implants Res.* 15 (2004) 135–141.
- [7] D. Rickert, J.J. Slater, H.J. Meijer, A. Vissink, G.M. Raghoobar, *Int. J. Oral Maxillofac. Surg.* 41 (2012) 160–167.
- [8] E.S. Tadjoeidin, G.L. de Lange, D.M. Lyaruu, L. Kuiper, E.H. Burger, *Clin. Oral Implants Res.* 13 (2002) 428–436.
- [9] U.M. Wikesjo, M. Qahash, Y.H. Huang, A. Xiropaidis, G. Polimeni, C. Susin, *Orthod. Craniofacial Res.* 12 (2009) 263–270.
- [10] C.I. Polo, J.L. Oliveira Lima, L. De Lucca, C.B. Piacezzi, M.G. Naclerio-Homem, V.E. Arana-Chavez, W.R. Sendyk, *J. Periodontol.* 84 (2013) 360–370.
- [11] J.C. Reichert, A. Cipitria, D.R. Epari, S. Saifzadeh, P. Krishnakanth, A. Berner, M.A. Woodruff, H. Schell, M.Mehta, M.A. Schuetz, G.N. Duda, D.W. Hutmacher, *Sci. Transl. Med.* 4 (2012) 141ra93.
- [12] M. Bohnner, *Injury* 31 (2000) D37–D47.
- [13] S.V. Dorozhkin, *Bio* 1 (2011) 1–51.
- [14] R.Z. LeGeros, *Clin. Orthop. Relat. Res.* 395 (2002) 81–98.
- [15] S. Bose, S. Tarafder, *Acta Biomater.* 8 (2012) 1401–1421.
- [16] M.I. Alam, I. Asahina, K. Ohmamiuda, S. Enomoto, *J. Biomed. Mater. Res.* 54 (2001) 129–138.
- [17] H. Yuan, J.D. De Bruijn, X. Zhang, C.A. Van Blitterswijk, K. de Groot, *J. Mater. Sci. Mater. Med.* 12 (2001) 761–766.
- [18] P. Ruhé, H. Kroese-Deutman, J.Wolke, P. Spauwen, J. Jansen, *Biomaterials* 25 (2004) 2123–2132.

- [19] Y. Gonda, Y. Shibata, T. Okuda, G. Kawachi, M. Kamitakahara, H. Murayama, et al., *Biomaterials* 30 (2009) 4390–4400.
- [20] J. Tazaki, M. Murata, T. Akazawa, M. Yamamoto, K. Ito, M. Arisue, T. Shibata, Y. Tabata, *Biomed. Mater. Eng.* 19 (2009) 141–146.
- [21] F.Z. Notodihardjo, N. Kakudo, S. Kushida, K. Suzuki, K. Kusumoto, J. *Cranio-Maxillofac. Surg.* 40 (2012) 287–291.
- [22] R.Z. LeGeros, *Monogr. Oral Sci. Karger Basel* 15 (1991) 4–45.
- [23] R.Z. LeGeros, *Clin. Mater.* 14 (1993) 65–88.
- [24] C.P.A.T. Klein, P. Patka, W. den Hollander, *Biomaterials* 10 (1989) 59–62.
- [25] Y. Doi, H. Iwanaga, T. Shibutani, Y. Moriwaki, Y. Iwayama, J. *Biomed. Mater. Res.* 47 (1999) 424–433.
- [26] S. Leeuwenburgh, P. Layrolle, F. Barrère, J. de Bruijn, J. Schoonman, C.A. van Blitterswijk, K. de Groot, J. *Biomed. Mater. Res.* 56 (2001) 208–215.
- [27] Y. Doi, T. Shiutani, Y. Moriwaki, T. Kajimoto, Y. Iwayama, J. *Biomed. Mater. Res.* 39 (1998) 603–610.
- [28] C.P.A.T. Klein, A.A. Driessen, K. De Groot, A. van den Hooff, J. *Biomed. Mater. Res.* 17 (1983) 769–784.
- [29] R.Z. LeGeros, J.R. Parsons, G. Daculsi, F. Driessens, D. Lee, S.T. Liu, S. Metsger, D. Perterson, M. Walker, *Ann. N. Y. Acad. Sci.* 523 (1988) 268–271.
- [30] A.A. Baig, J.L. Fox, J. Su, Z. Wang, M. Otsuka, W.I. Higuchi, R.Z. LeGeros, J. *Colloid Interface Sci.* 179 (1996) 608–617.
- [31] H. Fu, M.N. Rahaman, D.E. Day, Q. Fu, J. *Am. Ceram. Soc.* 93 (2010) 3116–3123.
- [32] H. Fu, M.N. Rahaman, D.E. Day, R.F. Brown, J. *Mater. Sci. Mater. Med.* 22 (2011) 579–591.
- [33] W. Xiao, H. Fu, M.N. Rahaman, Y. Liu, B.S. Bal, *Acta Biomater.* 9 (2013) 8374–8383.
- [34] M. Jarco, *Clin. Orthop.* 157 (1981) 259–278. [35] M. Roy, S. Bose, J. *Biomed. Mater. Res. A* 100 (2012) 2450–2461.
- [36] Y. Lin, W. Xiao, X. Liu, B.S. Bal, L.F. Bonewald, M.N. Rahaman, J. *Non-Cryst. Solids* (2015) <http://dx.doi.org/10.1016/j.jnoncrysol.2015.04.008>.
- [37] A.E. Clark, L.L. Hench, J. *Non-Cryst. Solids* 113 (1989) 195–202.
- [38] M.R. Filgueiras, G. LaTorre, L.L. Hench, J. *Biomed. Mater. Res.* 27 (1993) 445–453.
- [39] N. Patel, S.M. Best, W. Bonfield, J. *Aust. Ceram. Soc.* 41 (2005) 1–22.
- [40] R.Z. LeGeros, J.P. LeGeros, R.O. Trautz, E. Klein, *Dev. Appl. Spectrosc.* 7B (1970) 12–22.
- [41] C. Hayashi, U. Hasegawa, Y. Saita, H. Hemmi, T. Hayata, K. Nakashima, Y. Ezura, T. Amagasa, K. Akiyoshi, M. Noda, J. *Cell. Physiol.* 220 (2009) 1–7.

- [42] S.J. Hong, C.S. Kim, D.K. Han, I.H. Cho, U.W. Jung, S.H. Choi, C.W. Kim, K.S. Cho, *Biomaterials* 27 (2006) 3810–3816.
- [43] Y.I. Chung, K.M. Ahn, S.H. Jeon, S.Y. Lee, J.H. Lee, G. Tae, *J. Control. Release* 121 (2007) 91–99.
- [44] F.C.M. Driessens, in: K. De-Groot (Ed.), *Bioceramics of Calcium Phosphate*, CRC Press, Boca Raton, FL 1983, pp. 1–32.
- [45] R.Z. LeGeros, M.A. Miravite, G.B. Quirolgico, M.E.J. Curzon, *Nature* 205 (1965) 403–404.
- [46] R.Z. LeGeros, O.R. Trautz, J.P. LeGeros, E. Klein, *Science* 155 (1967) 1409–1411.
- [47] H. Pan, B.W. Darvell, *Cryst. Growth Des.* 10 (2000) 845–850.
- [48] Z. Schwartz, C.H. Lohmann, J. Oefinger, L.F. Bonewald, D.D. Dean, B.D. Boyan, *Adv. Dent. Res.* 13 (1999) 38–48.
- [49] B.D. Boyan, L.F. Bonewald, E.P. Paschalis, C.H. Lohmann, J. Rosser, D.L. Cochran, D.D. Dean, Z. Schwartz, A.L. Boskey, *Calcif. Tissue Int.* 71 (2002) 519–529.
- [50] R.Y. Kim, J.H. Oh, B.S. Lee, Y.K. Seo, S.J. Hwang, I.S. Kim, *Biomaterials* 35 (2014) 1869–1881.
- [51] U. Noth, R. Tuli, R. Seghatoleslami, M. Howard, A. Shah, D.J. Hall, N.J. Hickok, R.S. Tuan, *Exp. Cell Res.* 291 (2003) 201–211.
- [52] N. Kamiya, T. Kobayashi, Y. Mochida, P.B. Yu, M. Yamauchi, H.M. Kronenberg, Y. Mishina, *J. Bone Miner. Res.* 25 (2010) 200–210.
- [53] N. Kamiya, L. Ye, T. Kobayashi, Y. Mochida, M. Yamauchi, H.M. Kronenberg, J.Q. Feng, Y. Mishina, *Development* 135 (2008) 3801–3811.
- [54] J. Zhao, G. Shen, C. Liu, S. Wang, W. Zhang, X. Zhang, Y.D. Zhang, J. Wei, Z. Zhang, X. Jiang, *Tissue Eng. A* 18 (2012) 185–197.
- [55] J.H. Lee, C.S. Kim, K.H. Choi, U.W. Jung, J.H. Yun, S.H. Choi, K.S. Cho, *Biomaterials* 31 (2010) 3512–3519.
- [56] L.J. Marden, J.O. Hollinger, A. Chaudhari, T. Turek, R.G. Schaub, E. Ron, J. Biomed. Mater. Res. A 28 (1994) 1127–1138.
- [57] C.M. Cowan, T. Aghaloo, Y.F. Chou, B. Walder, X. Zhang, C. Soo, K. Ting, B. Wu, *Tissue Eng.* 13 (2007) 501–512.

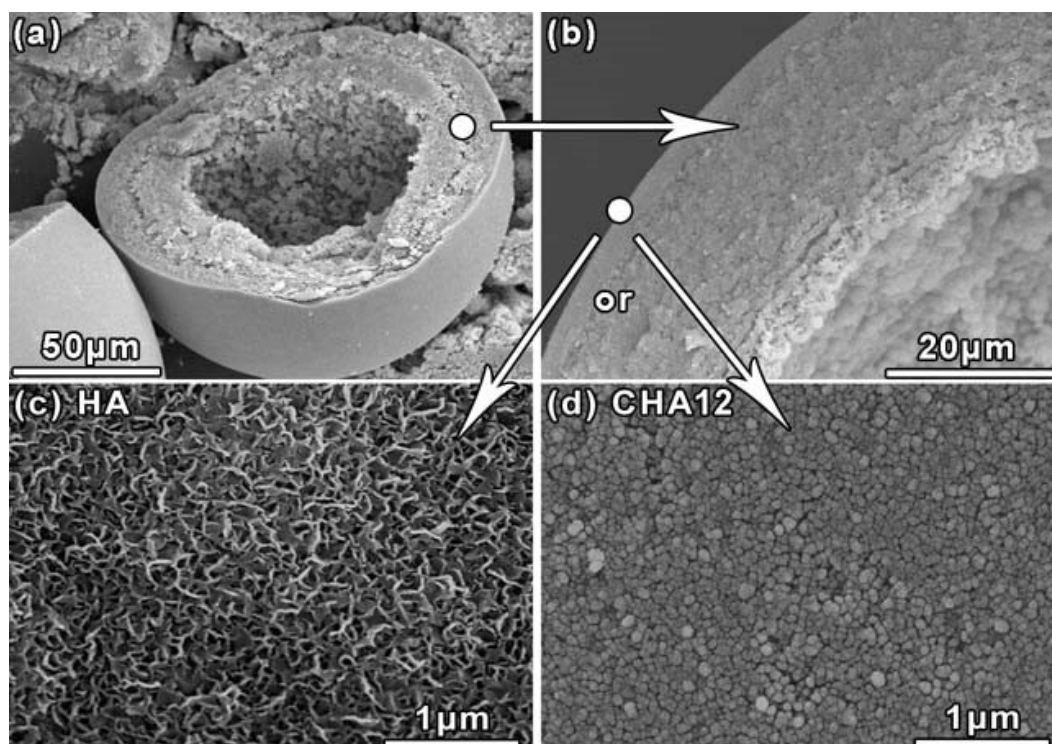


Fig. 1. SEM images of the cross section of a hollow HA microsphere (a, b) and higher magnification images showing differences in surface morphology between the hollow HA and CHA12 microspheres (c, d).

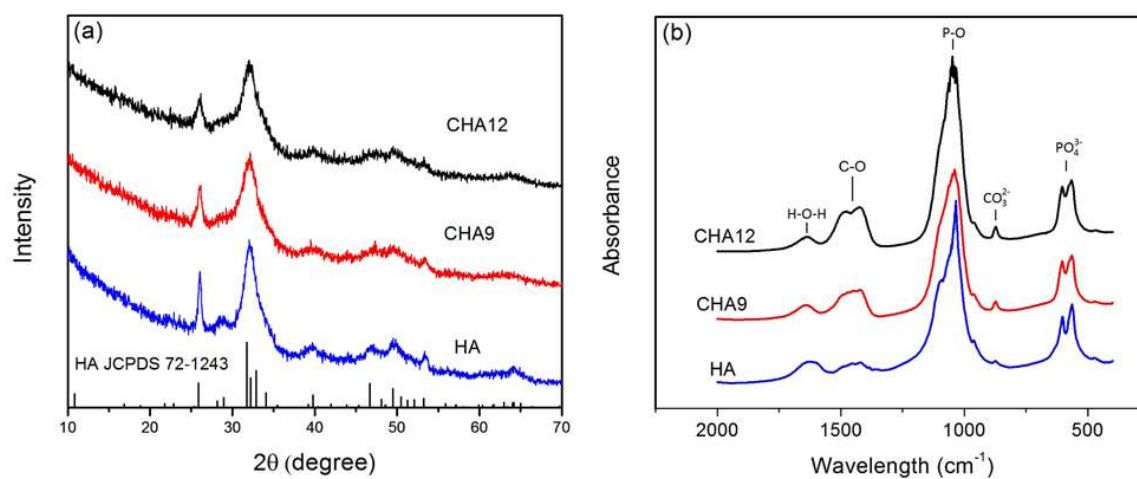


Fig. 2. (a) X-ray diffraction patterns and (b) FTIR spectra of the hollow HA, CHA9 and CHA12 microspheres. The pattern of a reference hydroxyapatite (HA JCPDS 72-1243) is also shown in (a).

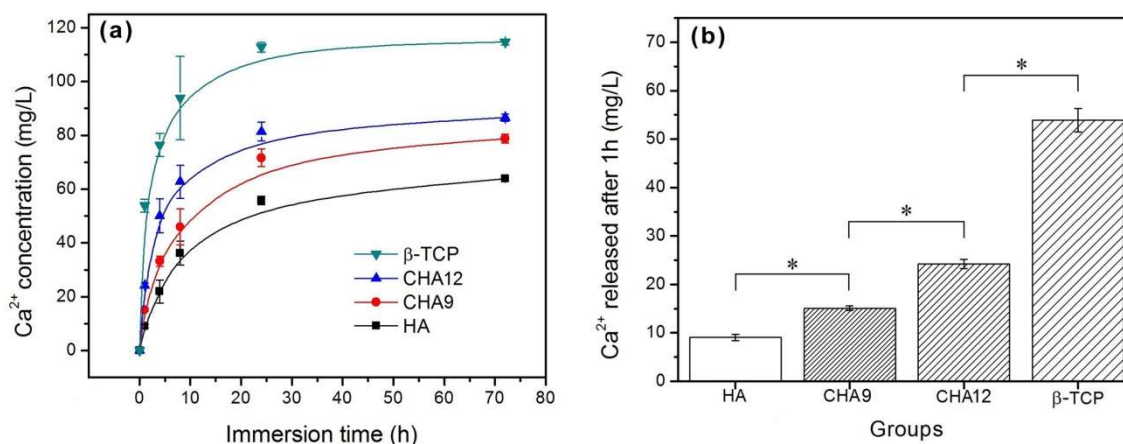


Fig. 3. (a) Cumulative amount of Ca^{2+} ion released from hollow HA, CHA9, and CHA12 microspheres into 0.1 M potassium acetate buffer solution (pH = 5.0; 37 °C) as a function of immersion time. (b) Amount of Ca^{2+} ions released from the three groups of microspheres after 1 h in the buffer solution. For comparison, the release of Ca^{2+} ions from a β -TCP reference material is also shown. (*significant difference between groups; $p < 0.05$).

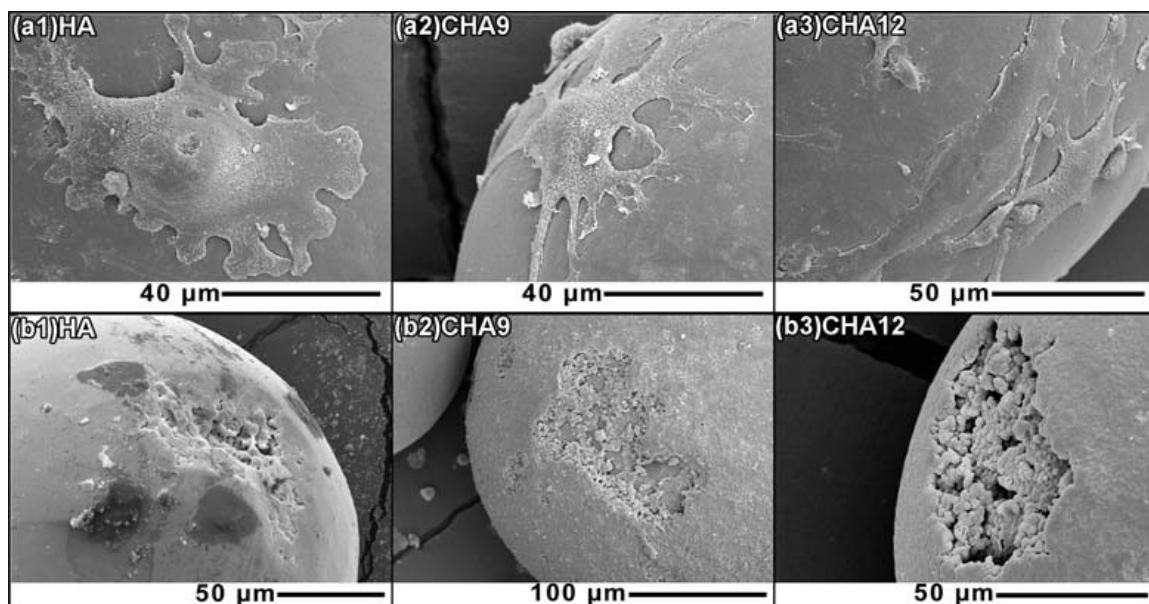


Fig. 4. SEM images of the surface of the HA, CHA9 and CHA12 microspheres after incubation with TIB-71 cells with added RANKL for 1 week (a1–3), and after the cells had been rinsed off (b1–3). (C: cells; P: pitted area after removal of cells).

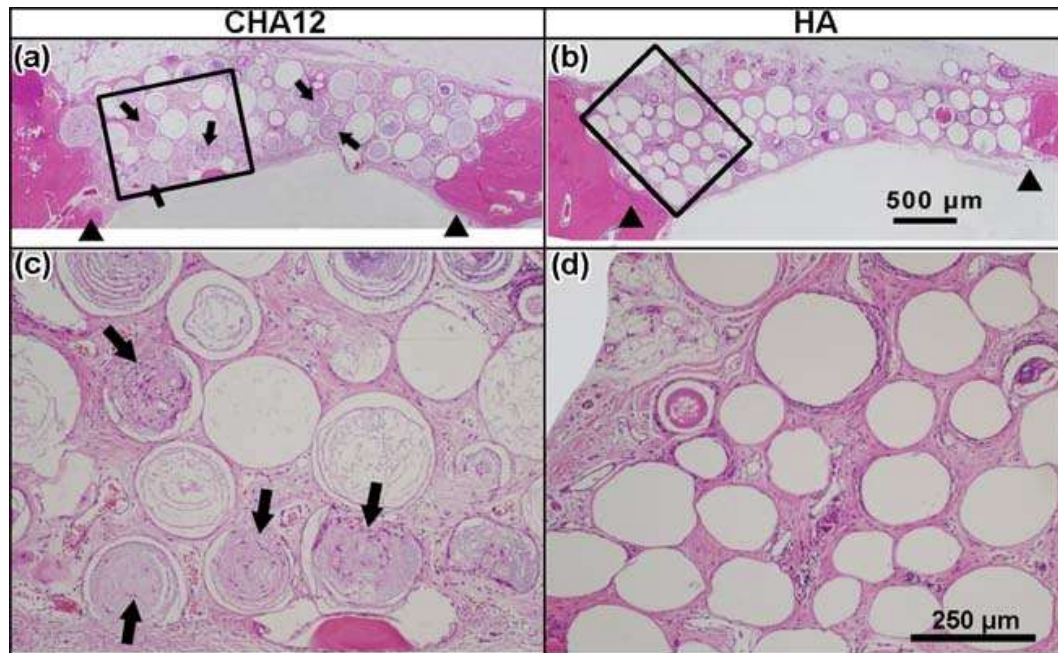


Fig. 5. Transmitted light images of (a, b) H&E stained sections of rat calvarial defects implanted with hollow CHA12 and HA microspheres without BMP2 at 12 weeks postimplantation; (c, d) higher magnification images of the boxed areas in a, b. (Arrowheads: edges of host bone; arrows: open microspheres).

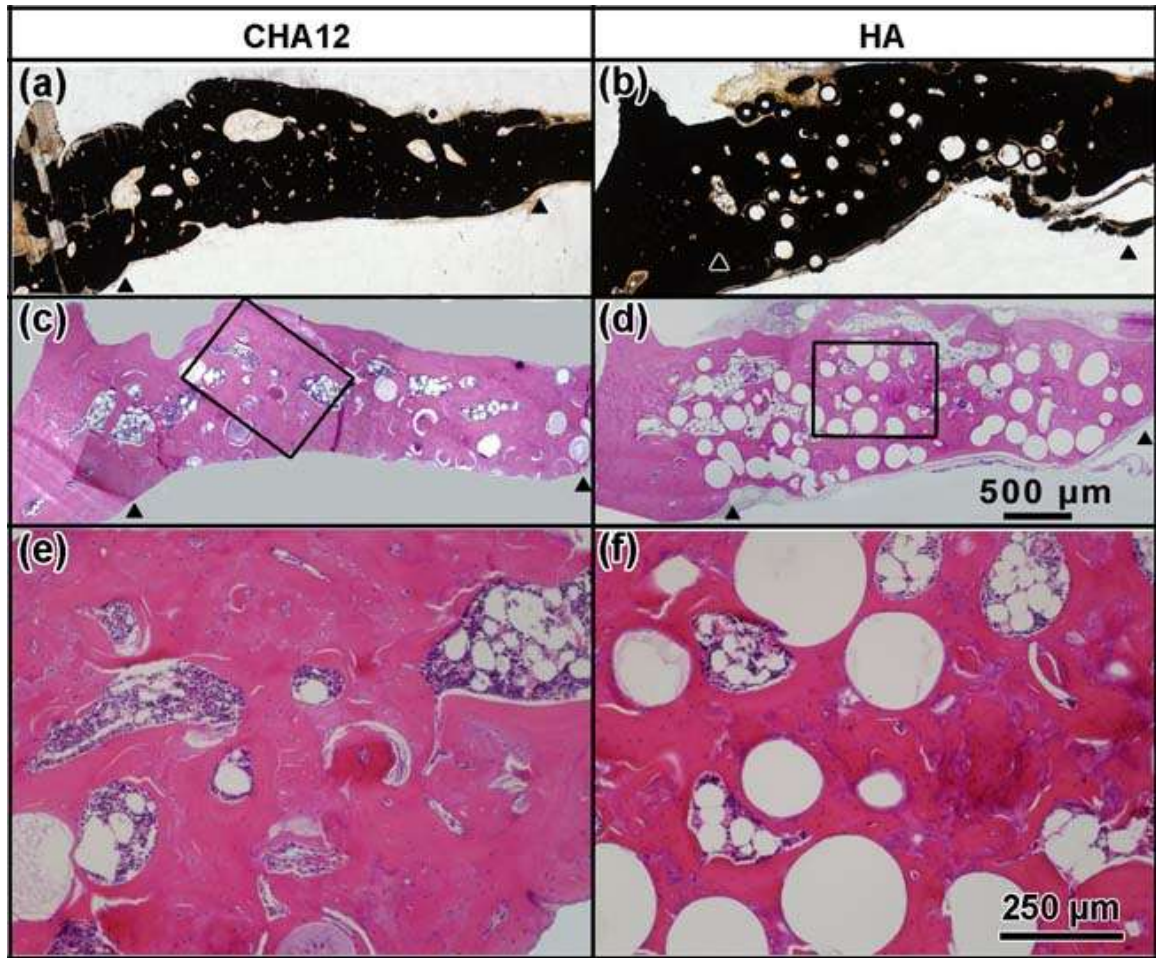


Fig. 6. Transmitted light images of (a, b) von Kossa and (c, d) H&E stained sections of rat calvarial defects implanted with hollow CHA12 and HA microspheres loaded with BMP2 at 12 weeks postimplantation; (e, f) higher magnification images of the boxed areas in c, d. (Arrowheads: edges of host bone).

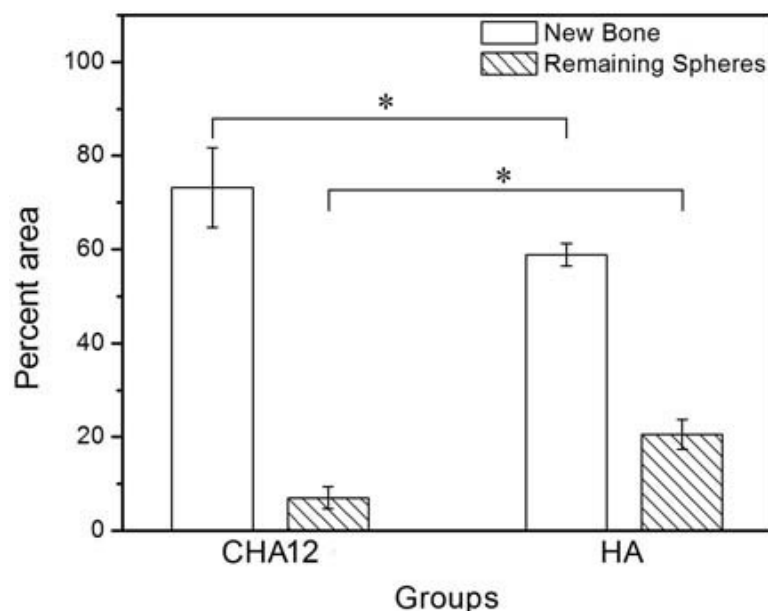


Fig. 7. New bone and residual amount of microspheres, as a percentage of the total defect area, in rat calvarial defects implanted with CHA12 and HA microspheres loaded with BMP2 at 12 weeks postimplantation. (*significant difference between groups; $p < 0.05$)

Table I. Characteristics of hollow hydroxyapatite (HA) and carbonate-substituted hydroxyapatite (CHA) microspheres prepared by converting borate glass microspheres (150–250 μm) in 0.02 M K_2HPO_4 solution containing different concentrations of KHCO_3 at 37 $^\circ\text{C}$. Data for commercial β -TCP granules used as the control group are included for reference.

Microsphere designation	KHCO_3 concentration (M) in solution	CO_3 content of microspheres (wt. %)	Surface area of microspheres (m^2g^{-1})	Average pore size of shell (nm)	Microsphere diameter (μm)
HA	0	2.1 ^a	179	11	150–250
CHA9	0.135	8.6	233	8	150–250
CHA12	0.27	12.4	236	7	150–250
β -TCP			0.30		53–124 ^b

^a Presumably due to dissolved CO_2 in the aqueous medium

^b Granule size

III. Creation of bioactive glass (13-93) scaffolds for structural bone repair using a combined finite element modeling and rapid prototyping approach

Wei Xiao ^a, Mohsen Asle Zaeem ^a, B. Sonny Bal ^b, Mohamed N. Rahaman ^a

^a Department of Materials Science and Engineering, Missouri University of Science and Technology, Rolla, MO 65409, USA

^b Department of Orthopaedic Surgery, University of Missouri, Columbia, MO 65212, USA

ABSTRACT

There is a clinical need for synthetic bioactive materials that can reliably repair intercalary skeletal tissue loss in load-bearing bones. Bioactive glasses have been investigated as one such material but their mechanical response has been a concern. Previously, we created bioactive silicate glass (13–93) scaffolds with a uniform grid-like microstructure which showed a compressive strength comparable to human cortical bone but a much lower flexural strength. In the present study, finite element modeling (FEM) was used to re-design the scaffold microstructure to improve its flexural strength without significantly lowering its compressive strength and ability to support bone infiltration in vivo. Then scaffolds with the requisite microstructures were created by a robotic deposition method and tested in four-point bending and compression to validate the FEM simulations. In general, the data validated the predictions of the FEM simulations. Scaffolds with a porosity gradient, composed of a less porous outer region and a more porous inner region, showed a flexural strength (34 ± 5 MPa) that was more than twice the value for the uniform grid-like microstructure (15 ± 5 MPa) and a higher compressive strength (88 ± 20 MPa) than the grid-like microstructure (72 ± 10 MPa). Upon implantation of the scaffolds for 12 weeks in rat calvarial defects in vivo, the amount of new bone that infiltrated the pore space of the scaffolds with the porosity gradient ($37 \pm 16\%$) was similar to that for the grid-like scaffolds ($35 \pm 6\%$). These scaffolds with a porosity gradient that better mimics the microstructure of human long bone could provide more reliable implants for structural bone repair.

1. Introduction

The repair of large structural bone defects such as segmental defects in the long bones of the limbs is a challenging clinical problem [1]. In comparison, small, contained bone defects are repairable with commercially available osteoconductive and osteoinductive filler materials [2,3]. To treat structural bone loss, clinicians use bone allografts, autografts and porous metals. These materials are limited by cost, availability, durability, infection risk, donor site morbidity, and uncertain healing. Consequently, there is a clinical need for synthetic bioactive implants that can reliably repair intercalary skeletal tissue loss in load-bearing bones.

Bioactive glasses have been investigated as one such material since they are osteoconductive, convert to hydroxyapatite in vivo, heal readily to host bone and soft tissues, and they are amenable to fabrication into porous three-dimensional (3D) architectures [4–8]. In the form of particles and weak scaffolds, bioactive silicate glasses such as the glasses designated 45S5 and 13–93 are approved by the Food and Drug Administration (FDA) for in vivo use, and they are used clinically to reconstitute non-structural bone defects [8].

Advances in rapid prototyping techniques (also referred to as solid freeform fabrication or additive manufacturing) have resulted in more innovative design and unprecedented control of scaffold microstructures [9]. Recent studies have shown the ability to create porous 3D scaffolds of bioactive silicate glasses (13–93 and 6P53B) with compressive strength comparable to human cortical bone using rapid prototyping methods [10–15]. Our previous study showed that 13–93 bioactive glass scaffolds, created with a uniform grid-like microstructure by robocasting, had a compressive strength (86 ± 9 MPa) and an elastic modulus (13 ± 2 MPa) comparable to the human cortical bone [13]. In comparison, the flexural strength of the scaffolds (11 ± 3 MPa) was much lower than cortical bone (~ 100 MPa). While those scaffolds showed the capacity to heal critical size segmental defects in rat femurs [16], improvement in their flexural strength could alleviate concerns about their mechanical reliability in vivo.

Finite element modeling (FEM) has been widely used to analyze the mechanical response of biomaterials [17–20]. In a recent study, FEM was used to simulate the mechanical response of models composed of hydroxyapatite or beta-tricalcium phosphate

with a cubic geometry and uniform grid-like structure [17]. Regions of the structure with the highest local stress were determined under loading in compression, tension or shear and used to predict the strength of scaffolds with the same grid-like microstructure. Scaffolds created by a robocasting method were tested in compression to validate the FEM simulations. However, the FEM analysis and mechanical testing were limited to a cubic geometry and a uniform grid-like structure. The mechanical response of alternative geometries relevant to bending (flexure), an important loading mode in structural bone, and alternative structures relevant to the non-uniform microstructure of human long bones were not analyzed or tested.

The cross section of long bones of the limbs has a non-uniform microstructure, composed of a less porous outer region of cortical bone (porosity = 5–10%) and a more porous inner region of trabecular bone (porosity = 50–90%). As outlined above, our previous studies showed that a uniform grid-like microstructure provided bioactive glass (13–93) scaffolds with promising compressive strength and capacity to support bone infiltration but a flexural strength that was much lower than cortical bone [13,21,22]. Because the uniform grid-like microstructure is limited in its ability to mimic the microstructure of human long bones, an investigation of alternative microstructures is warranted. When compared to an approach based on trial-and-error experiments, FEM simulations could provide a more efficient approach to predict the mechanical response of a variety of alternative microstructures.

The objective of the present study was to re-design the uniform grid-like microstructure used in our previous studies and determine whether alternative microstructures can impart higher flexural strength to 13–93 glass scaffolds without compromising their compressive strength and ability to support bone infiltration. FEM was used to simulate the mechanical response in flexure and compression for models with a variety of structures. Then scaffolds with the optimal microstructures predicted by FEM were created by robocasting and tested in four-point bending and in compression to validate the predictions of the FEM simulations. Scaffolds with the optimal microstructures were also implanted for 12 weeks in rat calvarial defects to evaluate their ability to support bone infiltration *in vivo*.

2. Materials and methods

2.1 Design of scaffold architecture

A uniform grid-like microstructure, in which the glass filaments in adjacent layers were arranged at right angles with reference to the x and y axes, was used as the reference structure and our approach was to modify the spatial arrangement of the filaments. The diameter of the glass filaments (330 μm) used in the FEM simulations was the same as the filaments in the uniform grid-like scaffolds created by robocasting in our previous studies [13,16,21,22]. In view of our interest in improving the flexural strength of the bioactive glass scaffolds while maintaining the promising compressive strength, the flexural mechanical response of the structures was analyzed first. Then the response of selected structures was analyzed in compression.

For the FEM analysis in flexure, a beam was selected as the macroscopic external shape of the physical model because this geometry is commonly used in the measurement of flexural strength by four-point bending. The external dimensions of the model (Fig. 1) were selected to avoid the use of excessive computing power and time. However, the dimensions of the model were still large enough to allow the use of enough layers to create a porosity gradient in the structure and to create scaffolds with similar dimensions for experimental four-point bending tests.

Each model was composed of 13 alternating orthogonal layers of parallel filaments. The length and angle of the filaments and the spacing between the parallel filaments were defined for each layer. With different arrangements of the filaments in each layer, 11 different 3D models were designed (Table I). The models all had the same external dimensions. Ten models were composed of 7 layers of short (S) filaments along the x axis and 6 layers of long (L) filaments along the y axis. The assignments L1 to L4 were used to describe the arrangement of the long filaments while S1 to S3 were used to describe the arrangement of the short filaments. For example, L3S1 designated the model in which the long filaments had the L3 arrangement and the short filaments, orthogonal to the long filaments, had the S1 arrangement. In the eleventh model, designated S45°, the filaments in the adjacent layers were arranged at 45° to the x and y axes. In this model, the 13 alternating orthogonal layers consisted 4 layers each with a lower porosity on the top and the bottom of the model and 5 layers with a higher porosity in the middle. Except

for the L4S1 model, all the models had the same porosity (~43% as determined from the models by the software). For the L4S1 model, additional long filaments were added to the two outermost layers of the L1S1 structure, resulting in a lower porosity (~33%). The center-to-center distance between adjacent filaments in each layer of the models is given in Table II.

Based on the results of FEM simulations in flexure, 3 models were selected for analysis in compression. Models with the L3S1 and L4S1 structures were selected because the FEM simulations showed that these structures had a higher flexural strength than the uniform grid-like L1S1 structure. In addition, the uniform grid-like L1S1 structure was analyzed for comparison. Each model was composed of 19 alternating orthogonal layers of parallel filaments (Fig. 2). All three models had the same external shape (a cube with each side equal to ~5 mm). The glass filaments were identical to those described for the flexural analysis. The cross sections of the structures (xy plane) were identical to the L1S1, L3S1 and L4S1 models and the load was applied in the z direction.

2.2 Finite element simulations

Finite element simulations were carried out using ABAQUS/CAE 6.12-1 software (Dassault Sytemes Simulia Corp., Providence, RI). All 11 models in Table I were analyzed in flexure while the 3 models in Fig. 2 were analyzed in compression. The filaments in all the models were assumed to be composed of a dense homogeneous material with a Young's modulus of 70 GPa and a Poisson's ratio of 0.25, values which are comparable to those of a silicate glass [23].

For the simulations in flexural loading, 4 rigid cylinders with a diameter of 2.0 mm were generated to simulate the fixture used in the four-point bending test (Fig. 3). The two upper cylinders, each 5 mm from the midline, served as the inner span, while the two lower cylinders, 10 mm from the midline, served as the outer span. The cylinders were in contact with the model from the beginning of the simulations. Furthermore, the contact between the cylinders and the model was assumed to be hard (no interpenetration between the materials) and frictionless. For the simulations in compression, two rigid planes were generated to simulate the platens used in a compression test. The planes were

in contact with the scaffold from the beginning of the simulation, and the contact between the planes and the scaffold was also assumed to be hard and frictionless.

The models were partitioned into several parts in order to improve the meshing and apply the proper boundary conditions. The FEM models were discretized with an approximate mesh size of 120 μm , and quadratic tetrahedral elements were used. For the simulations in flexural loading, each of the models with the same porosity contained $\sim 1.4 \times 10^6$ elements, while L4S1 contained $\sim 1.7 \times 10^6$ elements. Different element sizes were used to test the convergence of the FEM simulations. Smaller element sizes produced approximately the same results but they required a much longer time to complete the simulation. The element size used in this study provided a good balance between computing time and the results. The middle of the cross section perpendicular to x axis was fixed at the x axis direction ($U_1=0$) to prevent the scaffold from sliding in the x axis direction, while the middle of the cross section perpendicular to y axis was fixed at the y axis direction ($U_2 = 0$) to prevent sliding in the y axis direction during bending. The two lower cylinders of the fixture were fixed in all directions ($U_1=U_2=U_3=0$) and an evenly distributed load of 100 N was applied to the two upper cylinders through a static, general step with default time duration of 1 s.

For the simulations in compression, the L1S1 and L3S1 models contained $\sim 0.4 \times 10^6$ elements, while L4S1 model contained $\sim 0.5 \times 10^6$ elements. The middle of the cross section perpendicular to the x axis was fixed at the x axis direction ($U_1 = 0$), while the middle of the cross section perpendicular to y axis was fixed at the y axis direction ($U_2=0$). The bottom plane was fixed in all directions ($U_1=U_2=U_3=0$) and an evenly distributed load of 1500 N was applied to the top plane through a static, general step with default time duration of 1 s. The load was applied in the z direction (Fig. 2) which corresponds to the loading mode of an actual scaffold implanted in a segmental defect in the long bones of the limbs.

A desktop computer with 16 CPU cores and 128 GB of RAM were used for the simulations. A typical CPU time to complete a simulation was ~ 4 h and ~ 1 h, respectively, for bending and compression. As a brittle material, glass can withstand much higher stresses in compression than in tension. Consequently, the highest tensile stress within the inner span of the model was used as the primary parameter in the

flexural strength analysis. The compressive strength analysis focused on locating the highest tensile stress through the whole scaffold.

2.3 Experimental four-point bending and compression tests

The scaffolds (L1S1) with a uniform grid-like microstructure were fabricated using the same method described in detail in our previous study [13]. Briefly, the as-received 13–93 glass (Mo-Sci Corp., Rolla, MO) was ground to form particles ($\sim 1 \mu\text{m}$), mixed with a 20 wt% Pluronic-127 binder solution to form a paste (40 vol% glass particles) and extruded using a robocasting machine (RoboCAD 3.0; 3-D Inks, Stillwater, OK). After drying at room temperature, the scaffolds were heated in O_2 at a rate of $0.5 \text{ }^\circ\text{C min}^{-1}$ to $600 \text{ }^\circ\text{C}$ to burn out the processing additives and sintered for 1 h at $700 \text{ }^\circ\text{C}$ (heating rate = $5 \text{ }^\circ\text{C min}^{-1}$) to densify the glass filaments.

Based on the results of the FEM simulations, 5 groups of scaffolds with the designation L1S3, L3S3, L3S1, L4S1 and S45° were also created using this method for mechanical testing in flexure. Three groups of scaffolds, with microstructures corresponding to L1S1, L3S1 and L4S1 designations, were created using the same method for testing in compression. The porosity of the fabricated scaffolds, measured using the Archimedes method, was the same as the porosity of the models. The scaffolds were stored in a desiccator prior to testing to avoid degradation by water vapor in the atmosphere and they were tested in the as fabricated state (without any machining) to avoid introducing strength-limiting flaws due to machining.

Flexural testing of the scaffolds in four-point bending was performed on a fully articulated fixture (outer span = 20 mm; inner span = 10 mm) at a crosshead speed of 0.2 mm min^{-1} using a 2 kN load cell. The stress was applied in the z direction (the same direction used in the FEM simulations). Ten samples of each group with the same dimensions as the models ($23.0\text{mm} \times 4.7\text{mm} \times 3.2\text{mm}$) were tested according to the procedure described in ASTM C1674-11 and the flexural strength was determined from the equation

$$\sigma = \frac{3PL}{4bd^2} \quad (1)$$

where P is the applied load, L is the outer span, b is the sample width, and d is the thickness of the sample.

The Weibull modulus of the scaffolds with the L3S1 and L4S1 architectures was determined by analyzing the flexural strength of thirty samples. According to ASTM C1239-07, the flexural strength data were fitted with the equation

$$\ln \ln \left(\frac{1}{1-P_f} \right) = m \ln \left(\frac{\sigma}{\sigma_0} \right) \quad (2)$$

where P_f is the probability of failure at a stress σ , the normalizing stress σ_0 is the Weibull scale parameter determined from the intercept of the fit to the data, and the Weibull modulus m is the slope of the straight line fit. The value σ_0 is also the stress at which the probability of failure is 63%. The value of P_f was determined using the equation

$$P_f = \frac{i - 0.5}{n} \quad (3)$$

where n is the total number of specimens tested and i is the specimen rank in ascending order of failure stresses.

After testing, the fractured surfaces of the samples were coated with Au/Pd and examined in a scanning electron microscope, SEM (S-4700; Hitachi, Tokyo, Japan). The fracture morphology, particularly of the bottom and top filaments of the scaffolds, subjected to tensile and compressive stresses in the four-point bending test, was examined.

Testing in compression was performed between two metal platens at a cross-head speed of 0.5 mm min^{-1} using a 10 kN load cell. Deformation of the sample was determined from the movement of the crosshead. The load was applied along the z axis, the same direction used in the simulations. Ten samples in each group, with the same dimensions as the models ($5 \text{ mm} \times 5 \text{ mm} \times 5 \text{ mm}$), were tested.

2.4 Animal surgery

Scaffolds with the shape of discs (4.6 mm in diameter \times 1.5 mm) and microstructures corresponding to the L1S1, L3S1 and L4S1 designations were created using the same robocasting method described earlier for implantation in rat calvarial defects in vivo (Fig. 4). The circumferential area of the scaffold in contact with host

calvarial bone corresponded to the cross-section that would be in contact with host bone in a segmental defect of the long bones of the limbs. Each scaffold was composed of 7 layers of orthogonal filaments which resulted in a thickness that was approximately equal to the thickness of the calvarial defect (~ 1.5 mm).

All animal experimental procedures were approved by the Animal Care and Use Committee, Missouri University of Science and Technology, in compliance with the NIH Guide for Care and Use of Laboratory Animals (1985). Eleven Sprague Dawley rats (3 months old; 350 ± 50 g; Harlan Laboratories Inc., USA) were maintained in the animal facility for 2 weeks to become acclimated to diet, water and housing under a 12 h/12 h light/dark cycle. The rats were anesthetized with an intramuscularly injected mixture of ketamine and xylazine ($1.5 \mu\text{l kg}^{-1}$). The surgical area was shaved, scrubbed with 70% ethanol and iodine and draped. With sterile instruments and an aseptic technique, a cranial skin incision was sharply made in an anterior to posterior direction along the midline. The subcutaneous tissue, musculature and periosteum were dissected and reflected to expose the calvarium. Bilateral full-thickness defects 4.6 mm in diameter were created in the central area of each parietal bone using a phosphate-buffered saline (PBS)-cooled trephine drill without disturbing the dura mater. The sites were constantly irrigated with sterile PBS to prevent overheating of the bone margins and to remove the bone debris. The bilateral defects were randomly implanted with 7 replicates per group (L1S1, L3S1 and L4S1). The number of replicates per group ($n = 7$) was based on our previous studies [21]. The periosteum and skin were repositioned and closed using wound clips. The animals were given a dose of ketoprofen (3 mg per kg mass of the animal) intramuscularly and 0.2 ml penicillin subcutaneously post-surgery, and they were monitored daily for the condition of the surgical wound, food intake, activity and clinical signs of infection. At 12 weeks, the animals were sacrificed by CO_2 inhalation and the calvarial defects with surrounding bone and soft tissue were harvested for subsequent evaluation.

2.5 Histology and histomorphometric analysis

The harvested calvarial samples were fixed in 10% formaldehyde for 5 days, washed with deionized water and then cut in half. Half of each sample was for paraffin

embedding while the other half was for polymethyl methacrylate (PMMA) embedding. The samples for paraffin embedding were de-siliconized by immersion for 2 h in 10% hydrofluoric acid, decalcified in 14% ethylenediaminetetraacetic acid (EDTA) for 4 weeks, dehydrated in a graded series of ethanol and embedded in paraffin using routine histological techniques. Then the samples were sectioned to 5 μm using a microtome and stained with hematoxylin and eosin (H&E). The undecalcified samples were dehydrated in a graded series of ethanol and embedded in PMMA. Sections were affixed to acrylic slides, ground down to 40 μm using a surface grinder (EXAKT 400CS, Norderstedt, Germany) and stained using the von Kossa method. Transmitted light images of the stained sections were taken with an Olympus BX 50 microscope connected to a CCD camera (DP70, Olympus, Japan).

Histomorphometric analysis was carried out using optical images of the stained sections and the ImageJ software (National Institutes of Health, USA). One section across the diameter of each defect was analyzed. The percent new bone formed in the defects was evaluated from the H&E stained sections. The entire defect area was determined as the area between the two defect margins, including the entire glass scaffold and the tissues within. The available pore area within the scaffold was determined by subtracting the area of the bioactive glass scaffold from the total defect area. The newly formed bone were then outlined and measured. The von Kossa-positive area was determined from the von Kossa stained sections, which yielded the combined amount of mineralized bone and hydroxyapatite converted from the glass as both bound the silver nitrate.

2.6 Statistical analysis

The data are presented as a mean \pm standard deviation (SD). Analysis for differences in the maximum applied load, flexural strength, compressive strength, new bone area and mineralization between groups was performed using one-way analysis of variance (ANOVA) with Tukey's post hoc test. Differences were considered significant for $p < 0.05$.

3. Results

3.1 Finite element simulation of four-point bending

The deformation of the L1S1 model (uniform grid-like structure) in four-point bending is shown in Fig. 5, with a scale factor of 30 (i.e., the deformation has been magnified 30 times for ease of observation). Similar deformation profiles were found for other structures. According to the maximum principal stress theory (Tresca), failure will occur when the maximum principal stress in a system reaches the value of the maximum stress at the elastic limit in simple tension, which is approximately correct for brittle materials such as glass. Consequently, the maximum principal stress (S, Max. Principal (Abs.)) was evaluated and the results are shown in color as represented by the scale in Fig. 5. The top layers of the scaffold had a negative tensile stress because they were in compression. The highest tensile stress was in the bottom layers and it decreased with distance above the bottom of the model. Particular attention was paid to differences in the magnitude and distribution of the stress in the bottom layers of the various models.

The magnitude and distribution of the tensile stress near the middle of the two or three bottom layers of the L1S1, L1S3, L3S1 and L4S1 models are shown in Fig. 6. For the L1S1 model (Fig. 6a), corresponding to the uniform grid-like microstructure used in our previous experimental studies [13,16,21,22], the tensile stress was generally uniform over most of the area of the long filaments (green color). However, a higher tensile stress (weak yellow color) was found in the regions of the long filaments near the interfaces between the long filaments and the short filaments in the adjacent layer. When compared to the L1S1 model, under the same applied load, the stress in the long filaments of the L1S3 model showed approximately the same distribution but the magnitude of the tensile stress was several times higher (Fig. 6b). In comparison, the tensile stress in the filaments of the L3S1 model (Fig. 6c) was lower than the L1S1 model while the L4S1 model (Fig. 6d) showed even smaller tensile stresses in the filaments than the L3S1 model.

Based on the color scheme and the stress scale (Fig. 6), the highest tensile stress in the middle region of the bottom layers are shown in Fig. 7 for the different models analyzed. For the nine LiSi models ($i = 1-3$) which have the same porosity, redistributing the short filaments from the middle region of the model to the top and bottom layers

resulted in a higher tensile stress. For the same number of long filaments, the highest tensile stress was in the order $S1 < S2 < S3$. Redistributing the long filaments from the middle region to the top and bottom layers of the model resulted in a smaller maximum tensile stress in the model, according to the order $L1 > L2 > L3$. For the L4S1 model which had a lower porosity due to a larger number of long filaments, the highest tensile stress in the bottom filaments was even lower than the L3S1 model. The tensile stress in the bottom filaments of the L3S1 and L4S1 models were 25% and 44% lower, respectively, than the L1S1 model. In comparison, the S45° model (filaments at 45° to the x and y axes) showed a tensile stress in the bottom filaments that was ~210% higher than the L1S1 model. Overall, for the same applied load, the L4S1 and L3S1 models showed the lowest tensile stress in the bottom filaments while the L1S3 model showed the highest tensile stress for the ten LiSi models analyzed. The S45° model showed the highest tensile stress among all eleven models.

3.2 Measured flexural strength of scaffolds in four-point bending

The cross sections of the as-fabricated scaffolds with the L1S1, L3S1 and L4S1 microstructures, created using robocasting, are shown in Fig. 8 in the plane perpendicular to the long filaments. In general, the microstructures of the as-fabricated scaffolds corresponded well to the model structures used in the FEM analysis. For the scaffold with the L3S1 microstructure (Fig. 8b), some sagging of the short glass filaments right above the layers with the smallest number of long filaments (the layers with the largest spacing between the long filaments) was observed. In comparison, no sagging was observed in the L1S1 and L4S1 microstructures, presumably because the long filaments in all the layers were close enough to provide adequate support for the short layers.

In the four-point bending test, the maximum load at failure for the scaffolds with the L1S3, L3S3, L1S1, L3S1, L4S1 and S45° microstructures are summarized in Fig. 9a while the flexural strength, determined using Equation 1, are shown in Fig. 9b. When compared to the uniform grid-like (L1S1) microstructure studied previously (flexural strength = 15 ± 5 MPa), the L1S3 microstructure showed the lowest flexural strength (10 ± 4 MPa) while the flexural strength of the L3S3 microstructure (16 ± 4 MPa) was not significantly different. In comparison, the L3S1 microstructure showed the highest

flexural strength (22 ± 3 MPa) among the microstructures with same porosity ($\sim 43\%$), and it was significantly higher ($\sim 50\%$ higher) than the L1S1 microstructure. The flexural strength of the L4S1 microstructure, with a lower porosity ($\sim 33\%$), showed the highest flexural strength (34 ± 5 MPa) which was also significantly higher ($\sim 130\%$ higher) than the L1S1 architecture. The flexural strength of the S45° microstructure (14 ± 3 MPa) was not significantly different from L1S1 and L3S3 microstructures.

Figure 10a, b shows Weibull plots of the flexural strength data for scaffolds with the L3S1 and L4S1 microstructures. The straight line fit to the data was obtained using a least-squares method. The data points within most of the stress range were well fitted by the straight line ($R^2 = 0.95$ or 0.96) but there was some deviation at the lowest and highest stress values. The Weibull modulus m and the normalizing stress σ_0 were determined from the slope and intercept of the straight line fit. The results showed that $m = 9$ and $\sigma_0 = 23$ MPa for the LS31 microstructure, and $m = 8$ and $\sigma_0 = 36$ MPa for the L4S1 microstructure. In comparison, four-point bending tests in our previous study showed that $m = 6$ and $\sigma_0 = 12$ MPa for the uniform grid-like scaffolds with the L1S1 microstructure [13].

SEM images of fractured surfaces of the scaffolds with the L3S1 and L4S1 microstructures from the four-point bending tests are shown in Fig. 11. Features such as hackle region, mist region, smooth mirror region and arrest lines [24], similar to those observed previously for the L1S1 microstructure [13], were found on the fractured surface of both samples. The origin of failure of some glass filaments was determined using fractography guidelines. By outlining the mist region with a circle, the failure origin is commonly at the center of the circle, while the hackle lines commonly point to the origin. However, it was difficult to locate the initial failure origin of the scaffold itself. Cantilever curls observed near the top region of the fractured surface often indicate regions of compression in flexural testing of brittle solids [24].

3.3 Finite element simulations and testing in compression

For each of the three models (L1S1, L3S1 and L4S1 structures), the filaments in all the layers in the xy plane showed a similar color distribution when subjected to the

same applied load, indicating no discernible difference in the stress in each layer (Fig. 12a,b,c). For all three groups, colors (yellow to red) representing higher tensile stress were found in the regions where the filaments parallel to the x direction were bonded to the filaments in the z direction (Fig. 12a1, b1, c1). The models with the L1S1 and L3S1 structures did not show any observable difference in color (stress) in those regions whereas the L4S1 showed colors (green to yellow) that corresponded to a smaller tensile stress.

In general, the measured compressive strengths of the scaffolds (L1S1, L3S1 and L4S1 microstructures) were compatible with the predictions of the FEM simulations. The compressive strength of the scaffolds with the L3S1 microstructure (71 ± 20 MPa) was approximately equal to that for the scaffolds with the uniform grid-like (L1S1) microstructure (72 ± 10 MPa) (Fig. 13). In comparison, the compressive strength of the scaffolds with the L4S1 microstructure (88 ± 20 MPa) was $\sim 22\%$ higher. The higher compressive strength observed for the scaffold with the L4S1 microstructure was presumably due to its lower porosity (33% compared to 43% for the L1S1 and L3S1 microstructures). (See Fig. 14.)

3.4 Assessment of bone regeneration

Transmitted light images of H&E stained sections of the rat calvarial defects implanted for 12 weeks with the three groups of scaffolds having the L1S1, L3S1 and L4S1 microstructure are shown in Fig. 14a1,b1,c1. New bone infiltrated all three groups of scaffolds, into the edges (periphery) adjacent to the host bone and into the pores, indicating good integration of the scaffolds with the surrounding calvarial bone regardless of the difference in microstructure. The amount of new bone that infiltrated the three groups of scaffolds are shown separately in Fig. 15 as a percentage of the total defect area and the total pore area of the scaffolds. The amount of new bone that infiltrated the scaffold with the uniform grid-like microstructure (L1S1) was $15 \pm 3\%$ based on the total defect area. This value is not significantly different from the values found in our previous studies for scaffolds with the same microstructure and for the same animal model [21, 22]. In comparison, the amount of new bone that infiltrated the scaffolds with the L3S1 and L4S1 microstructures was $19 \pm 5\%$ and $9 \pm 5\%$ respectively,

respectively. However, the differences among the three groups were not statistically significant. Because the scaffolds had different microstructures, the amount of new bone as percentage of the total pore area was also evaluated. The values were $35 \pm 6 \%$, $36 \pm 10 \%$ and $37 \pm 16 \%$, respectively, for scaffolds with the L1S1, L3S1 and L4S1 groups. These values show that based on the available pore space, there was no difference in the capacity of the groups of scaffolds to support bone infiltration.

Transmitted light images of von Kossa stained sections of the rat calvarial defects implanted for 12 weeks with the three groups of scaffolds are shown in Fig. 14a2,b2,c2. The von Kossa staining detects a combination of bone and glass converted to hydroxyapatite (phosphate material). The total von Kossa positive area, evaluated as a percentage of the total defect area, was $37 \pm 7 \%$, $36 \pm 5 \%$ and $32 \pm 4 \%$, respectively, for scaffolds with the L1S1, L3S1 and L4S1 microstructures (Fig. 15). There was no significant difference among the values. Subtracting the percentage of new bone (based on the total defect area), the amount of the scaffold that converted to hydroxyapatite in the twelve-week implantation period was 22%, 17% and 23%, respectively, for the scaffolds with the L1S1, L3S1 and L4S1 microstructures.

4. Discussion

Strong porous scaffolds of silicate 13-93 bioactive glass are showing promise as a synthetic biomaterial in healing structural bone defects. Scaffolds with a uniform grid-like microstructure and a compressive strength comparable to human cortical bone have shown the capacity to heal critical size segmental defects in rat femurs [16]. However, the low flexural strength of those scaffolds (11 ± 3 MPa) found in a previous study [13] is a concern because bending is an important loading mode in structural bone. In the present study, we used a combined approach consisting of FEM simulations and experimental testing to identify alternative microstructures with improved flexural strength. Redistribution of the glass filaments in the uniform grid-like microstructure to form a porosity gradient that better mimics human long bones resulted in scaffolds with significantly higher flexural strength. Furthermore, the scaffolds with the gradient porosity retained the high compressive strength of the uniform grid-like scaffolds and

their ability to support bone infiltration. These scaffolds could provide more reliable bioactive glass implants for structural bone repair.

4.1 FEM simulations

The FEM analysis in the present study focused on simulating the flexural mechanical response of porous 3D scaffolds with microstructures based on a grid-like arrangement of glass filaments. A grid-like arrangement was used because our previous experiments showed that scaffolds composed of a uniform grid-like microstructure had the requisite compressive strength (comparable to cortical bone) as well as the capacity to support bone infiltration in vivo. However, the flexural strength of the scaffolds was much lower than cortical bone. One objective was to determine whether a redistribution or rearrangement of the filaments in the grid-like microstructure could lead to an improvement in the flexural strength. FEM provided an efficient approach to simulate the mechanical response of a variety of microstructures.

The uniform grid-like model used as a reference was composed of filaments arranged orthogonally in the x and y directions. Maintaining the grid-like arrangement and total porosity but rearranging the filaments orthogonally at 45° to the x and y directions (the S45° model) resulted in higher tensile stresses in the bottom layers of the model. Consequently, the simulations focused on retaining the arrangement of the filaments in the x and y direction but redistributing the filaments to form a gradient microstructure. The simulations served as a guide for comparing the mechanical response of a variety of models and reduced the time required in an approach based solely on experimental trial-and-error.

In a four-point bending test, the bottom layer in the middle part between the inner span is subjected to the highest tensile stress. As the structure is assumed to fail when the stress exceeds the tensile strength of the glass filaments, the stress in that region of the model was a major consideration in the simulations. For models with the same porosity ($\sim 43\%$), the simulations showed that redistributing some long filaments from the two interior layers to the top and bottom layers resulted in a lower tensile stress in the long filaments of the lowest layer (where the tensile stress is greatest). The tensile stress generated in the L2S1 and L3S1 models was lower (by 6% and 25%, respectively) when

compared to the L1S1 model. As the structure is assumed to fail when the stress exceeded the tensile strength of the glass filaments, a reduction in the tensile stress is indicative of an increase in the flexural strength for identical systems.

By taking the L3S1 model and adding long filaments to the second layer from the top and bottom also, thereby increasing the total number of long filaments and the density of the model, a further reduction in the tensile stress of the bottom layers was achieved. The tensile stress in the bottom layer of the L4S1 model was 44% lower than the L1S1 model. The tensile stress in the bottom layer is distributed among a larger number of filaments (or a denser region), resulting in a lower stress in the individual filaments.

Redistributing some of the short filaments from the middle region of the model to the top and bottom layers resulted in an increase in the tensile stress of the bottom layer. As the short filaments are parallel to the cylinders that apply the load to the model, a larger number of short filaments created more interfaces with the long filaments. The decrease in the flexural strength might be related to the change in the projected area of the applied load on the short filaments and the number of interfaces between the short and long filaments in the bottom layer.

Some assumptions in the FEM analysis are idealized and, consequently, they differed from the actual experimental system. In the FEM analysis, the model assumed fully dense filaments without flaws and ideal bonding between the filaments in adjacent layers so that the simulations could focus on the effects of the structure on the flexural mechanical response. In practice, glasses and other brittle materials commonly contain flaws such as pores and microcracks which have a major effect on their mechanical response (particularly in flexural or tensile loading). Another factor is the strain rate (or crosshead speed) used in the four-point bending test. The FEM simulations assumed a more or less static condition (the load increased from 0 to the defined value in 1 s, the default time period for a static general step in the ABAQUS software). In comparison, the experimental four-point bending test is more dynamic. The load is applied to the specimen at a constant speed according to ASTM guidelines (0.2 mm min^{-1} in the present study). During the slow movement of the crosshead, microcracks and other flaws have enough time to grow. As the glass filaments were assumed to be free from flaws in the model, the simulation of a dynamic system was not necessary in the present study. The

simulation of a dynamic system would also require a considerable increase in computing power and time.

4.2 Measured flexural strength of scaffolds and validation of FEM simulations

The structures analyzed in the FEM analysis were generally well replicated by the microstructures of the scaffolds fabricated by robocasting (Fig. 6). The scaffolds had a well-controlled microstructure but there was some sagging of the short filaments in the middle layers of a few scaffolds that contained the smallest number of long filaments (Fig. 6b). The long filaments appeared to be too widely spaced to provide sufficient support for the short filaments during the robocasting process. The glass filaments were almost fully dense, as assumed in the models, but a few small pores were apparent in the cross section of the filaments. SEM examination did not show large flaws in the glass filaments, such as large pores and crack-like voids that could serve as strength-limiting flaws.

The measured flexural strength of the ten scaffolds composed of orthogonal long and short filaments in the x and y directions validated the trends predicted by the FEM analysis. Using the uniform grid-like (L1S1) microstructure as a reference, redistributing some of the long rods from middle layers to the top and bottom layers resulted in an increase in the flexural strength. In comparison, redistributing some of the short rods from the middle layers to the top and bottom layers resulted in a decrease in flexural strength (Fig. 7, 9). Scaffolds created with the gradient L3S1 and L4S1 microstructures, composed of a larger number of long filaments in the top and bottom layers, showed flexural strengths that were ~50% and ~130% higher, respectively, than scaffolds with the L1S1 microstructure.

The measured flexural strength of the S45° scaffolds deviated from the trend for the LiSi scaffolds. While the FEM simulations predicted a considerably higher tensile stress in the S45° model (when compared to the L1S1 model), the measured flexural strength was not different from the L1S1 scaffolds. Unlike the LiSi microstructures that were composed of long filaments (~23 mm) and short filaments (~4.7 mm), the S45° microstructure was composed of filaments of length ≤ 6.6 mm in all the layers. Presumably, the probability of a strength-limiting flaw due to processing and environmental factors was lower in the shorter filaments of the S45° microstructure than

in the long filaments of the LiSi microstructures. Although a higher tensile stress was predicted by the FEM simulations, a lower probability of a strength-limiting flaw being present in the filaments of the S45° microstructure could lead to a measured flexural strength that was similar to the L1S1 microstructure. However, comparing the L3S1 or L4S1 microstructure to the S45° microstructure, the structural difference still dominated over possible effects due to flaws, resulting in a significant increase in flexural strength which matched the trend predicted by the FEM analysis.

Our previous studies showed that silicate 13-93 bioactive glass scaffolds with the uniform grid-like (L1S1) microstructure can support bone infiltration and integration with host bone in vivo [21,22]. Consequently, the gradient L4S1 microstructure was designed to have a more porous inner region similar to the L1S1 microstructure to support bone infiltration whereas the top and bottom regions were composed of lower porosity regions to enhance the flexural strength. The gradient L4S1 microstructure mimics human long bones that typically consist of an inner region of trabecular bone (porosity = 50–90%) and an outer region of cortical bone (porosity = 5–10%).

The Weibull modulus, determined from the strength data for a large number of identical samples (typically 20–30 or more) is commonly used as a measure of the mechanical reliability or the probability of failure of brittle materials [24]. A higher Weibull modulus is indicative of lower variability in strength, which means that any microstructural flaws present in the material are more uniform in size and more uniformly distributed in the material. The Weibull modulus determined in the present study from the flexural strength of 30 specimens, $m = 9$ and $m = 8$, respectively, for the L3S1 and L4S1 microstructures, were higher than the value ($m = 6$) obtained previously for the scaffolds with the uniform grid-like L1S1 microstructure [13]. The higher Weibull modulus found in the present study indicates a narrower distribution of flaw sizes in the glass filaments and therefore a more reliable scaffold. Data for the Weibull modulus of biomaterials tested in bending are limited. In one study, isotropic glass-ceramic scaffolds (porosity = 50–75%) prepared from a CaO–Al₂O₃–P₂O₅ glass were found to have a Weibull modulus in the range 3–8 in four-point bending tests [25].

SEM images of fractured surfaces of the scaffolds with the L3S1 and L4S1 microstructures after testing in four-point bending showed features such as hackle regions,

mist regions, smooth mirror regions, and arrest lines which are commonly found on the fractured surface of brittle materials. These features provided useful information for determining the direction of crack propagation. The SEM images confirmed that failure of the scaffolds in four-point bending occurred in the direction from the bottom (subjected to a tensile stress) to the top (subjected to a compressive stress). While the failure origin of each glass filament could be located, the exact glass filament at which failure was initiated could not be determined from the SEM images.

4.3 Compressive strength and capacity to support bone infiltration

The FEM simulations showed that redistribution of the filaments in the z direction from the interior of the uniform grid-like structure (L1S1) to the surface layer (to form the L3S1 structure) did not lead to a higher tensile stress in the filaments whereas increasing the number of the filaments in the z direction (L4S1 structure) produced a reduction in the tensile stress. In general, the measured compressive strength of the scaffolds validated the predictions of the FEM simulations. The scaffolds with the L3S1 microstructure showed an average compressive strength that was approximately equal to that for the L1S1 microstructure whereas the average compressive strength of the L4S1 group was ~22% higher. This trend is compatible with the color scheme and stress scale of the FEM predictions in Fig. 12. In combination, the FEM simulations and experimental data in flexure and compression showed that a redistribution of the glass filaments in the uniform grid-like structure to form structures with a porosity gradient resulted in a significant improvement in the flexural strength without a reduction in the high compressive strength. The FEM simulations provided an efficient approach to determine the manner in which the filaments should be redistributed.

As the scaffolds in the present study are intended for eventual application in structural bone repair, the capacity of the scaffolds to support bone infiltration and integration in vivo is an important factor. Modification of the uniform grid-like (L1S1) microstructure to form microstructures with a porosity gradient (L3S1 and L4S1) did not affect the infiltration of bone into the pore space of the scaffolds and the capacity of the scaffolds to integrate with bone. The percentage of new bone that infiltrated the scaffolds at 12 weeks, as a percentage of the pore area (volume) of the scaffolds, was independent

of the scaffold microstructure (Fig. 15). When evaluated as a percentage of the total defect area, the average amount of new bone that infiltrated the scaffolds with the L4S1 microstructure ($9 \pm 5\%$) was lower than the scaffolds with the L1S1 and L3S1 microstructures ($15 \pm 3\%$ and $19 \pm 5\%$) but the difference was not significant. One factor that might have contributed to the lower amount of new bone in the L4S1 group was their lower porosity (33% vs. 43% for the L1S1 and L3S1 groups), providing less pore space for bone infiltration.

Scaffolds of bioactive 13-93 glass with a uniform grid-like (L1S1) microstructure have shown the capacity to repair critical size segmental defects in rat femurs [16]. With their higher flexural strength, coupled with their comparable or higher compressive strength and their comparable ability to support bone infiltration, scaffolds with a gradient porosity (L3S1 and L4S1 structures) created in this study could provide more reliable implants for structural bone repair.

5. Conclusions

Finite element modeling (FEM) was used to simulate the flexural mechanical response of a variety of porous beam-shaped models composed of ideal glass filaments bonded orthogonally in adjacent layers to form a grid-like microstructure. The FEM simulations showed that when compared to a uniform grid-like model, redistribution of the long filaments from the middle layers to the bottom and top layers resulted in a decrease in the tensile stress in the bottom layers. In comparison, redistribution of the short filaments from the middle layers to the bottom and top layers enhanced the tensile stress of the bottom layers. The measured flexural strength of scaffolds fabricated with microstructures similar to those in the models validated the predictions of the FEM simulations. Scaffolds with a porosity gradient, composed of a higher porosity inner region and a lower porosity outer region to better mimic human long bones, showed a flexural strength that was more than twice the value of the uniform grid-like microstructure, coupled with a higher average compressive strength and a comparable capacity to support bone infiltration in vivo. These scaffolds could provide more reliable implants for structural bone repair.

References

1. R. Cancedda, P. Giannoni, M. Mastrogiacomo, *Biomaterials* 28 (2007) 4240–4250.
2. P.V. Giannoudis, H. Dinopoulos, E. Tsiridis, *Injury* 36 (2005) S20–27.
3. C. Laurencin, Y. Khan, S.F. El-Amin, *Expert Rev. Med. Devices* 3 (2006) 49–57.
4. L.L. Hench, *J. Mater. Sci. Mater. Med.* 17 (2006) 967–978.
5. L.-C. Gerhardt, A.R. Boccaccini, *Materials* 3 (2010) 3867–3910.
6. M.N. Rahaman, D.E. Day, B.S. Bal, Q. Fu, S.B. Jung, L.F. Bonewald, et al., *Acta Biomater.* 7 (2011) 2355–2373.
7. Q. Fu, E. Saiz, M.N. Rahaman, A.P. Tomsia, *Mater. Sci. Eng. C* 31 (2011) 1245–1256.
8. J.R. Jones, *Acta Biomater.* 9 (2013) 4457–4486.
9. S.M. Giannitelli, D. Accoto, M. Trombetta, A. Rainer, *Acta Biomater.* 10 (2014) 580–594.
10. N.D. Doiphode, T.S. Huang, M.C. Leu, M.N. Rahaman, D.E. Day, *J. Mater. Sci. Mater. Med.* 22 (2011) 515–523.
11. T.S. Huang, N.D. Doiphode, M.N. Rahaman, M.C. Leu, B.S. Bal, D.E. Day, *Mater. Sci. Eng. C* 32 (2011) 1482–1489.
12. A. Deliomani, M.N. Rahaman, *J. Eur. Ceram. Soc.* 32 (2012) 3637–3646.
13. X. Liu, M.N. Rahaman, G.E. Hilmas, B.S. Bal, *Acta Biomater.* 9 (2013) 7025–7034.
14. Q. Fu, E. Saiz, A.P. Tomsia, *Adv. Funct. Mater.* 21 (2011) 1058–1063.
15. Q. Fu, E. Saiz, A.P. Tomsia, *Acta Biomater.* 7 (2011) 3547–3554.
16. L. Bi, B. Zobell, X. Liu, M.N. Rahaman, L.F. Bonewald, *Mater. Sci. Eng. C* 42 (2014) 816–824.
17. P. Miranda, A. Pajares, F. Guiberteau, *Acta Biomater.* 4 (2008) 1715–1724.
18. C. Sandino, D. Lacroix, *Biomech. Model. Mechanobiol.* 10 (2011) 565–576.
19. D. Lacroix, J.A. Planell, P.J. Prendergast, *Philos. Trans. A Math. Phys. Eng. Sci.* 367 (2009) 1993–2009.
20. A. Boccaccio, A. Ballini, C. Pappalettere, D. Tullo, S. Cantore, A. Desiate, *Int. J. Biol. Sci.* 7 (2011) 112–132.
21. X. Liu, M.N. Rahaman, Y. Liu, B.S. Bal, L.F. Bonewald, *Acta Biomater.* 9 (2013) 7506–7517.
22. Y. Lin, W. Xiao, X. Liu, B.S. Bal, L.F. Bonewald, M.N. Rahaman, *J. Non-Cryst. Solids* 432 (2016) 120–129.

23. A.M. Korsunsky, In: Encyclopedia of Materials: Science and Technology. Oxford (UK), Pergamon, 2001; p. 2398–2404.
24. J.B. Wachtman, W.R. Cannon, M.J. Matthewson, Mechanical Properties of Ceramics. 2nd ed., New York: Wiley, 2009.
25. F. Pernot, P. Etienne, F. Boschet, L. Datas, J. Am. Ceram. Soc. 82 (1999) 641–648.

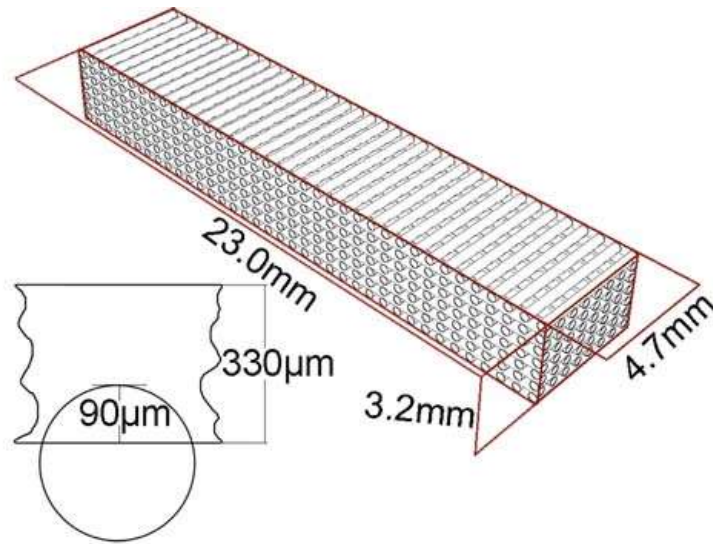


Fig. 1. The external shape and dimensions of the models used in FEM simulations of the flexural mechanical response. Each filament had a diameter of $330\ \mu\text{m}$ and the thickness of the partially overlapped region between the filaments in adjacent layers was $90\ \mu\text{m}$.

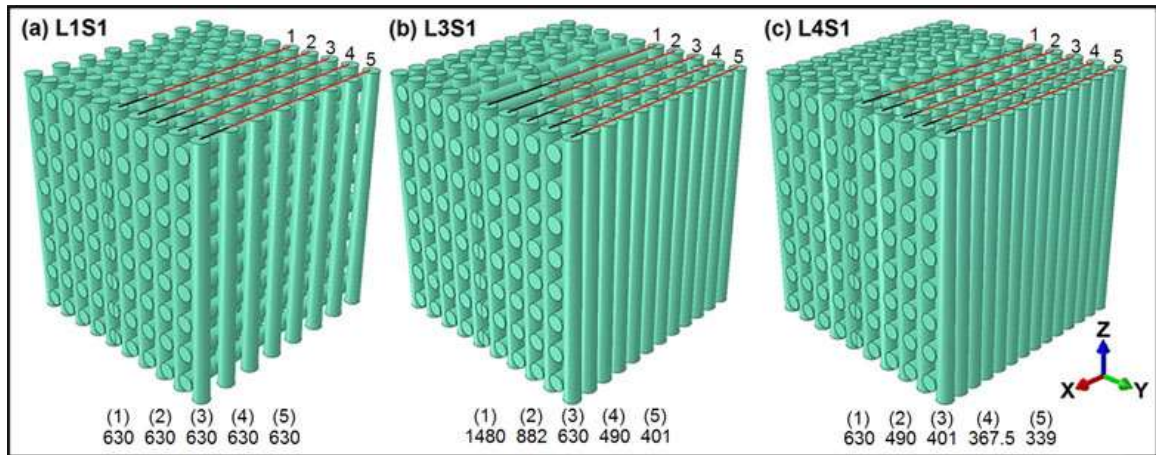


Fig. 2. The external shape and structure of the models used in FEM simulations of the mechanical response in compression. The properties of the filaments were identical to those used for the simulations in flexure. The center-to-center distance (in μm) between adjacent filaments in each layer of one-half of each structure is shown below each model.

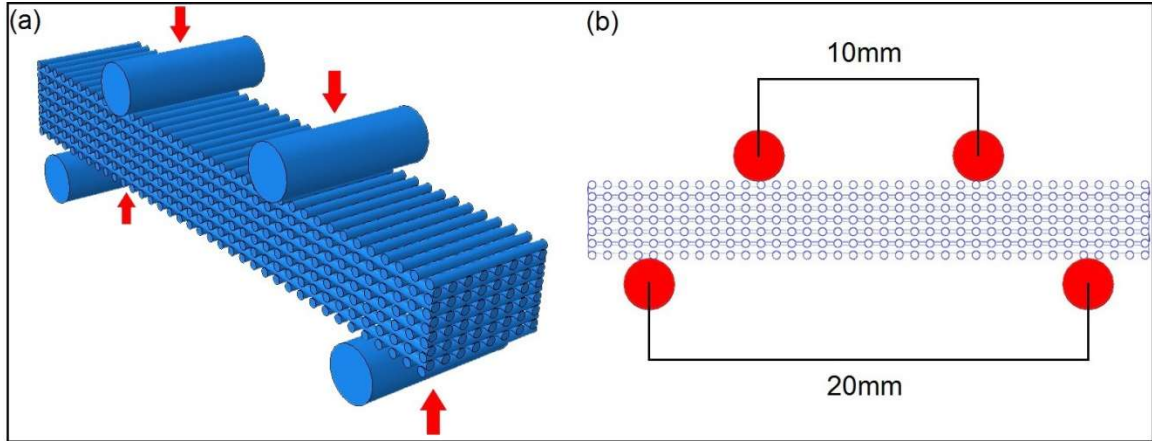


Fig. 3. (a) Three-dimensional and (b) planar view of the four-point loading system used in the FEM simulations. The inner and outer spans were 10 mm and 20 mm, respectively, and the load was applied in a vertical direction (red arrow).

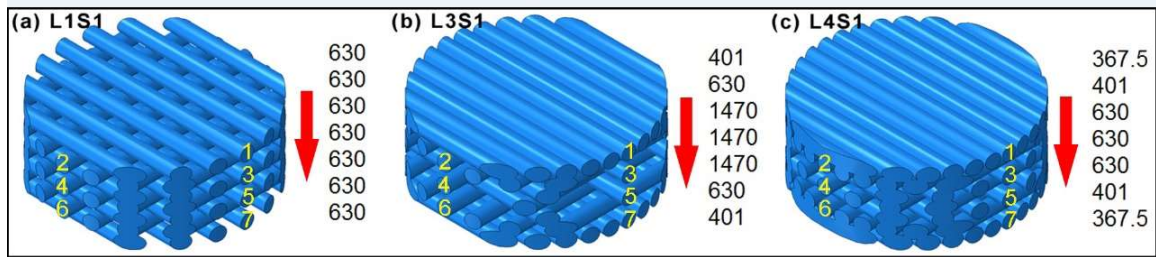


Fig. 4. Shape and microstructure of scaffolds used for implantation in rat calvarial defects in vivo. The scaffolds, corresponding to the L1S1, L3S1 and L4S1 models in the FEM simulations, were 4.6 mm in diameter and 1.5 mm thick and were composed of 7 orthogonal layers of glass filaments. The center-to-center distance (in μm) between adjacent filaments in each layer of the scaffolds is shown on the right.

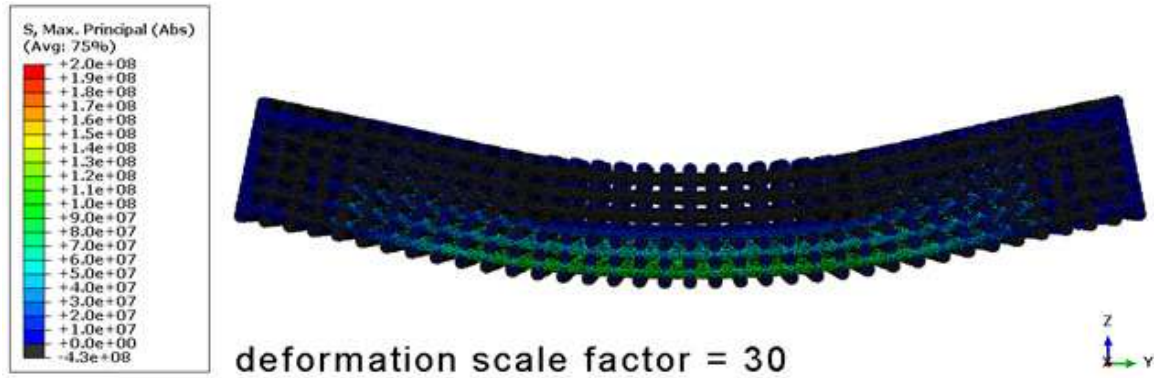


Fig. 5. Typical deformation of the uniform grid-like (L1S1) model in flexure showing the magnitude and distribution of the stress in the filaments as determined by FEM simulations. The actual deformation of the model has been magnified by a scale factor of 30. The scale on the left gives the maximum principal stress corresponding to specific colors.

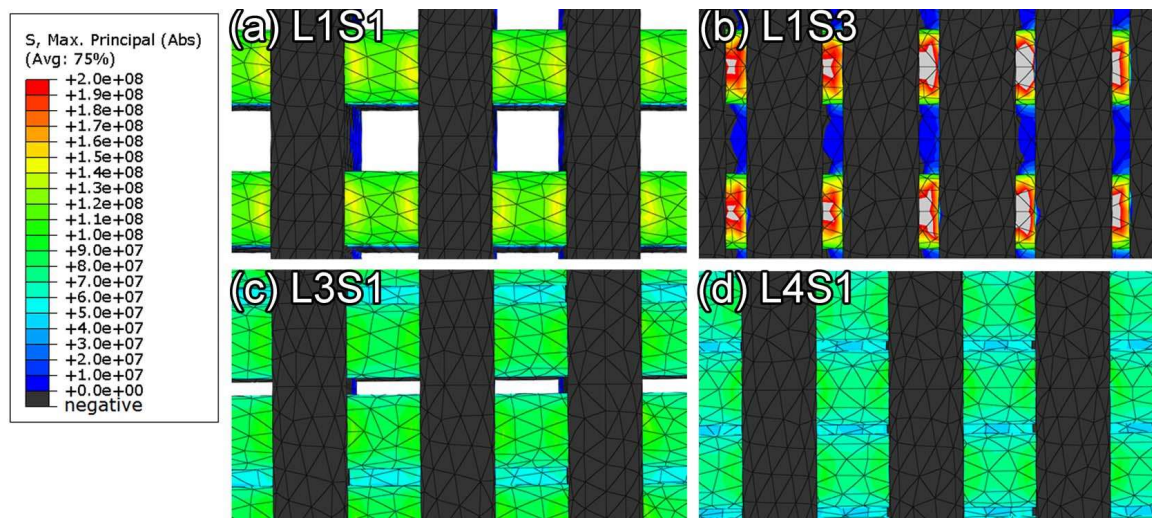


Fig. 6. The magnitude and distribution of the tensile stress in the long filaments of the bottom layers of different models when subjected to the same applied load in four-point bending. The scale on the left gives the maximum principal stress corresponding to specific colors.

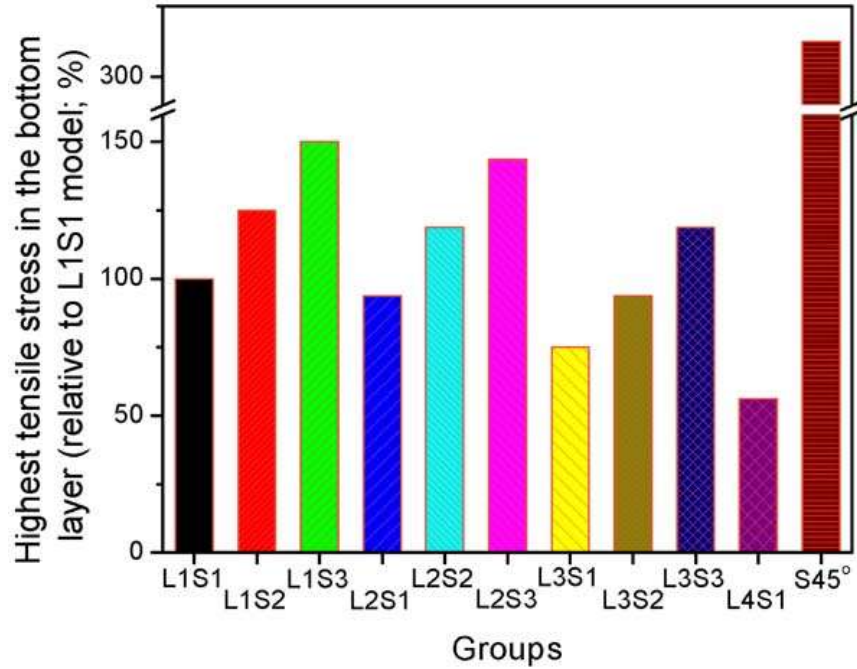


Fig. 7. Highest tensile stress in the long filaments in the bottom layer of the models (normalized to the L1S1 model) determined from FEM simulations of four-point bending under an applied load of 100 N. The region of highest stress corresponded to the middle region of the bottom filaments between the inner span.

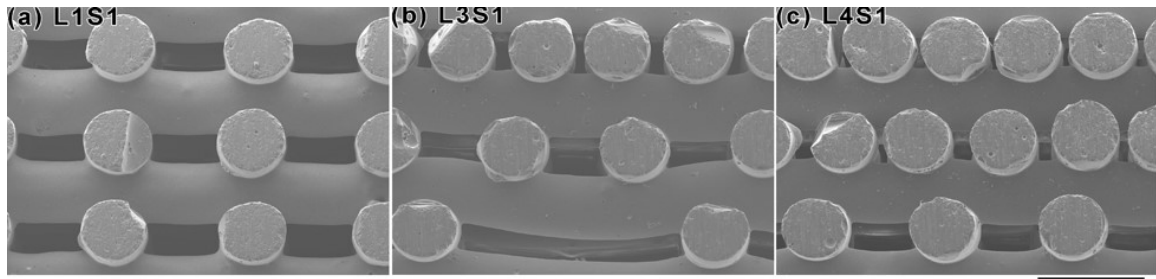


Fig. 8. SEM images of the cross section perpendicular to the long filaments of as-fabricated 13-93 bioactive glass scaffolds with three different microstructures. Scale bar = 500 μm .

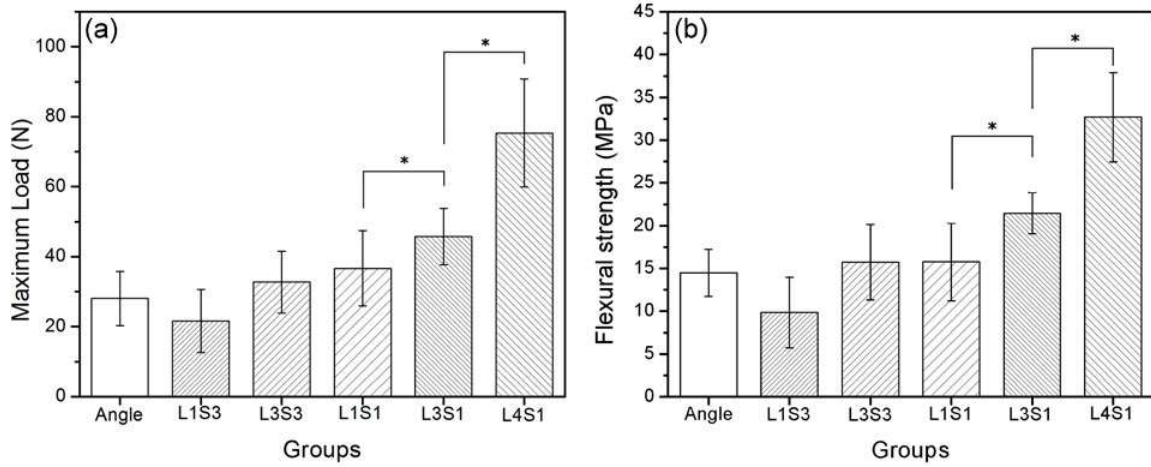


Fig. 9. (a) Measured load at failure and (b) flexural strength of as-fabricated 13-93 bioactive glass scaffolds with the microstructures shown, tested in four-point bending.

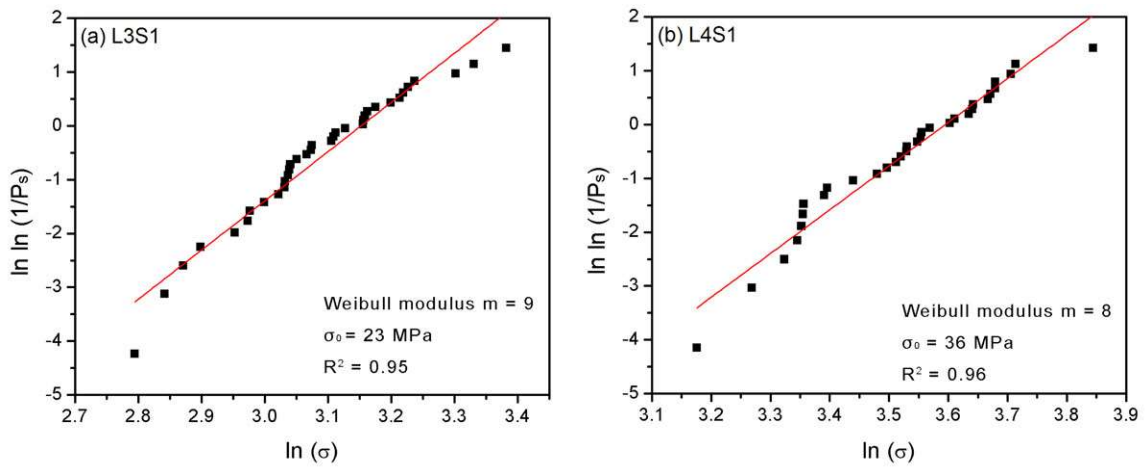


Fig. 10. Weibull plots of the flexural strength data for 13-93 bioactive glass scaffolds with the L3S1 architecture (a) and L4S1 architecture (b). The straight line shows a least-squares fit to the data.

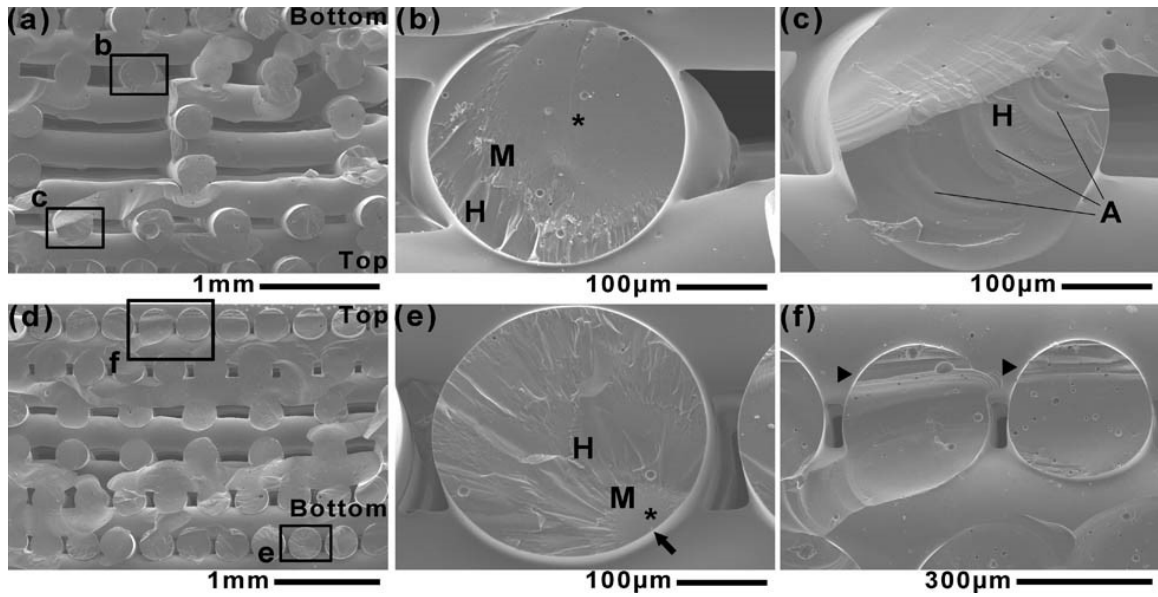


Fig. 11. SEM images of the fractured surfaces of the scaffolds with the L3S1 architecture (a-c) and L4S1 architecture (d-f) after testing in four-point bending. The plane (a, d) is approximately perpendicular to the direction of the long filaments. Higher magnification images of selected areas in (a), (d) are shown in (b, c) and (e, f). (Top: the side contacting inner span during the bending test; Bottom: the side contacting outer span; Stars: mirror region; M: mist region; H: hackle region; A: arrest line; arrow: crack origin; arrowheads: cantilever curls.)

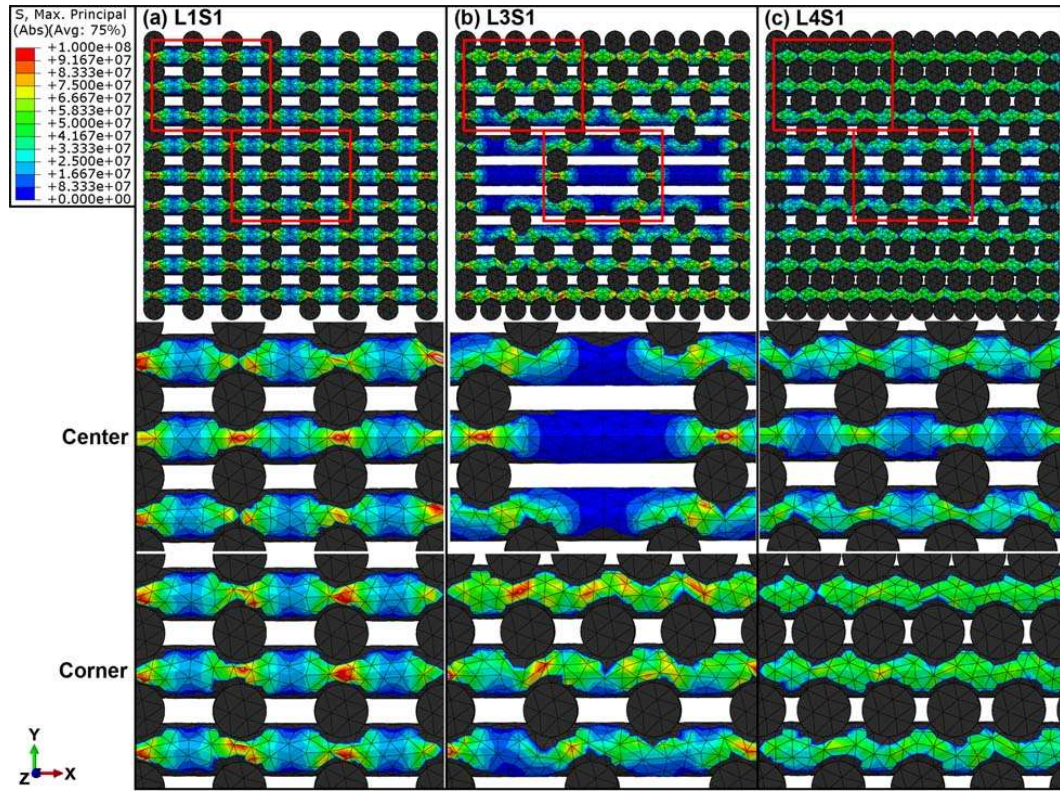


Fig. 12. Magnitude and distribution of the tensile stress in the filaments (parallel to xy plane) of different models when subjected to the same applied load in compression. The scale on the left gives the maximum principal stress corresponding to specific colors.

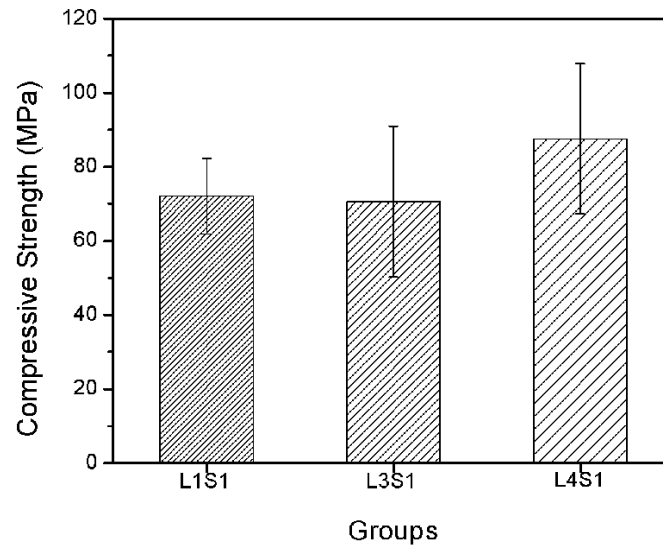


Fig. 13. Measured compressive strength of as-fabricated 13-93 bioactive glass scaffolds with the microstructures corresponding to L1S1, L3S1 and L4S1.

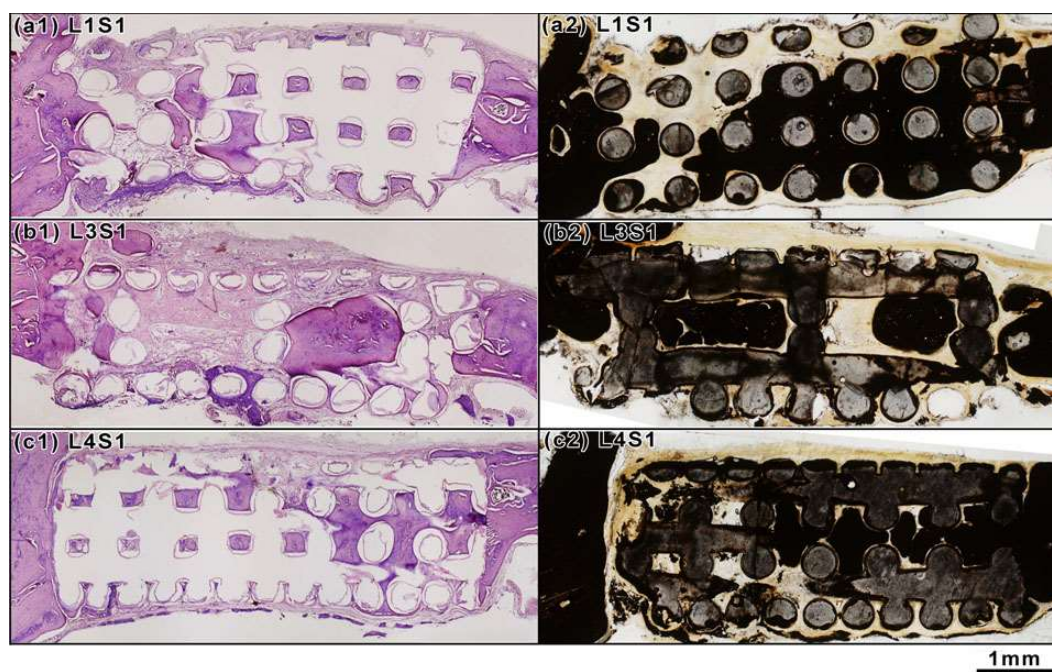


Fig. 14. Transmitted light images of H&E-stained sections (a1,b1,c1) and von Kossa-stained sections (a2,b2,c2) of rat calvarial defects implanted for 12 weeks with the three groups of bioactive glass scaffolds with microstructures corresponding to L1S1, L3S1 and L4S1.

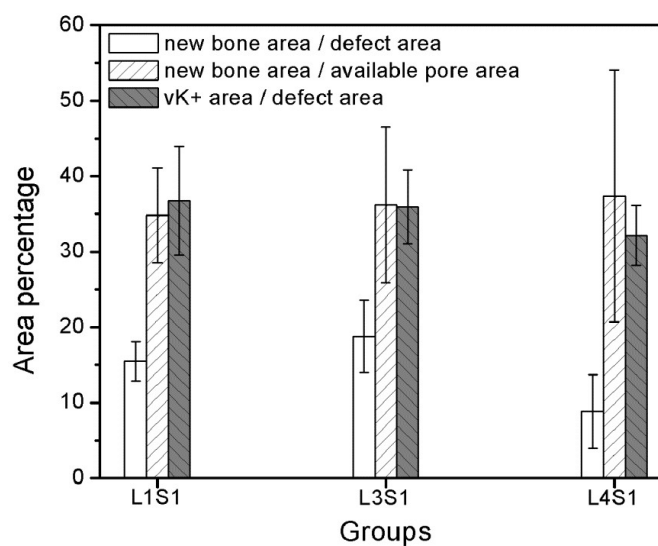


Fig. 15. Amount of new bone area determined as a percentage of the total defect area and the available pore area, and the total von Kossa positive area determined as a percentage of the total defect area, for rat calvarial defects implanted for 12 weeks with the three groups of scaffolds with microstructures corresponding to L1S1, L3S1 and L4S1.

Table I. Summary of models analyzed in FEM simulations of the mechanical response in flexure. The models, with the shape of beams, were composed of alternating layers of long glass filaments (L) and short glass filaments (S) arranged orthogonally along the x and y axes. The designations LiSi are used to describe the different distribution of the filaments in the models. Each model was composed of 6 layers of long filaments and 7 layers of short filaments. All the models were composed of the same number of long filaments (48) and short filaments (259), except for the L4S1 model (66 long filaments and 259 short filaments). The cross section of the long filaments in the models is also shown. In addition, a model (S45°) with same porosity as L1S1, but with filaments at 45° to the x and y axes was also analyzed. The S45° model was composed of layers with different porosity as shown.

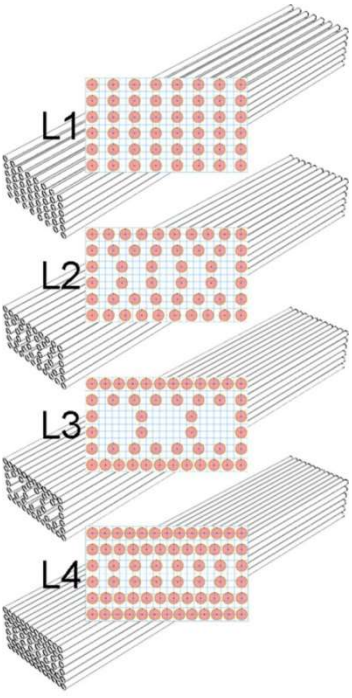
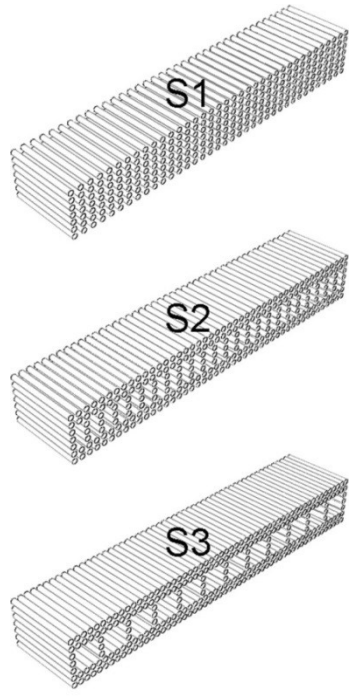
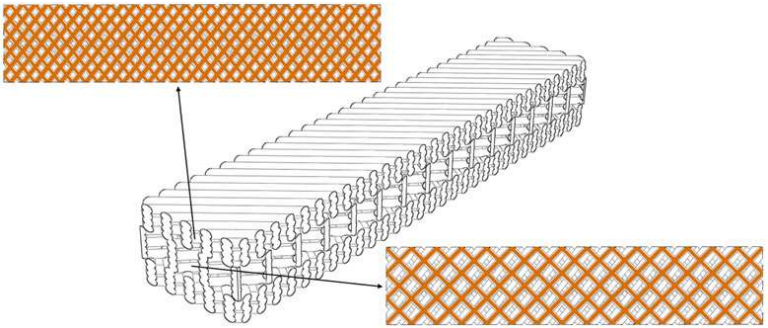
Long filaments	Short filaments	Model designation
		L1S1
		L1S2
		L1S3
		L2S1
		L2S2
		L2S3
		L3S1
		L3S2
		L3S3
		L4S1
		S45°

Table II. Geometrical parameters of the LiSi models (Table 1) analyzed in FEM simulations of the mechanical response in flexure. The center-to-center distance (μm) between adjacent glass filaments in the each layer of the models is shown. In the S45° model, the center-to-center distance was 581 μm and 1054 μm , respectively, for the denser layers and more porous layers.

Long filaments					Short filaments			
Layer	L1	L2	L3	L4	Layer	S1	S2	S3
1	630	490	401	367.5	1	630	504	420
2	630	630	630	401	2	630	504	420
3	630	882	1470	630	3	630	945	1890
4	630	882	1470	630	4	630	945	1890
5	630	630	630	401	5	630	945	1890
6	630	490	401	367.5	6	630	504	420
					7	630	504	420

IV. Tough and strong porous bioactive glass–PLA composites for structural bone repair

Wei Xiao ^a, Guangda Li ^{a, b}, Mohsen Asle Zaeem ^a, B. Sonny Bal ^c, Mohamed N. Rahaman ^a

^a Department of Materials Science and Engineering, Missouri University of Science and Engineering, Rolla, Missouri 65409, USA

^b Department of Medical Technology and Engineering, Henan University of Science and Technology, Luoyang, China, 471023

^c Department of Orthopaedic Surgery, University of Missouri, Columbia, Missouri 65212, USA

ABSTRACT

Bioactive glass scaffolds have been used to heal small contained bone defects but their application to repairing structural bone is limited by concerns about their mechanical reliability. In the present study, the addition of an adherent polymer layer to the external surface of strong porous bioactive glass (13-93) scaffolds was investigated to improve their toughness. Finite element modeling (FEM) of the flexural mechanical response of beams composed of a porous glass and an adherent polymer layer predicted a reduction in the tensile stress in the glass with increasing thickness and elastic modulus of the polymer layer. Mechanical testing of composites with structures similar to the models, formed from 13-93 glass and polylactic acid (PLA), showed trends predicted by the FEM simulations but the observed effects were considerably more dramatic. A PLA layer of thickness equal ~12.5% of the scaffold thickness increased the load-bearing capacity of the scaffold by ~50%. The work of fracture increased dramatically, resulting in a change in mechanical response from brittle to “ductile”. These bioactive glass–PLA composites, combining bioactivity, high strength, high work of fracture and an internal architecture shown to be conducive to bone infiltration, could provide optimal implants for healing structural bone defects.

1. Introduction

Bone defects are a common occurrence in orthopedic surgery, resulting from trauma, malignancy, infection and congenital disease. Clinically, these defects are reconstructed through the use of various bone grafts. Whereas small contained bone defects are repairable with a wide variety of commercially-available osteoconductive and osteoinductive filler materials [1, 2], the repair of large (critical size) defects in structural bone is challenging. The available treatments such as bone allografts, autografts and porous metals are limited by costs, availability, durability, infection risk, donor site morbidity and uncertain healing. Consequently, there is a clinical need for synthetic biocompatible materials that can replicate the strength, bioactivity, morphology, porosity and load-bearing ability of living bone.

Bioactive glasses have been studied and developed as one such material because they are biocompatible, osteoconductive, convert to hydroxyapatite *in vivo*, heal readily to host bone and soft tissues and they are amenable to fabrication into porous three-dimensional architectures [3–7]. However, most bioactive glass scaffolds created by conventional methods have shown low strength, typically compressive strength in a range comparable to human trabecular bone (2–12 MPa) [5]. This low strength and a brittle mechanical response typical of glass have limited the application of bioactive glass scaffolds to the healing of contained or non-loaded bone defects.

Recent studies using additive manufacturing (rapid prototyping or three-dimensional printing) methods have shown the ability to create bioactive glass scaffolds with a porous grid-like microstructure which have vastly improved compressive strength, comparable to the strength of human cortical bone (~100–150 MPa) [8–11]. Despite a low flexural strength (~10–15 MPa), much smaller than that of cortical bone (~100–150 MPa) [9], these strong porous scaffolds have shown the ability to repair critical size segmental defects in a rat or rabbit femoral model [12, 13]. Modification of the grid-like microstructure to produce a porosity gradient in the scaffolds produced a significant improvement in the flexural strength (~35 MPa) without sacrificing their ability to support bone infiltration [14]. As bending is an important loading in structural bone, this improvement in flexural strength should improve the mechanical reliability of bioactive

glass scaffolds in vivo. However, these scaffolds with high compressive and flexural strength still showed a brittle mechanical response.

Several studies have shown the ability to modify or improve the mechanical response of porous ceramics or glass by infiltrating the pore volume or coating the pore surface with a polymer such as a biodegradable polymer composed of polycaprolactone (PCL) or polylactic acid (PLA) [15–21]. The polymer phase presumably acts as a sealant to bond together the walls of pre-existing flaws in the surface of the brittle material and limit the initiation or growth of cracks, providing a defect healing mechanism [15–17]. Polymers with high elastic modulus, such as PLA, can also assist in partially supporting the applied load, thereby reducing the effective load on the ceramic or glass phase [15–17].

While complete infiltration of the pore space of biocompatible ceramics or glass scaffolds with a biodegradable polymer can improve their mechanical response, the absence of porosity could, at least initially, limit bone infiltration and integration of the scaffolds in vivo. An alternative approach, particularly bioactive materials, is judicious coating of the pore surface of the scaffolds to provide an optimal combination of improved mechanical response, bioactivity and porosity conducive to bone or tissue infiltration. Coating the pore surface of weak bioactive glass (45S5) scaffolds with poly(D, L-lactic acid) has been found to produce a small improvement in their compressive and flexural strength but remarkable improvement in their work of fracture [20]. When encapsulated in a sheath of PLA (~500 μm), the average flexural strength of bioactive glass (13-93) scaffolds (external diameter 4.2 mm; porosity~20%) formed from thermally-bonded fibers (300–700 μm) increased by approximately 2.5 times, from ~50 MPa to ~120 MPa [21]. Furthermore, the PLA sheath produced a drastic modification of the brittle mechanical response of the glass scaffolds, resulting in a considerable improvement in the work of fracture and a “ductile” response.

Based on our previous studies which showed the ability to create strong porous bioactive glass (13-93) scaffolds with a grid-like microstructure conducive to supporting bone infiltration [14], the present study was undertaken to modify their brittle mechanical response and improve their toughness. Finite element modeling (FEM) was used to simulate the mechanical response in flexural loading of model composites composed of a

porous glass beam with a grid-like structure and adherent surface layers composed of an elastic polymer. Then composites with microstructures mimicking the model structures were created from 13-93 bioactive glass and PLA, and tested in four-point bending to evaluate their mechanical response.

2. Materials and methods

2.1 Design of composite structures

Three different glass structures, with the external geometry of a beam (23.0 mm long \times 4.7 mm wide \times 3.2 mm thick) and composed of orthogonal glass filaments (diameter = 330 μ m) in adjacent layers, were analyzed in FEM simulations (Fig. 1). The structures were composed of 6 layers of filaments in the long direction of the beam and 7 layers of filaments in the orthogonal direction. These structures were selected on the basis of a previous study [14]. The structure designated L1S1 was composed of a uniform grid-like arrangement of the filaments in the adjacent layers. In comparison, the structure designated L3S1 was derived from the L1S1 structure by redistributing some of the long (L) filaments in the structure from the interior to the top layer and bottom layer but keeping the number of filaments the same. The L4S1 structure was obtained from the L3S1 structure by adding additional long filaments to the second layer from the top and bottom, making these layers identical to the top and bottom layer. All three structures had the same arrangement of the short (S) filaments. The redistribution of the long filaments resulted in a porosity gradient in the L3S1 and L4S1 structures, with the top and bottom layers of the structure having a lower porosity than the interior. FEM simulations and four-point bending experiments previously showed that the flexural strength of scaffolds with the L3S1 and L4S1 structures (22 ± 3 MPa and 34 ± 5 MPa, respectively) was significantly greater than the L1S1 scaffold (15 ± 5 MPa) [14].

Composite structures were designed by adding adherent layers of polymer to the top and bottom surfaces of the beams (Fig. 2). Layers of thickness 200, 400 and 800 μ m were used. Based on observations from experiments described later, a small amount of polymer infiltration into the surface layer of the glass structure was assumed. Twelve different structures were analyzed in the FEM simulations, based on the structure of the glass scaffold and the thickness of the polymer layer (Table I).

2.2 Finite element simulations

Finite element simulations were carried out using ABAQUS/CAE 6.14-1 software (Dassault Sytemes Simulia Corp., Providence, RI). Twelve models shown in Table I were analyzed in four-point bending. The filaments in all the models were assumed to be composed of a dense homogeneous material with a Young's modulus of 70 GPa and a Poisson's ratio of 0.25, values which are comparable to those of a silicate glass [22]. The polymer layer in the models were assumed to be dense and homogeneous with a Young's modulus of 0.65 GPa (measured for the PLA sheets used in this study) and a Poisson's ratio of 0.36 (given in the manufacturer's specifications for PLA). The polymer layer was assumed to have an elastic response and to be perfectly bonded to the glass surface, without any delamination under flexural loading.

For the simulations in flexural loading, 4 rigid cylinders with a diameter of 2.0 mm were generated to simulate the fixture used in the four-point bending test, as described previously [14]. The two upper cylinders, each 5 mm from the midline, served as the inner span, while the two lower cylinders, 10 mm from the midline, served as the outer span. The cylinders were in contact with the model composites from the beginning of the simulations, and the contact was assumed to be hard (no interpenetration between the materials) and frictionless.

The FEM models were partitioned into several parts in order to improve the meshing and apply the proper boundary conditions. The FEM models were discretized with an approximate mesh size of 120 μm and quadratic tetrahedral elements were used. This size was selected based on a previous study [14] as it provided a good balance between computing time and convergence to reliable results. The middle of the cross section perpendicular to x axis was fixed at the x axis direction ($U1 = 0$) to prevent the scaffold from sliding in the x axis direction. In addition, the middle of the cross section perpendicular to y axis was fixed at the y axis direction ($U2 = 0$) to prevent sliding in the y axis direction during bending. The two lower cylinders of the fixture were fixed in all directions ($U1 = U2 = U3 = 0$) and an evenly distributed load of 100 N was applied to the two upper cylinders.

A desktop computer with 16 CPU cores and 128 GB of RAM were used for the simulations. A typical CPU time to complete a simulation was $\sim 4\text{h}$. As a brittle material,

glass can withstand much higher stresses in compression than in tension. Consequently, the highest tensile stress within the inner span of the model was used as the primary parameter in the load carrying capacity analysis.

2.3 Creation of bioactive glass–PLA composites

Bioactive glass (13-93) scaffolds with the geometry of a beam and microstructure corresponding to the L1S1, L3S1 and L4S1 structure in the FEM simulations were fabricated using a robotic deposition technique as described in detail elsewhere [14]. Briefly, as-received 13–93 glass frit (Mo-Sci Corp., Rolla, MO) was ground to form particles ($\sim 1\ \mu\text{m}$), mixed with a 20 wt. % Pluronic-127 binder solution to form a paste (40 vol. % glass particles) and extruded using a robocasting machine (RoboCAD 3.0; 3-D Inks, Stillwater, OK). After drying at room temperature, the scaffolds were heated in O_2 at a rate of $0.5\ ^\circ\text{C min}^{-1}$ to $600\ ^\circ\text{C}$ to burn out the processing additives and sintered for 1 h at $700\ ^\circ\text{C}$ (heating rate = $5\ ^\circ\text{C min}^{-1}$) to densify the glass filaments. The external dimensions of the as-fabricated bioactive glass beams were 23.0 mm long \times 4.7 mm wide \times 3.2 mm thick.

PLA sheets were prepared by dissolving as-received pellets (molecular weight = 150 kDa; IngeoTM biopolymer 4043D; NatureWorks LLC, Minnetonka, MN) in CHCl_3 , casting the solution on a flat surface and evaporating the solvent slowly. Sheets of thickness ~ 200 , 400 and 800 μm were formed from solutions with different PLA concentration. The amorphous or crystalline nature of the PLA sheets was checked using X-ray diffraction XRD (D/mas 2550 v; Rigaku; The Woodlands, TX, USA). Dog-bone shaped specimens were cut from the sheets (800 μm thick) using a standard fixture and tested in tension at deformation rates of $2\text{--}10\ \text{mm min}^{-1}$ to measure their Young's modulus.

A controlled and reproducible procedure was used to bond a PLA layer to the top and bottom surface of the bioactive glass beams. One surface of a sheet was wetted with CHCl_3 and applied to one surface of the scaffold (in the x - y plane). Then a pressure of $\sim 20\ \text{kPa}$ was applied to keep the sheet in contact with the scaffold surface and the system was allowed to dry for 24 hours. The same process was repeated to bond a PLA layer to

the opposite surface of the bioactive glass scaffold. Excess PLA was trimmed off the edges of the scaffold.

2.4 Measurement of bioactive glass–PLA adhesive strength

The adhesive strength between the PLA layer and the surface of the bioactive glass scaffold was measured using an adhesion testing apparatus (Romulus universal test equipment; Quad Group Inc., Spokane, WA). PLA sheets of thickness 800 μm were cut into disks (diameter = 2.6 mm) and bonded to one surface of the bioactive glass scaffold using the same process described earlier for the preparation of the composite scaffolds. Then an aluminum rod (2.6 mm in diameter) was bonded to the PLA disk using an adhesive capable of withstanding a stress >100 MPa. The system was held in the testing apparatus and the aluminum rod was pulled at a rate of ~ 2 mm min^{-1} until delamination of the PLA layer failed. The adhesive strength was determined from the maximum recorded load, the total interfacial area between the scaffold and the PLA disc and the actual area of the PLA disk in contact with the glass scaffold. As the scaffold had a porous grid-like microstructure, the area of the PLA disc in actual contact with the glass was lower than the total interfacial area.

2.5 Mechanical testing in four-point bending

Flexural testing of the scaffolds in four-point bending was performed using a fully articulated fixture (outer span = 20 mm; inner span = 10 mm) at a crosshead speed of 0.2 mm min^{-1} using a 2 kN load cell. The stress was applied in the z direction (the same direction used in the FEM simulations). Eight samples of each group were tested according to the procedure described in ASTM C1674-11 and the load versus deformation curves were recorded. After testing, the samples were examined in a scanning electron microscope, SEM (S-4700; Hitachi, Tokyo, Japan) and by optical microscopy (KH-8700; Hirox-USA, Inc., Hackensack, NJ).

2.6 Statistical analysis

The data are presented as a mean \pm standard deviation (SD). Analysis for differences between groups was performed using one-way analysis of variance (ANOVA) with Tukey's post hoc test. Differences were considered significant for $p < 0.05$.

3. Results

3.1 Finite element simulations

The deformation of a model composite composed of a glass scaffold with the L1S1 structure and an adherent polymer surface layer of thickness 200 μm in four-point bending is shown in Fig. 3. The deformation of the composite beam was magnified 15 times (scale factor = 15) for ease of observation. Similar deformation profiles were found for the other composites that were analyzed. The distribution of the maximum principal stress (S, Max. Principal (Abs.)) in the deformed structure is also shown in color, as represented by the scale in Fig. 3. Negative tensile stress was found in the top layers of the scaffold as they were in compression during the bending. The highest tensile stress was present in the long filaments of the bottom layer in the y-direction. As the polymer layer could deform more easily than the glass filaments due to its much lower Young's modulus, the tension was much lower in the PLA layer. According to the maximum principal stress theory (Tresca), failure will occur when the maximum principal stress in a system reaches the maximum stress at the elastic limit in simple tension. This is approximately valid for brittle materials such as glass. Consequently, particular attention was paid to differences in the magnitude and distribution of the stress in the bottom layers of the glass filaments of the various models.

The magnitude and distribution of the tensile stress in the long filaments at the middle of the bottom layers of the models are shown in Fig. 4. The highest tensile stress was present at the contact region between the long and short filaments. Fig. 5 shows the magnitude of the highest tensile stress for the various models. For models with same polymer layer thickness, the highest tensile stress was in the order $\text{L1S1} > \text{L3S1} > \text{L4S1}$, which is in consistent with the results of previous simulations for the same glass structures without a polymer layer [14]. For models with same glass structure but different polymer layer thickness, the simulations predicted a small decrease in the

magnitude of the tensile stress (or the area with same magnitude of the tensile stress) in the glass filaments with increasing thickness of the PLA coating. For a PLA layer thickness of 800 μm , the highest stress in the filaments decreased by less than 10% when compared to the scaffold without a PLA layer.

The effect of the Young's modulus of the polymer layer was also analyzed. For a model composed of a glass scaffold with the L1S1 structure and a polymer layer of thickness 200 μm , Fig. 6 shows the magnitude and distribution of the tensile stress in the glass filaments near the middle of the bottom layers. The tensile stress decreased with increasing Young's modulus of the polymer layer.

3.2 Mechanical response of as-fabricated bioactive glass-PLA composites

X-ray diffraction patterns of the PLA sheets used in this study showed strong well-defined peaks corresponding to crystalline PLA and broad low-intensity bumps indicative of an amorphous PLA phase (results not shown). The results indicate that the PLA layers in the composites were semi-crystalline and not amorphous (results not shown). The measured stress vs. strain curves and the Young's modulus determined from the initial linear region of the curves at cross-head speeds of 2, 5 and 10 mm/min are shown in Fig. 7. As generally observed for polymeric materials, the Young's modulus increased with increasing strain rate. The PLA sheet showed an elastic response at strains less than ~1–2% for the strain rates used, which was considerably larger than the strain to failure of the bioactive glass (~0.1%).

Optical images of as-fabricated bioactive glass-PLA composites with a PLA layer thickness of ~200, 400 and 800 μm are shown in Fig. 8. The PLA layers appeared to have a uniform thickness and they partially infiltrated the macroporous surface of the glass scaffolds (the space between the short glass filaments at the surface). Higher magnification examination in the SEM revealed the presence of a few isolated pores within PLA layer. These pores existed though the entire thickness of the 200 μm PLA layer which meant that the glass surface immediately below these through-thickness pores was bare. Apparently, the 200 μm PLA layer was not sufficiently thick to provide a complete uniform layer over the entire surface of the glass scaffold. No through-thickness pores were observed in the 400 μm or 800 μm PLA layer. The measured adhesive

strength between the PLA layer and the glass scaffold was 1.0 ± 0.1 MPa based on the total interfacial area. Because of the porous nature of the scaffold surface, the actual contact area between the PLA and the glass was estimated to be approximately two-thirds of the total interfacial area. If the actual contact area was used, the adhesive strength was ~ 1.5 MPa.

After the adhesion test, the surface of the PLA which was previously adherent on the glass scaffold showed a structure composed of bumps and valleys that replicated the macroscopic structure of the glass scaffold surface. This indicated some degree of mechanical interlocking between the PLA and the glass scaffold (Fig. 9a). The glass scaffold showed the presence of residual adherent PLA which but this was situated mainly at the junctions between the two outermost layers of glass filaments (Fig. 9b). The “smooth” surface of the glass filaments previously in contact with the PLA layer showed little residual PLA.

Typical load versus strain curves in four-point bending for composites formed from 13-93 bioactive glass scaffolds with the L1S1 structure and different PLA layer thickness are shown in Fig. 10a. The glass scaffold without a PLA layer showed a typical brittle mechanical response (rapid failure after an elastic response). The applied load showed a peak followed by a rapid decrease as the structure fractured and was unable to support the load. For a PLA layer thickness of 200 μm , the peak load increased by $\sim 50\%$ but a brittle mechanical response was still observed. In comparison, the composites with a PLA layer thickness of 400 or 800 μm showed a dramatic change in mechanical response. First, the peak load increased, showing the ability of the composite to support a higher load than the glass scaffold alone (without a PLA layer). When compared to the glass scaffold alone, the peak load increased by $\sim 95\%$ and $\sim 110\%$, respectively, for composites with PLA layer thicknesses of 400 and 800 μm . Second, the composite did not fail in a brittle manner. Instead, the composite was able to support a considerable load at strains up to as high as 2.5% when the experiments were terminated. The load versus strain curves showed additional peaks and valleys, and the load supported by the composite when the experiments were terminated was even higher than the load at the first peak. The area under the load versus strain curve, referred to as the work of fracture

(which is a measure of the toughness), showed a very large increase over the bioactive glass scaffold alone or the composite with a 200 μm PLA layer.

The mechanical response of composites formed from a bioactive glass scaffold with a gradient in porosity (L3S1 or L4S1 structure) and PLA layer thickness of 400 or 800 μm showed trends similar to the composite with the L1S1 glass structure and PLA layers of the same thickness (Fig. 10b). The measured load at the first peak in the load versus strain curve (referred to as the load-bearing capacity) is summarized in Fig. 11 for all the composites. For a PLA layer thickness of 400 μm , the load-bearing capacity was 100 N, 84 N, and 72 N, respectively, for scaffolds with the L4S1, L3S1, and L1S1 structure. The load-bearing capacity L4S1 glass scaffold with a 400 μm or 800 μm PLA layer increased by $\sim 200\%$ when compared to the L1S1 scaffold without a PLA layer.

SEM images of a composite formed from a 13-93 glass scaffold with the L1S1 structure and 200 μm PLA layer after testing in four-point bending are shown in Fig. 12a, b. The crack initiated at the contact region between the long and short filaments, the same region that showed the highest tensile stress in the FEM simulations. Then the crack propagated further (upward in the z direction) via a path along similar contact regions between the long and short filaments. The initiation and propagation of the crack resulted in a brittle failure mode, similar to the glass scaffold alone, presumably because the composite was unable to support the applied load.

Examination of composites formed from a bioactive glass scaffold (L1S1, L3S1 or L4S1 structure) and PLA layers of thickness 400 or 800 μm after testing to different points of the load vs. strain curve showed the presence of more than one crack in most specimens (Figure 12c, d, e). In general, the occurrence of these cracks was correlated with successive peaks in the load versus strain curve. The first crack was correlated with the first peak and additional cracks were correlated with subsequent peaks. Thus the composite did not fail catastrophically due to the propagation of a single crack. Instead, smaller cracks formed periodically in different parts of the glass scaffold which allowed the composite to maintain its overall integrity as a whole and to continue to support a considerable load.

4. Discussion

The results of the present study showed the ability to significantly improve the load-bearing capacity and to dramatically enhance the work of fracture of strong porous bioactive glass scaffolds in four point bending. This was achieved by the addition of an adherent polymer layer to the external surface of the scaffolds. Finite element simulations of model composites predicted an improvement in the load-bearing capacity of the glass scaffold in four-point bending with increasing thickness and elastic modulus of the polymer layer. Mechanical testing of 13-93 bioactive glass–PLA composites created with structures similar to the models showed effects that were considerably larger and more dramatic than those predicted by the simulations. The load-bearing capacity of the bioactive glass scaffold increased significantly with the addition of the PLA layer. For a sufficiently thick PLA layer (greater than ~12.5% of the scaffold thickness), the work of fracture increased dramatically, resulting in a non-brittle (or “ductile”) mechanical response. These composites, combining bioactivity, high strength, high work of fracture and an internal architecture previously shown to be conducive to bone infiltration, could provide optimal synthetic implants for healing structural bone defects.

4.1 FEM simulations

The FEM analysis focused on simulating the flexural mechanical response of model composite structures composed of a porous glass beam and an adherent polymer surface layer on the top and bottom surface of the beam. The beam geometry was used because it is relevant to flexural testing in four-point bending. The glass had a grid-like structure composed of layers of long (L) filaments along the length of the beam and short (S) filaments in adjacent layers in the orthogonal direction. According to the maximum principal stress theory, failure will occur when the maximum principal stress in a system reaches the value of the maximum stress at the elastic limit in simple tension. Consequently, the analysis focused on determining the magnitude and distribution of the tensile stress in the structure when subjected to a constant load in four-point bending.

For glass structures with a uniform grid-like structure (L1S1) (without a polymer surface layer) the simulations showed that the highest tensile stress was present in the long filaments at the bottom surface of the beam (Fig. 3), in accordance with a previous

study [15]. The addition of an adherent polymer layer to the top and bottom surface of the beam resulted in a reduction in the tensile stress in the glass filaments. The magnitude of the tensile stress in the bottom filaments of the glass scaffold decreased with increasing thickness and elastic modulus of the polymer layer (Fig. 4, 5, 6). However, the reduction predicted by the simulation was $<10\%$ for the thickest PLA layer ($800\text{ }\mu\text{m}$) used in the simulations.

As the polymer layer was assumed to be elastic and perfectly bonded to the glass surface, the reduction in the tensile stress of the glass structure was apparently due to stress transfer to the polymer layer and the capacity of the polymer layer to share a fraction of the applied load. The reduction in the tensile stress of the glass filaments means that when compared to the glass structure alone (without the polymer layer), the composite can support a higher load prior to failure of the brittle glass structure. The composite is predicted to have a higher load-bearing capacity than the glass structure alone. However, because the elastic modulus of the PLA used in the present study (0.65 GPa) was considerably lower than that of the glass (70 GPa), the fraction of the load shared by the polymer layer was limited. The simulations showed similar trends for composites in which the glass structure had a gradient in porosity (L3S1 and L4S1 structures). However, for a given thickness of the polymer layer, the magnitude of the reduction (when compared to the L1S1 glass scaffold without a polymer layer) was larger for the L3S1 structure and even larger still for the L4S1 structure (Fig. 5).

4.2 Observed mechanical response of bioactive glass–PLA composites

The bioactive glass scaffolds created by robotic deposition had grid-like microstructures that well approximated the structures used in the FEM simulations. The glass filaments were almost fully dense and only a few fine pores were found within the cross section of the filaments which corresponded well to the fully dense glass filaments assumed in the models. Tensile testing of PLA specimens at deformation rates of $2\text{--}10\text{ mm/min}$ showed an elastic limit of $1\text{--}2\%$ that was considerably larger than the failure strain ($<0.1\%$) of the bioactive glass scaffolds in four-point bending. Consequently, the PLA layer can be considered to be elastic in four-point bending of the bioactive glass–PLA composites, as assumed in the FEM models.

Examination of the as-fabricated composites showed that the PLA layer adhered to the glass filaments at the surface of the scaffold (Fig. 8). The adhesive strength of the bioactive glass–PLA interface measured in a standard pullout test was 1.0–1.5 MPa. After the pullout test, the surface of the PLA previously in contact with the scaffold showed grooves and bumps that replicated the grid-like structure of the scaffold surface. Residual PLA adhered to the scaffold but it was situated mainly at the junctions between the two outermost layers of glass filaments (Fig. 9). In general, these observations confirmed that the PLA layer adhered to the scaffold but perfect interfacial bonding assumed in the FEM simulations was apparently not present.

For scaffolds with a uniform grid-like microstructure (L1S1), the peak value in the load versus strain curve increased with increasing thickness of the PLA layer (Fig. 10a). The addition of an adherent PLA layer of thickness 400 μm to the top and bottom surfaces of the bioactive glass beam (thickness = 3.2 mm) resulted in a 100% increase in the flexural load that can be supported by the glass beam alone. An increase in the PLA layer thickness to 800 μm produced a further increase in the average peak load but the increase was not significant when compared to the scaffold with the 400 μm PLA layer (Fig. 11).

In general, the observed mechanical response of the bioactive glass–PLA composites in four-point bending showed trends predicted by the FEM simulations but the effects were considerably stronger and more dramatic. The addition of a 400 μm PLA layer improved the load-bearing capacity of the bioactive glass scaffold with the L1S1 structure by ~100%. In comparison, the tensile stress in the glass filaments in the bottom layer of the models was predicted to decrease by ~3% in the FEM simulations. Similar trends were observed for bioactive glass scaffolds with a porosity gradient (L3S1 and L4S1 structures). The difference between the predicted and observed load-bearing capacity of the bioactive glass–PLA composites was presumably due to the deviations of the model assumptions from the as-fabricated composites.

In the FEM model, the glass was assumed to be fully dense and devoid of flaws. In comparison, the mechanical response of brittle materials, particularly when subjected to a tensile stress, is known to be strongly dependent on the presence of surface flaws and internal microstructural flaws. In the present study, the bioactive glass filaments in the as-

fabricated scaffolds were almost fully dense, containing only a few isolated fine pores. Consequently, the difference between the predictions of the FEM simulations and the measured mechanical response was presumably due to the presence of surface flaws in the glass filaments. As the surface of the PLA layer was softened by wetting with CHCl_3 and applied to the surface of the glass scaffold by means of a low applied load, it is likely that the PLA might have filled surface flaws, in addition to adhering to the glass surface. This could result in reducing the effect of the surface flaws present in the as-fabricated glass scaffolds.

A striking feature of the observed mechanical response was that the addition of the PLA layer did not just improve the load-bearing capacity of the bioactive glass scaffold. The PLA layer also dramatically modified the type of mechanical response. A PLA layer thickness of 400 μm ($\sim 12.5\%$ of the glass scaffold thickness) significantly enhanced the work of fracture, in addition to significantly enhancing the load-bearing capacity of the bioactive glass scaffold. Increasing the PLA layer thickness to 800 μm ($\sim 25\%$ of the glass scaffold thickness) did not provide significant improvements in the mechanical response when compared to the 400 μm PLA layer. In comparison, composites with a PLA layer thickness of 200 μm showed a brittle mechanical response typical of the glass scaffold, although there was a significant increase in the failure load (Fig. 11).

As the same process was used to bond the PLA layers to the surface of the bioactive glass scaffolds, it is expected that the interfacial characteristics would be independent of the PLA layer thickness. The difference in mechanical response (brittle versus “ductile”) between the composite with the 200 μm PLA layer and those with the 400 μm or 800 μm PLA layer was presumably due to the processing method used to attach the PLA layer to the glass scaffold. As described earlier, the 200 μm PLA layer was apparently not sufficiently thick to provide complete coverage over the entire surface of the scaffold. A few isolated through-thickness pores were present in the 200 μm PLA layer and the glass under these pores was essentially bare. These bare glass regions, although few in number and small in size, could nevertheless provide sources of brittle failure for the composite with the 200 μm PLA layer.

Another interesting feature of the results was the occurrence of multiple peaks and valleys in the load versus strain curves in four-point bending for composites with a PLA layer thickness of 400 or 800 μm (Fig. 10). These peaks were correlated with the initiation and propagation of successive cracks in the glass scaffold. Furthermore, at strains of up to 5% when the experiments were terminated, the load supported by the composite was comparable or even higher than the load at the first peak. For the glass scaffolds with a PLA layer thickness of 200 μm , a single crack initiated and propagated rapidly, resulting in failure following a peak load. In comparison, multiple cracks formed in succession in the glass scaffold with a PLA layer thickness of 400 or 800 μm , and the spacing between the two surfaces of the crack was much smaller than that for the glass scaffold with the 200 μm PLA layer (Fig. 12). Apparently, these multiple cracks with smaller separation between the crack surfaces enabled the composite to maintain its integrity and support a considerable load.

4.3 Potential of bioactive glass composites for structural bone repair

Although the tough and strong bioactive glass–PLA composites created in the present study were not evaluated in vivo, the bioactive glass scaffolds by themselves (without the PLA surface layer) were shown previously to have a microstructure conducive to bone infiltration in vivo [15]. When implanted in rat calvarial defects for 12 weeks, bioactive glass (13-93) scaffolds with microstructures corresponding to the L1S1, L3S1 and L4S1 structures were infiltrated with new bone. The amount of new bone that infiltrated the pore space of the scaffolds (35–37%) was not dependent on the microstructure of the three groups of scaffolds. Furthermore, the amount of new bone infiltration was higher than that observed for the same glass with a fibrous, trabecular or oriented microstructure [24]. As the PLA layers are present only on the external surface of the bioactive glass scaffold, the porous internal architecture can degrade, release ions that stimulate osteogenesis and support bone infiltration in more or less the same way as a glass scaffold without the PLA layer. The PLA layer on the external surface of the scaffold will degrade and eventually disappear.

Scaffolds of 13-93 bioactive glass with a uniform grid-like (L1S1) microstructure (without a PLA layer), with a compressive strength of 72 ± 10 MPa and flexural strength

of 15 ± 5 MPa, have already shown the capacity to heal segmental defects in rat femurs [13]. Scaffolds of 13-93 glass with a similar microstructure have also shown the capacity to heal segmental defects in rabbit femurs [14]. Bioactive glass (13-93) scaffolds with the L4S1 structure (without a PLA layer) have a higher compressive strength (88 ± 20 MPa) and a significantly higher flexural strength of (34 ± 5 MPa) than the scaffolds used in those studies. With the addition of a 400 μm or 800 μm PLA layer, the flexural load-bearing capacity of the L4S1 scaffold increased by $\sim 33\%$ and $\sim 50\%$, respectively, and its mechanical response changed dramatically from brittle to “ductile”. These composites formed from 13-93 bioactive glass with the L4S1 structure and an adherent PLA surface layer (400 or 800 μm thick) can provide more reliable implants for structural bone repair.

5. Conclusions

The addition of an adherent polylactic acid (PLA) layer to the external surface of strong porous bioactive glass (13-93) scaffolds with a grid-like microstructure significantly enhanced their load-bearing capacity and dramatically modified their mechanical response. Finite element modeling (FEM) predicted an improvement in the load-bearing capacity of the glass scaffolds with increasing thickness and elastic modulus of an adherent polymer surface layer. Mechanical testing of 13-93 bioactive glass–PLA composites created with structures similar to the models showed trends predicted by the FEM simulations but the observed effects were considerably larger and more dramatic. A PLA layer thickness equal $\sim 12.5\%$ of the scaffold thickness increased the load-bearing capacity of the scaffold by $\sim 50\%$ and enhanced the work of fracture increased dramatically, resulting in a change in mechanical response from brittle to “ductile”. These bioactive glass–PLA composites, combining bioactivity, high strength, high work of fracture and an internal architecture known to be conducive to bone infiltration, could provide optimal implants for healing structural bone defects.

Acknowledgements: Supported by the National Institutes of Health (NIDCR), Grant # 1R15DE023987-01 and Missouri University of Science and Technology.

References

- [1] P.V. Giannoudis, H. Dinopoulos, E. Tsiridis, Bone substitutes: an update, *Injury* 36 (2005) S20–7.
- [2] C. Laurencin, Y. Khan, S.F. El-Amin, Bone substitutes, *Expert. Rev. Med. Devices* 3 (2006) 49–57.
- [3] L-C. Gerhardt, A.R. Boccaccini, Bioactive glass and glass–ceramic scaffolds for bone tissue engineering, *Materials* 3 (2010) 3867–910.
- [4] M.N. Rahaman, D.E. Day, B.S. Bal, Q. Fu, S.B. Jung, L.F. Bonewald, A.P. Tomsia, Bioactive glass in tissue engineering, *Acta Biomater.* 7 (2011) 2355–73.
- [5] Q. Fu, E. Saiz, M.N. Rahaman, A.P. Tomsia, Bioactive glass scaffolds for bone tissue engineering: state of the art and future perspectives, *Mater. Sci. Eng. C* 31 (2011) 1245–56.
- [6] J.R. Jones, Review of bioactive glass: From Hench to hybrids, *Acta Biomater.* 9 (2013) 4457– 86.
- [7] S.M. Giannitelli, D. Accoto, M. Trombetta, A. Rainer, Current trends in the design of scaffolds for computer-aided tissue engineering, *Acta Biomater.* 10 (2014) 580–94.
- [8] A. Deliomani, M.N. Rahaman, Direct-write assembly of silicate and borate bioactive glass scaffolds for bone repair, *J. Eur. Ceram. Soc.* 32 (2012) 3637–46.
- [9] X. Liu, M.N. Rahaman, G.E. Hilmas, B.S. Bal, Mechanical properties of bioactive glass scaffolds fabricated by robotic deposition for structural bone repair, *Acta Biomater.* 9 (2013) 7025–34.
- [10] N.D. Doiphode, T.S. Huang, M.C. Leu, M.N. Rahaman, D.E. Day, Freeze extrusion fabrication of 13-93 bioactive glass scaffolds for bone repair, *J Mater Sci: Mater Med* 22 (2011) 515–23.
- [11] Q. Fu, E. Saiz, A.P. Tomsia, Bioinspired strong and highly porous glass scaffolds, *Adv. Funct. Mater.* 21 (2011) 1058–63.
- [12] Q. Fu, E. Saiz, A.P. Tomsia, Direct ink writing of highly porous and strong glass scaffolds for load-bearing bone defects repair and regeneration, *Acta Biomater.* 7 (2011) 3547–54.
- [13] L. Bi, B. Zobell, X. Liu, M.N. Rahaman, L.F. Bonewald, Healing of critical-size segmental defects in rat femora using strong porous bioactive glass scaffolds, *Mater. Sci. Eng. C* 42 (2014) 816–24.
- [14] W. Jia, G.Y. Lau, W. Huang, C. Zhang, A.P. Tomsia, Q. Fu, Bioactive glass for large bone repair, *Adv. Healthc. Mater.* 4 (2015) 2842–8.
- [15] W. Xiao, M. Asle Zaeem, B.S. Bal, M.N. Rahaman, Creation of bioactive glass (13-93) scaffolds for structural bone repair using a combined finite element modeling and rapid prototyping approach, *Mater. Sci. Eng. C* 68 (2016) 651–62.

- [16] F.J. Martinez-Vazquez, F.H. Perera, I. van der Meulen, A. Heise, A. Pajares, P. Miranda, Impregnation of β -tricalcium phosphate robocast scaffolds by in-situ polymerization, *J. Biomed. Mater. Res. A* 101 (2013) 3086–96.
- [17] F.J. Martinez-Vazquez, P. Miranda, F. Guiberteau, A. Pajares, Reinforcing bioceramic scaffolds with in-situ synthesized ϵ -polycaprolactone coatings, *J. Biomed. Mater. Res. A* 101 (2013) 3551–9.
- [18] F.J. Martinez-Vazquez, A. Pajares, F. Guiberteau, P. Miranda, Effect of polymer infiltration on the flexural behavior of β -tricalcium phosphate robocast scaffolds, *Materials* 7 (2014) 4001–18.
- [19] M. Peroglio, L. Gremillard, J. Chevalier, L. Chazeau, C. Gauthier, T. Hamaide, Toughening of bio-ceramics scaffolds by polymer coating, *J. Eur. Ceram. Soc.* 27 (2007) 2679–85.
- [20] Q. Fu, E. Saiz, M.N. Rahaman, A.P. Tomsia, Toward strong yet tough glass and ceramic scaffolds, *Adv. Func. Mater.* 23 (2013) 2461–76.
- [21] Q.Z. Chen, A.R. Boccaccini, Poly(D,L-lactic acid) coated 45S5 Bioglass®-based scaffolds: processing and characterization, *J. Biomed. Mater. Res. A* 3 (2006) 445–57.
- [22] D.E. Day, A. Mohammadkhah, Biodegradable composite scaffold for repairing defects in load-bearing bones, Patent US20140277578A1, Sep 18, 2014.
- [23] A.M. Korsunsky, *Encyclopedia of Materials: Science and Technology*, Oxford (UK), Pergamon, 2001, pp. 2398–404.
- [24] X. Liu, M.N. Rahaman, Y. Liu, B.S. Bal, L.F. Bonewald, Enhanced bone regeneration in surface-modified and BMP-loaded bioactive glass (13-93) scaffolds in a rat calvarial defect model, *Acta Biomater.* 2013;9:7506–17.

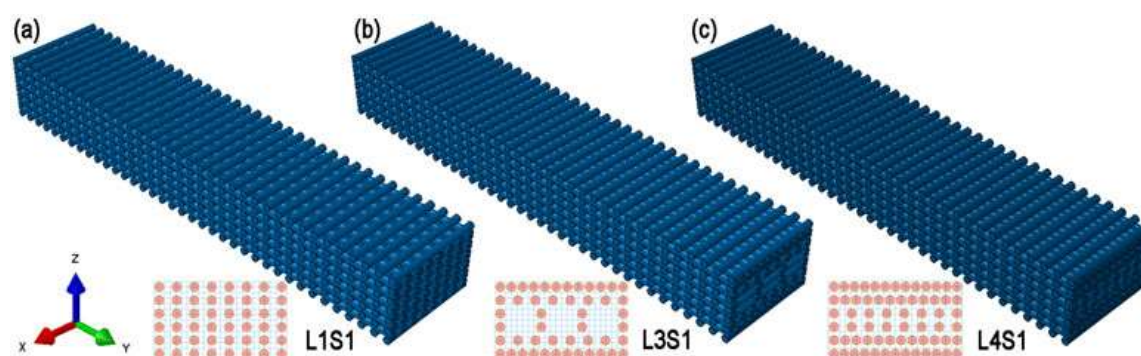


Fig. 1. Three different structures of the glass scaffold analyzed in finite element modeling. Each structure had the external geometry of a beam and was composed of 6 layers of long (L) filaments in the y direction and 7 alternating short (S) filaments in the x direction. The inset under each structure shows the arrangement of the long filaments in the xz plane.

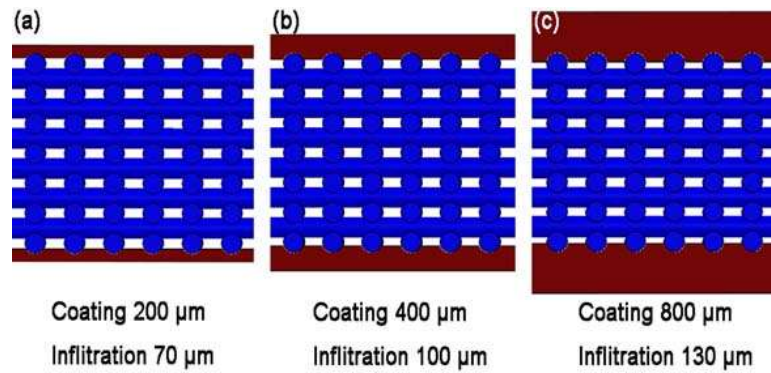


Fig. 2. Cross section of composite composed of glass scaffold and adherent polymer (PLA) surface layer of thickness 200, 400 and 800 μm . The polymer layer was assumed to partially infiltrate the top and bottom surface of the scaffold.

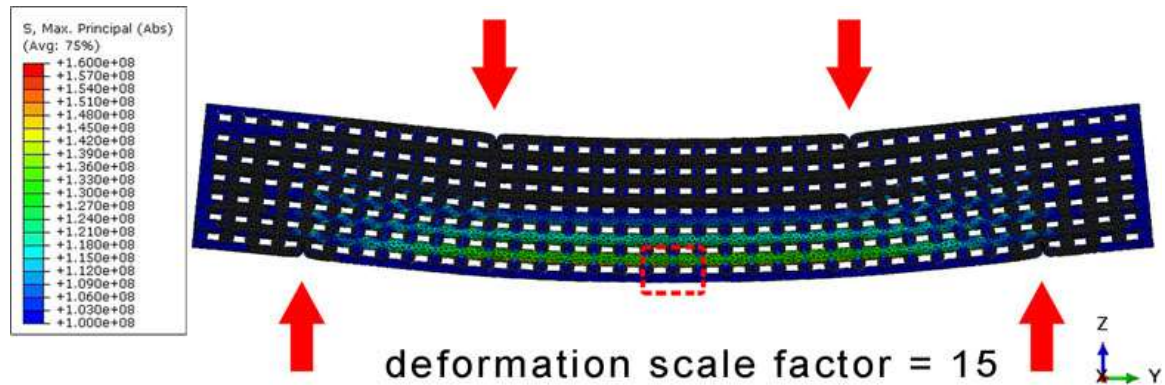


Fig. 3. Typical deformation of glass-polymer composite in four-point bending showing the magnitude and distribution of the stress in the glass filaments and polymer layer as determined by FEM simulations. The actual deformation of the model was magnified by a scale factor of 15 to better show the deformation. The scale on the left gives the maximum principal stress corresponding to specific colors. The box shows the region of most interest in the simulations.

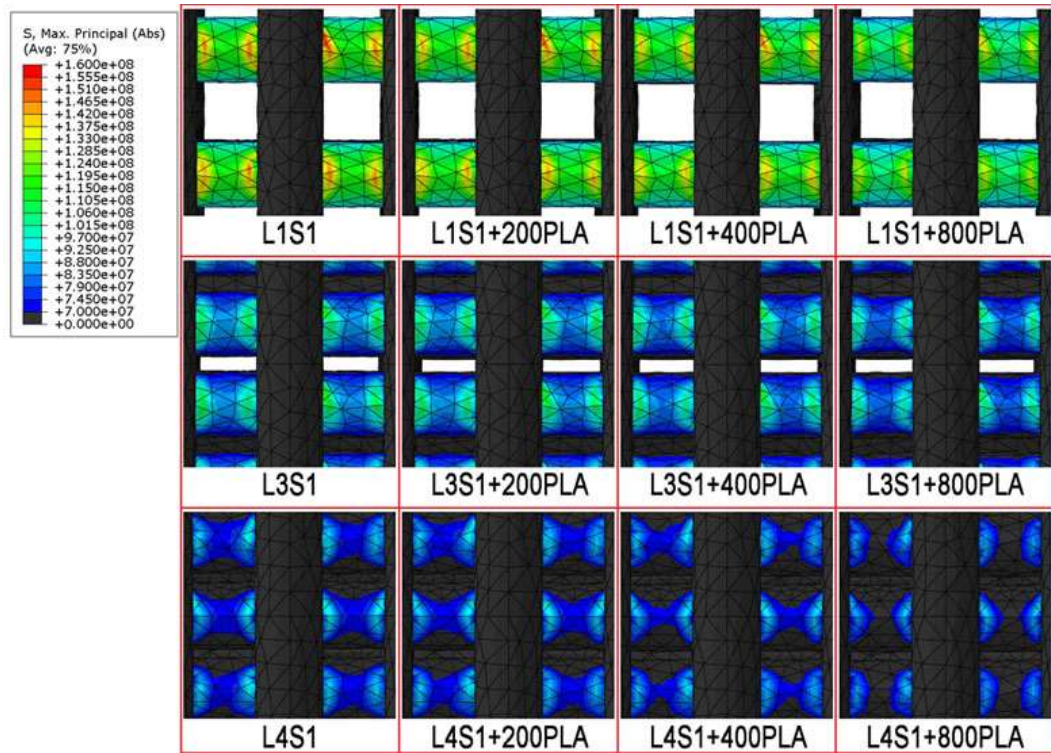


Fig. 4. Magnitude and distribution of the tensile stress in the long filaments of the bottom layers of different models when subjected to the same applied load in four-point bending. The scale on the left gives the maximum principal stress corresponding to specific colors for each row. The designations of the models are given in Table I.

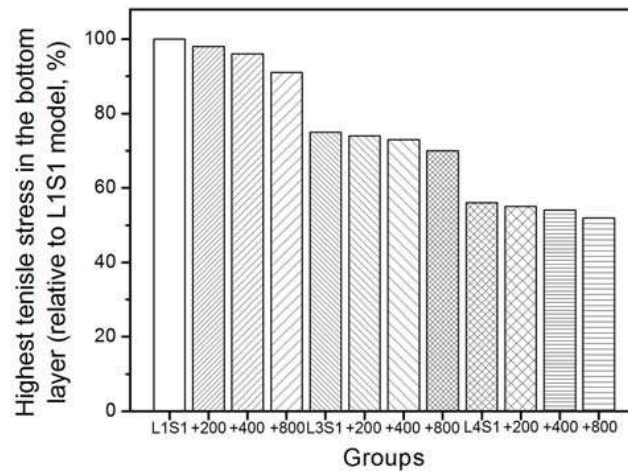


Fig. 5. Highest tensile stress in the long filaments in the bottom layer of the models (normalized to the L1S1 model) determined from FEM simulations of four-point bending under an applied load of 100 N. The region of highest stress corresponded to the middle region of the bottom filaments between the inner span.

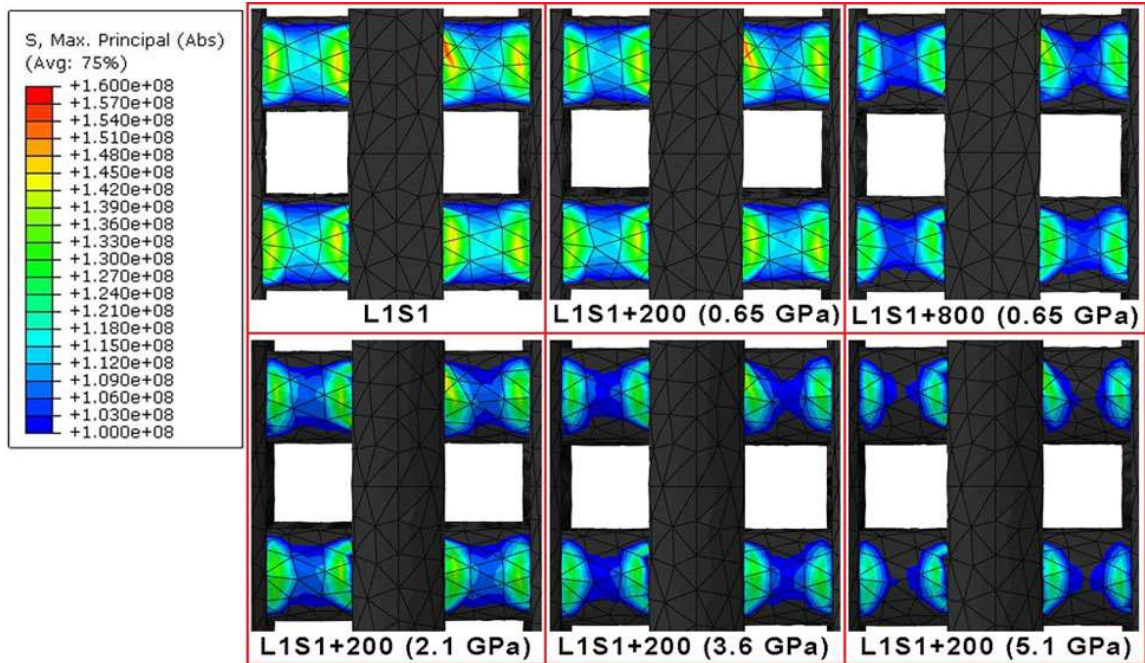


Fig. 6. Magnitude and distribution of the tensile stress in the long filaments of the bottom layers of different models with polymer surface layers of thickness 200 or 800 μm and elastic modulus of 0.65, 2.1, 3.6 and 5.1 GPa when subjected to the same applied load in four-point bending. The scale on the left gives the maximum principal stress corresponding to specific colors.

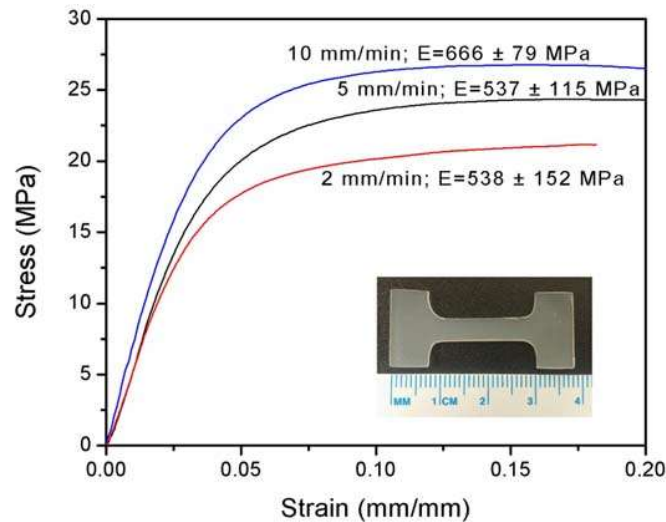


Fig. 7. Stress vs. strain curves for PLA sheets of thickness 800 μm measured in tensile testing of dog-bone specimens (inset) at different deformation rates shown. The Young's modulus is also shown for each deformation rate.

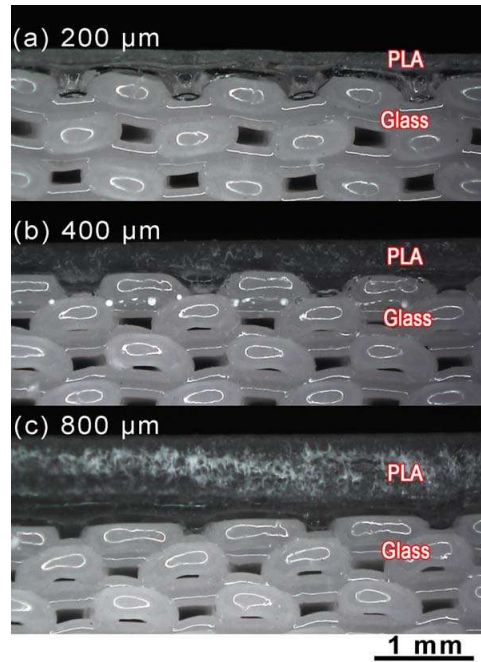


Fig. 8. Side view of as-fabricated composed of bioactive glass (13-93) scaffolds with a grid-like (L1S1) structure and adherent PLA surface layer of thickness (a) 200 μm ; (b) 400 μm ; (c) 800 μm .

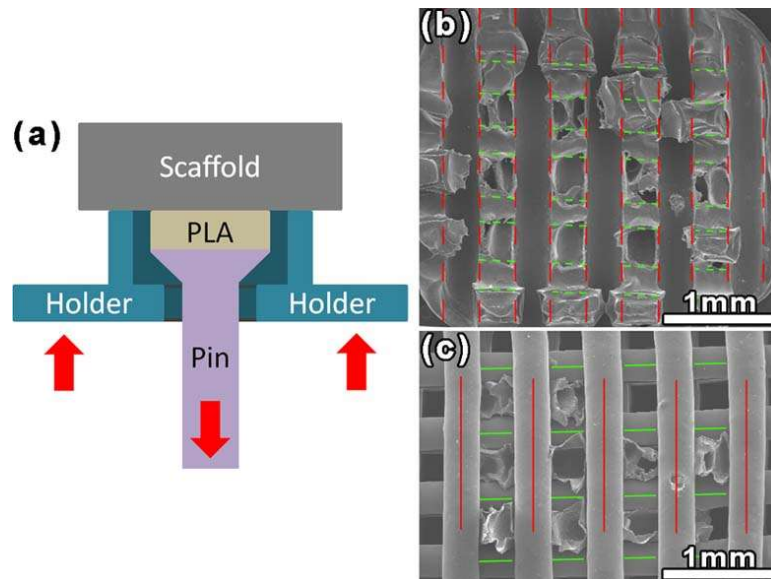


Fig. 9. (a) Schematic diagram illustrating the fixture used in the adhesive strength test; (b) surface of PLA layer (previously in contact with the bioactive glass scaffold) after pullout test; (c) surface of bioactive glass scaffold after pullout test showing residual PLA adhering to the glass. The dashed lines in (b) outline grooves in the PLA layer which replicate the filaments (indicated by solid lines) at the surface of the glass scaffolds in (c).

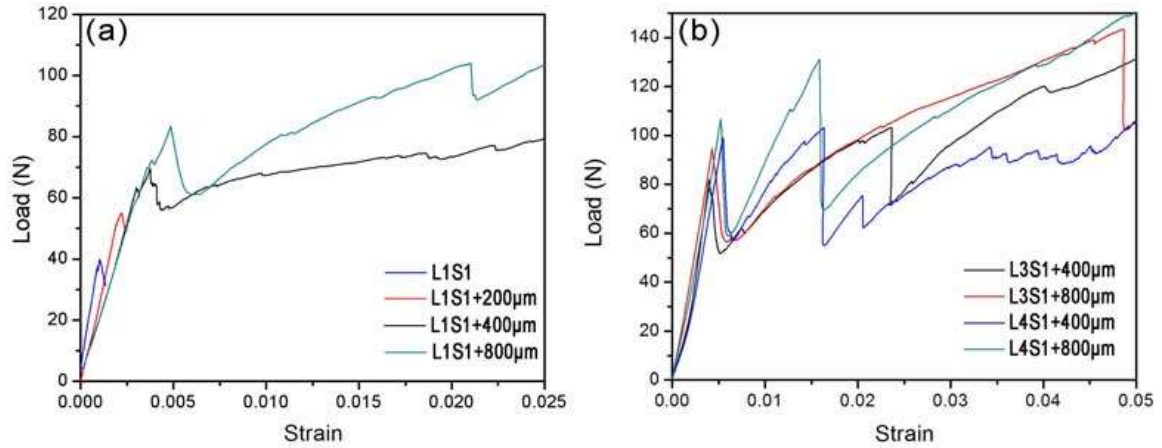


Fig. 10. Typical load vs. strain curves for bioactive glass (without PLA) and composites composed of bioactive glass (13-93) scaffolds with the different scaffold structures with different thickness of PLA coating.

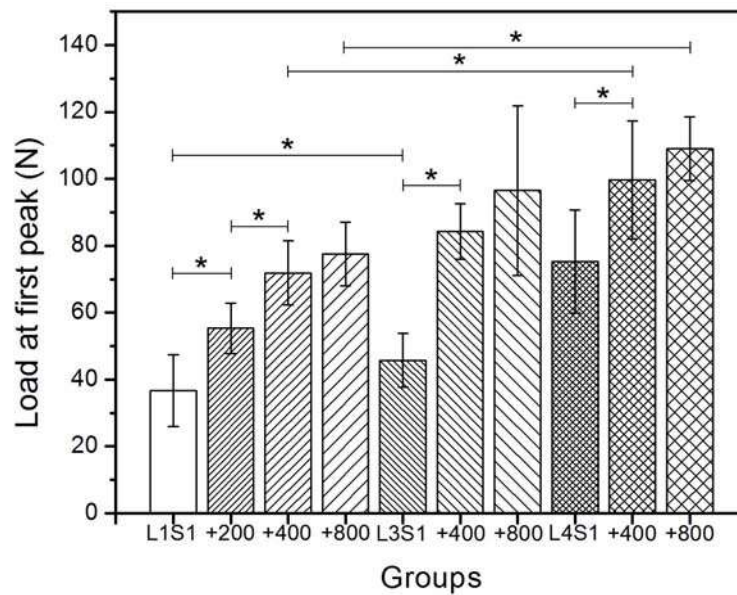


Fig. 11. Measured load at the first peak of the load vs. strain curves in four-point bending for different groups of bioactive glass scaffolds (L1S1, L3S1 and L4S1) and composites of these scaffolds with PLA surface layers of thickness 200, 400 or 800 µm. (* significant difference between groups; $p < 0.05$).

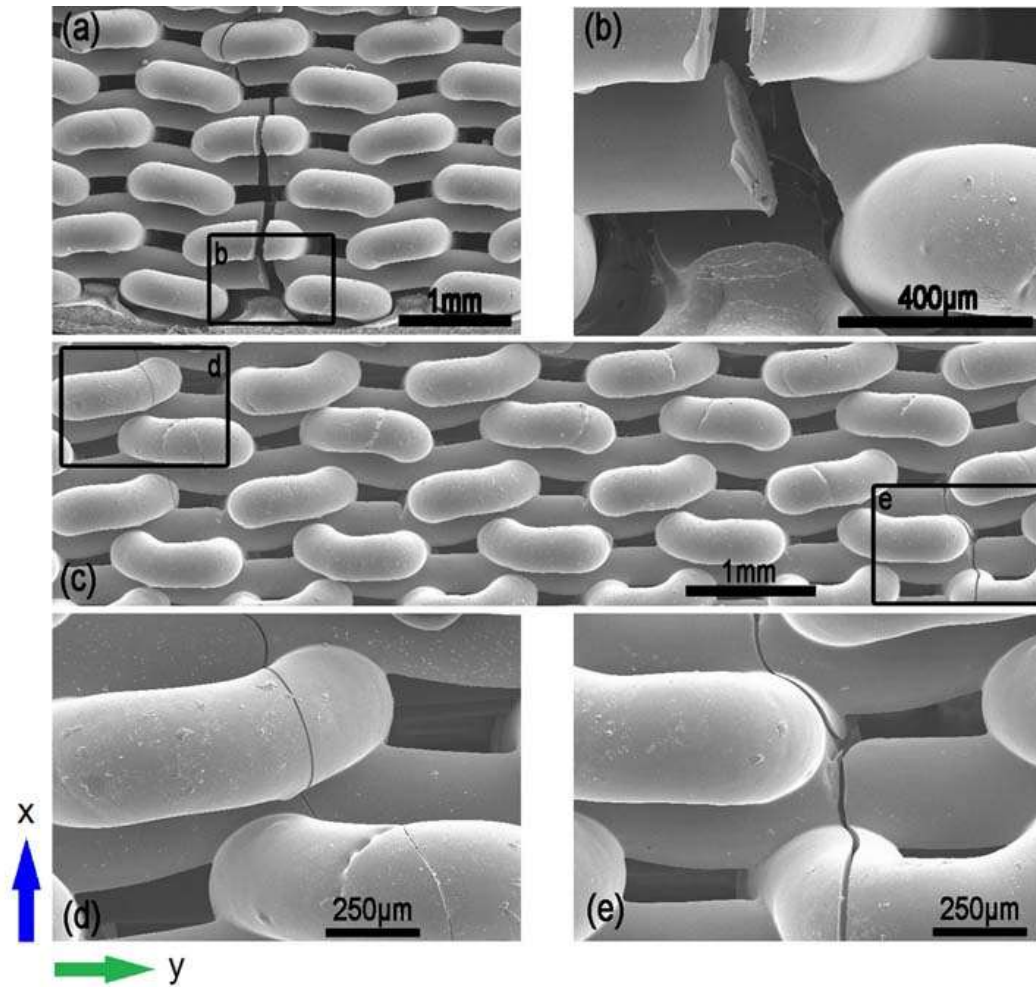


Fig. 12. SEM images of bioactive glass–PLA composites (yz plane) after testing to specific strains in four-point bending. (a) Glass scaffold with the L1S1 structure and PLA layer thickness of 200 μm ; a magnified images of the boxed area in (a) is shown in (b). (c) Glass scaffold with the L4S1 structure and PLA layer thickness of 400 μm ; magnified images of the boxed areas in (c) are shown in (d) and (e).

Table I. Summary of models analyzed in FEM simulations.

Glass scaffold architecture	Polymer (PLA) layer thickness (μm)		
	200	400	800
L1S1	L1S1+200	L1S1+400	L1S1+800
L3S1	L3S1+200	L3S1+400	L3S1+800
L4S1	L4S1+200	L4S1+400	L4S1+800

SECTION

2. CONCLUSIONS

1. Hollow hydroxyapatite (HA) microspheres with a high-surface-area mesoporous shell wall, prepared by a borate glass conversion route near room temperature, can provide a novel carrier for local delivery of bone morphogenetic protein-2 (BMP2) to stimulate bone regeneration.
2. The release of BMP2 from the hollow HA microspheres can be further controlled, particularly at early times, by coating the microspheres with a biodegradable polymer of varying thickness.
3. When loaded with BMP2 (1 μg per defect), the hollow HA microspheres significantly enhanced bone regeneration in rat calvarial defects at 3–6 weeks postimplantation.
4. Hollow microspheres with controllable amounts of carbonate substitution (0–12 wt. %) can be prepared by modifying the process variable in the glass conversion route.
5. Hollow HA microspheres with 12.4 wt. % carbonate ions showed a higher surface area ($236 \text{ m}^2 \text{ g}^{-1}$) than hollow HA microspheres prepared without carbonate substitution ($179 \text{ m}^2 \text{ g}^{-1}$) and a faster degradation rate in a potassium acetate buffer solution in vitro.
6. When implanted for 12 weeks in rat calvarial defects, the hollow HA microspheres (with or without carbonate substitution) showed a limited capacity to regenerate bone in rat calvarial defects but the carbonate-substituted HA microspheres (12.4 wt. % carbonate ions) resorbed faster than the HA microspheres without carbonate substitution.
7. When loaded with BMP2 (1 μg per defect), the carbonate-substituted hollow HA microspheres stimulated bone regeneration and resorbed faster than the HA microspheres without carbonate substitution.
8. The combination of carbonate-substituted hollow HA microspheres and clinically-safe doses of BMP2 could provide promising implants for healing non-loaded bone defects.
9. Finite element modeling (FEM) provided an efficient approach to simulate the mechanical response of a variety of glass architectures relevant to the development of strong porous bioactive glass scaffolds.
- 10 Mechanical testing of bioactive glass (13-93) scaffolds created with microstructures approximating the finite element models by a robotic deposition technique showed results that validated the predictions of the FEM simulations.

11. Bioactive glass (13-93) scaffolds with a porosity gradient, composed of a higher porosity inner region and a lower porosity outer region to better mimic human long bones, showed a flexural strength that was more than twice the value for a uniform grid-like microstructure, a higher average compressive strength and a comparable capacity to support bone infiltration in vivo.
12. The addition of an adherent polylactic acid (PLA) layer to the external surface of strong porous bioactive glass (13-93) scaffolds with a grid-like microstructure significantly enhanced their load-bearing capacity by ~50% and dramatically modified their mechanical response.
13. The measured load-bearing capacity of the glass scaffold increased with increasing PLA layer thickness and, above a certain PLA thickness (<12.5% of the scaffold thickness), the work of fracture increased dramatically, resulting in a non-brittle (or “ductile”) mechanical response.
14. The bioactive glass–PLA composites created in this study, combining bioactivity, high strength, high work of fracture and an internal architecture conducive to bone infiltration, could provide optimal implants for healing structural bone defects.

3. SUGGESTIONS FOR FUTURE WORK

1. Create and evaluate hollow carbonate-substituted HA microspheres doped with therapeutic ions

Trace amount of elements such as Cu, Zn and Sr are known to be beneficial for bone regeneration. Hollow carbonate-substituted HA microspheres doped with these elements should be studied to evaluate their ability to enhance bone regeneration and angiogenesis in osseous defects without the use of growth factors.

2. Determine the optimal amount of BMP2 for use with hollow HA microspheres

The amount of BMP2 loading (1 $\mu\text{g}/\text{defect}$) used in this study was based on data in the literature for the same animal model. It is not clear whether the amount used in this study is the optimal amount for bone regeneration. BMP2 is expensive and large amounts of BMP2 can have adverse effects in vivo. Hollow carbonate-substituted HA microspheres doped with therapeutic ions could potentially reduce the amount of BMP2 required for same amount of new bone. The microspheres loaded with different amounts of BMP2 should be evaluated in bone defects to determine the optimal BMP2 dose.

3. Improve sophistication of finite element modeling

The simulations performed in this study assumed glass filaments without surface flaws. In practice, glasses commonly contain surface flaws such as pores and microcracks that have a strong effect on their mechanical response, particularly when subjected to tensile stresses. Incorporation of controlled surface flaws of the glass into the finite element simulations could potentially provide further insight into creating bioactive glass scaffolds with improved mechanical properties.

4. Evaluation of bioactive glass–PLA composites in loaded bone defect model

The present study culminated in the creation of bioactive glass-based scaffolds with a desirable combination of properties that have sought after for several years: bioactivity, high compressive strength, high flexural strength, non-brittle mechanical response and an internal architecture conducive to bone infiltration. The composites should be evaluated in a loaded bone defect model, such as critical-size segmental defects in rabbit femurs. Bone regeneration in the defects and the biomechanical properties of the scaffolds should be studied as a function of implantation time.

APPENDIX

Three-Dimensional Printing of Silicon Nitride with Controllable Shape and Architecture by Robocasting

Santuan Zhao, Wei Xiao, Mohamed N. Rahaman

Department of Materials Science and Engineering, Missouri University of Science and Technology, Rolla, MO 65409, USA

David O'Brien, Jacob W. Seitz-Sampson

Amedica Corporation, 1885 West 2100 South, Salt Lake City, UT 84119, USA

B. Sonny Bal

Department of Orthopaedic Surgery, University of Missouri, Columbia, MO 65212, USA

Abstract

Silicon nitride (Si_3N_4) implants are used in spinal fusion surgery and are under development for use as bearings in total joint arthroplasty. The ability to create Si_3N_4 implants with anatomically relevant shapes and controllable architecture can be beneficial in these orthopedic applications. In the present study, an aqueous paste composed of Si_3N_4 powder and sintering additives was prepared with the requisite rheology and formed into structures with different geometry and architecture using a robotic deposition technique. Sintering and hot isostatic pressing produced an almost fully dense Si_3N_4 phase (density = $3.23 \pm 0.02 \text{ g/cm}^3$) with a fibrous microstructure. Four-point bending tests of as-fabricated dense beams showed a flexural strength of $552 \pm 68 \text{ MPa}$. Together, these results indicate that robotic deposition combined with sintering and hot isostatic pressing can provide a manufacturing strategy to create Si_3N_4 implants with controllable shape and architecture for applications in orthopedic surgery.

Introduction

During the past 50 years, silicon nitride (Si_3N_4) has developed into a well-established material for several structural applications, at both ambient and high

temperatures, due to its attractive combination of properties such as mechanical strength, resistance to thermal shock, high-temperature stability, hardness and wear resistance.^{1–3} Si_3N_4 materials fabricated by conventional powder processing routes can be modified by controlled thermal treatment to produce a microstructure composed of elongated (fibrous) grains with enhanced fracture toughness. These *in situ* toughened Si_3N_4 ceramics have shown a combination of flexural strength (>1 GPa) and fracture toughness (up to $10 \text{ MPa m}^{1/2}$) that are among the highest measured values for ceramic materials.^{3,4} Medical grade Si_3N_4 has also been shown to be biocompatible, stable *in vivo* and visible on X-ray radiographs as a partially radiolucent implant material.^{6,7} Based on these desirable properties, in addition to the aforementioned high strength and fracture toughness, Si_3N_4 is used clinically as spinal fusion implants and it is being developed for other biomedical applications such as bearings in hip and knee joint arthroplasty.^{8–10}

Near net shape fabrication of Si_3N_4 materials with the requisite geometry (shape) and architecture is particularly desirable for custom orthopedic applications but it is also relevant to other applications, such as high-temperature mechanical engineering applications. As Si_3N_4 has a high hardness, post-fabrication machining of the dense material to achieve the desired complexity in shape and architecture can be costly. In particular, biomedical implants are often required to have a complex shape to fit into existing bone defects or unusual patient anatomy and an architecture that is dense, porous or has a graded porosity, depending on the specific application. For example, some implants for spinal repair should have a dense Si_3N_4 phase to provide the requisite strength and a porous internal architecture for bone infiltration and integration.

Conventional forming methods such as injection molding,^{11,12} slip casting^{13,14} and gelcasting^{15,16} have been used for near net shape fabrication of Si_3N_4 ceramics with simple and complex shapes. However, they are limited in their ability to produce architectures with a controlled spatial distribution of porosity and the requisite pore size to facilitate integration of the implants with host bone. In comparison, it has been well demonstrated that additive manufacturing techniques, sometimes referred to as three-dimensional (3D) printing, can provide unprecedented control of the shape and internal architecture (or microstructure) of ceramic green parts.

Robocasting is a colloidal-based additive manufacturing method based on computer-controlled layer-by-layer deposition of a highly concentrated suspension (slurry or paste) through a nozzle of diameter $\sim 100\text{ }\mu\text{m}$ to 1 mm .^{17,18} Robocasting has been used to form green parts of structural ceramics such as alumina^{18,19} and silicon carbide^{19,20}, bioceramics such as hydroxyapatite and beta-tricalcium phosphate^{21–23} and bioactive glass.^{24–26} Robocasting has also been used to form Si_3N_4 parts from aqueous slurries composed of high solids loading (52 vol. % Si_3N_4 particles of size $0.77\text{ }\mu\text{m}$), low concentration of an anionic polyelectrolyte (1 wt. % Darvan 821A) and a flocculating agent (0.4 wt. % aluminum nitrate) at pH 7.8 to 8.5.²⁷ Sintering produced a linear shrinkage of 16% and a final density of 3.21 g/cm^3 which was $\sim 99\%$ of the theoretical density, while four-point bending tests of the sintered material showed a flexural strength of $737 \pm 38\text{ MPa}$.

The objectives of the present study were two-fold. One objective was to develop a paste formulation for continuous and reproducible robocasting of Si_3N_4 parts from a commonly-used commercial powder (SN-E10; UBE Industries, Japan). Because of its fine particle size, this powder is known to have attractive sintering characteristics but difficulties have been reported in dispersing it in aqueous media to high solids loading.²⁸ The second objective was to create Si_3N_4 parts with different shape and architecture by robocasting. The green parts were dried, debinded, fired using a combined sintering and hot isostatic pressing route, and characterized to evaluate their macrostructure, microstructure and mechanical properties.

Experimental procedure

Starting powders

The Si_3N_4 powder (SN-E10; UBE Industries, Tokyo, Japan) used in this study had an average particle size (D50) of $0.70\text{ }\mu\text{m}$, a surface area of 9 to $13\text{ m}^2/\text{g}$ and α phase content of $> 95\%$ according to the manufacturer's specifications. The sintering additives that would lead to the formation of a liquid phase to aid densification were 6.0 wt. % Y_2O_3 (D50 = $0.5\text{ }\mu\text{m}$; purity 98.9%; H. C. Starck, Germany) and 4.0 wt. % Al_2O_3 (D50 = $0.3\text{ }\mu\text{m}$; purity = 99.0%; Baikowski Malakoff, USA) which are a commonly-used formulation in the production of Si_3N_4 materials. In addition, 0.75 wt. % TiO_2 (D50 < 0.9

μm ; purity 99.8%; Spectrum Chemical, USA) was used as a colorant. The starting mixture composed of Si_3N_4 powder, sintering additives and colorant were mixed in a V-blender and provided by a manufacturer of Si_3N_4 orthopedic implants (Amedica Corp., Salt Lake City, UT).

The particle size distribution of the Si_3N_4 powder (without additives) was checked using a particle size analyzer (S3500; Microtrac, Largo, FL). Dilute suspensions composed of 0.002 vol. % Si_3N_4 particles were used in measuring the zeta potential as a function of pH using a Zetasizer Nano ZS90 machine (Malvern Instruments Ltd., Malvern, UK).

Preparation of suspensions and viscosity measurements

Based on the zeta potential data for the Si_3N_4 powder, a cationic polyelectrolyte, polyethylenimine (PEI) (Aldrich Chemical Co., Milwaukee, WI), was used as a dispersant–binder system. PEI is effectively neutral at pH values above ~ 10 and develops an increasing positive charge as the pH decreases below this value due to adsorption of H^+ ions, with the amine groups becoming $\sim 50\%$ protonated at pH of 5 to 6.²⁹ The optimal amount of PEI was assessed from measurements of the viscosity versus shear strain rate for Si_3N_4 suspensions containing varying amounts of PEI (as described below).

The powder mixture, composed of Si_3N_4 powder and sintering additives ($\text{Y}_2\text{O}_3 + \text{Al}_2\text{O}_3$), referred to simply as Si_3N_4 powder, was sieved through a 100 mesh nylon sieve to remove large agglomerates. Suspensions were prepared for use in rheological measurements by adding the Si_3N_4 powder to a solution of PEI in deionized water, followed by mixing in a planetary centrifugal mixer (ARE-310; THINKY, Laguna Hills, CA). Suspensions composed of 20 vol. % Si_3N_4 powder and varying amounts of PEI (0 to 8 wt. % based on the weight of the Si_3N_4 powder) composed of a high molecular weight PEI (designated H-PEI; molecular weight $M_w = 25,000$ Da), a low molecular weight PEI (L-PEI; $M_w = 2,000$ Da) or a combination of H-PEI and L-PEI were studied. The viscosity of the suspensions was measured at room temperature using a controlled-rate rotational viscometer (Haake Viscotester E; Haake Inc., Paramus, NJ) with a small

sample adaptor. Measurements were performed with TR series spindles, using 8 to 13 ml of suspension. The shear stress was measured as a function of the shear rate.

Paste preparation for robocasting

The as-received Si_3N_4 powder (with sintering additives), sieved through a 100-mesh sieve to remove large agglomerates, was added to a solution composed of deionized water and the requisite amount of PEI, and the system was mixed using a planetary centrifugal mixer (ARE-310; THINKY). Based on the aforementioned viscosity measurements, a combination of 4.0 wt. % L-PEI and 4.0 wt. % H-PEI was used. The powder was added to the solution in steps and mixed for 1 min after each step. Then hydroxypropyl methyl cellulose (Methocel F4M; Mw = 3500 Da; Dow Chemical Co., Midland, MI), abbreviated HPMC, was added to the slurry and the system was mixed in the planetary mixer for 1 min. The HPMC was used as a viscosifying agent to modify the rheology of the paste.²⁰ Pastes containing varying amounts of HPMC were tested to determine the optimal amount required to achieve continuous robocasting of green parts without any visible flaws. The composition of the paste used for robocasting the Si_3N_4 parts in this study is given in Table I.

Robocasting of silicon nitride

Green parts were formed using a robotic deposition apparatus (3D Inks; Stillwater, OK). The three-axis motion of the x, y and z stages was independently controlled by a computer-aided program (RoboCAD 3.0) that allowed for layer-by-layer deposition of 3D architectures. The paste was contained in a 3 ml syringe and deposited through a tapered stainless steel nozzle (inner diameter = 410 μm) held in a plastic housing (EFD precision tips, East Providence, RI). A constant pressure was applied to extrude the paste through the nozzle at a volumetric flow rate required to maintain a constant xy table speed of 10 mm/s.

The center-to-center distance between the extruded filaments was varied to achieve two different architectures. A center-to-center distance of 910 μm was used to form a porous grid-like architecture composed of filaments arranged at right angles in adjacent layers and square-shaped pores in the plane of deposition. In comparison, a

center-to-center distance of 410 μm was used to form a grid-like architecture composed of touching filaments in the plane of deposition. This architecture is referred to as a “solid” architecture to distinguish it from the porous grid-like architecture. For each architecture, green parts were formed with the external geometry of a cube (~ 10 mm in length) or a beam ($32\text{ mm} \times 6\text{ mm} \times 4\text{ mm}$). The green parts were dried for 24 h at room temperature, followed by 24 h at 70 $^{\circ}\text{C}$.

Binder removal and firing

Thermogravimetric analysis (TGA) was performed to determine the binder burnout profile of the processing additives alone (L-PEI, H-PEI and HPMC) and the Si_3N_4 green parts. A mass of 10 mg was heated in air at 5 $^{\circ}\text{C}/\text{min}$ to 600 $^{\circ}\text{C}$ using a thermal analysis instrument (STA 409C; Netsch, Selb, Germany). Then the weight loss curve was used to develop a heating schedule for the dried parts. Binder burnout was performed by heating the green parts in air at 2 $^{\circ}\text{C}/\text{min}$ to 600 $^{\circ}\text{C}$, with a hold of 2 h at 300 $^{\circ}\text{C}$ and at 600 $^{\circ}\text{C}$. The debinded parts were densified by a combination of sintering and hot isostatic pressing (referred to as sinter/HIP) according to a schedule previously developed at Amedica Corporation. Sintering was performed for 2 h at ~ 1700 $^{\circ}\text{C}$ in an N_2 atmosphere. Then the sintered samples were further treated by hot isostatic pressing for 2 h at ~ 1700 $^{\circ}\text{C}$ and N_2 gas pressure of ~ 200 MPa.

Characterization of green and fabricated Si_3N_4 parts

The density of the as-fabricated parts was measured using the Archimedes technique according to ASTM C373-88. The linear shrinkage in the sinter/HIP process was determined from the dimensions of the dried and final parts. Field-emission scanning electron microscope (SEM) (S-4700; Hitachi, Tokyo, Japan) was used to examine the microstructure of the debinded and final parts. Fractured and polished cross sections of the samples were coated with Au/Pd and examined at an accelerating voltage of 15 kV and a working distance of 12 mm.

As-fabricated parts with the shape of beams ($23 \times 4.3 \times 2.8$ mm) were tested in four-point bending according to ASTM C1674-11 to determine their flexural strength. Testing was performed at a crosshead speed of 0.2 mm/min in an Instron testing machine

(Model 5881; Norwood, MA) using a fully articulated fixture (outer span = 20 mm; inner span = 10 mm). The flexural strength was determined using the equation

$$\sigma = \frac{3PL}{4bd^2} \quad (1)$$

where P is the applied load, L is the outer span, b is the sample width and d is the thickness of the sample. Six samples in each group were tested and the flexural strength was determined as an average \pm standard deviation.

Results

Characteristics of slurries and green parts

Figure 1 shows the particle size distribution and the zeta potential vs. pH for the as-received Si_3N_4 powder (without sintering additives). The average particle size $D_{50} = 0.7 \mu\text{m}$ is consistent with the manufacturer's specifications. The zeta potential curve and the isoelectric point ($\text{IEP} = 6.2$) of the Si_3N_4 powder are consistent with results in the literature for Si_3N_4 powder with the same manufacturer's designation.³⁰ Although the IEP of the sintering additives was not measured, several studies have reported the IEP of high purity Al_2O_3 in the range 8 to 9 and Y_2O_3 in the range 8.5 to 9.5. As these are almost stoichiometric oxides, the IEPs of high purity Al_2O_3 and Y_2O_3 are not expected to deviate from these narrow ranges.

Addition of PEI (4.0 wt. % L-PEI + 4.0 wt. % H-PEI based on the mass of Si_3N_4 powder) to deionized water raised its pH to 11.5. Addition of 20 vol. % Si_3N_4 powder (with Y_2O_3 + Al_2O_3 sintering additives) to the PEI solution produced little change in the pH (to 11.4), indicating that the dispersion of the Si_3N_4 particles was dominated by the adsorbed PEI. Figure 2a shows the effect of the amount of H-PEI on the viscosity and rheological behavior of 20 vol. % Si_3N_4 suspensions. The viscosity decreased and the rheological behavior changed from shear thinning to essentially Newtonian as the amount of H-PEI increased from 0 to 4 wt. %. Increasing the amount of H-PEI to 8 wt. % showed little further change in viscosity or rheological behavior. The effect of a combination of H-PEI and L-PEI on the viscosity and rheological behavior of 20 vol. % Si_3N_4 suspensions is shown in Figure 2b. The use of 8 wt. % of L-PEI alone did not produce a marked difference in viscosity and rheological behavior when compared to the suspension without PEI, indicating that this amount of L-PEI was insufficient to provide

good dispersion of the particles. In comparison, a combination of 4.0 wt. % L-PEI + 4.0 wt. % H-PEI resulted in a reduction in the viscosity and a near Newtonian rheological response which was almost identical to the use of 8.0 wt. % H-PEI.

A combination of 4.0 wt. % H-PEI + 4.0 wt. % L-PEI was used for robocasting because it allowed the incorporation of a slightly higher volume fraction of Si_3N_4 particles into the paste when compared to slurries with 8.0 wt. % H-PEI. These pastes were extrudable but the filaments in the porous grid-like architecture showed some deformation while the ability to continuously form green parts without flaws was limited. HPMC additions below 1.0 wt. % (based on the weight of Si_3N_4) did not adequately improve the forming process whereas HPMC additions greater than 2.5 wt. % required a reduction in the solids content for successful robocasting. The optimal amount of HPMC used in the slurries was ~ 1.5 wt. %.

Figure 3 shows examples of green parts formed by robocasting. Two different shapes were formed, a cube and a beam, based on the geometry required for mechanical testing in compression and flexure. For each geometry, parts were created with a porous grid-like architecture and a solid architecture. All of the green parts showed a uniform shape and architecture and there was no observable deformation of the individual filaments in the structures.

Debinding of green parts

Figure 4 shows TGA curves for the binder system used in this study (without the Si_3N_4 powder) and for filaments formed by robocasting which were composed of the same binder system with the Si_3N_4 powder. The samples were dried prior to TGA. The curve for the binder system without Si_3N_4 powder can be divided into three regions. The first region showed a gradual weight loss between ~ 100 °C and ~ 300 °C in which ~ 20 wt. % of the binder was removed. The second region between ~ 300 °C and ~ 400 °C showed a much steeper weight loss, with ~ 40 to 50 wt. % of the binder being removed. In the third region (above ~ 400 °C), the weight loss curve decreased more slowly and not all of the binder was removed at the heating rate used (5 °C/min) when the experiment was terminated at 600 °C.

The binder burnout curve for the filament composed of the Si_3N_4 powder and the binder system can also be divided into three regions but they were less distinct. The curve showed a more gradual decrease with temperature over the entire range (room temperature to 600 °C). Although the weight loss curve showed the steepest drop between 300 °C and 400 °C, it was not as distinctive as in Fig. 4a. It appeared that the Si_3N_4 powder and sintering additives ($\text{Y}_2\text{O}_3 + \text{Al}_2\text{O}_3$) might be having a catalytic effect on the binder decomposition, leading to a relatively greater amount of weight loss in the first region (below ~300 °C) relative to that in the second region.

SEM images of the surface and fractured cross section of a filament after binder burnout are shown in Fig. 5 at different magnifications. As might be expected, the surface morphology was smoother than the fractured cross section (Fig. 5a, b). Higher magnification images showed a fairly homogeneous particle packing and the absence of large pores (Fig. 5c, d). At an even higher magnification, SEM images indicated that the largest pores had a size smaller than 1 to 2 μm (Fig. 5e, f).

Microstructure of fabricated Si_3N_4 parts

Optical images of the Si_3N_4 parts after sinter/HIP (Fig. 6) showed no observable distortion of the external shape of the parts and no observable deformation of the filaments in the parts with the porous grid-like architecture when compared to the green parts (Fig. 3). The apparent density of the solid phase in the porous grid-like parts was $3.18 \pm 0.01 \text{ g/cm}^3$, approximately 99% of the value ($\sim 3.23 \text{ g/cm}^3$) reported in the literature for fully-dense Si_3N_4 fabricated with the sintering additives used in this study. The porosity of the open macropores in the porous grid-like parts was 51.5% and 56.5 %, respectively, for the cube-shaped and beam-shaped samples, and the pore width was $\sim 350 \mu\text{m}$ in the plane of deposition. The bulk density of the parts with the solid architecture was $3.23 \pm 0.02 \text{ g/cm}^3$, approximately equal to the density of a fully dense material. The average of the measured densities for the porous grid-like parts or the solid parts was not dependent on the geometry of the parts (cube or beam). The linear shrinkage of the samples after sinter/HIP was 27.8%.

SEM images of the polished cross section (in the z direction) of the cube-shaped parts with the porous grid-like architecture are shown in Fig. 7a, c. The higher

magnification image showed few isolated pores of size $<1\ \mu\text{m}$ in the solid phase. At similar magnification, images of cube-shaped samples with the solid architecture showed a fully dense microstructure (Fig. 7b, d).

SEM images of the surface of the filaments in the as-fabricated Si_3N_4 parts with a porous grid-like architecture (Fig. 8a, b, c) showed a fibrous microstructure of rod-like grains (diameter 1 to 2 μm). The rod-like grains had a hexagonal cross section typical of $\beta\text{-Si}_3\text{N}_4$ and there appeared to be little glass phase (or solidified liquid phase) between these rod-like grains on the filament surface. Examination of the fractured cross section on the filaments (Fig. 8d) showed that the rod-like grains were also present within the filaments, as seen particularly in the areas with more pronounced intergranular fracture. These fibrous grains within the filaments had a diameter that was approximately the same as those on the surface but they appeared to be bonded together by the solidified liquid phase.

Mechanical properties of as-fabricated Si_3N_4 parts

The compressive strength of the cube-shaped parts was not determined because the required force was higher than the capacity of the available load cell (10 kN) in the mechanical testing machine. This means that the compressive strength of the porous grid-like parts (porosity of macropores = 51.5%) was higher than $\sim 200\ \text{MPa}$. The fully dense parts with the solid architecture is expected to have a considerably higher compressive strength. Four-point bending tests of the as-fabricated beams showed a flexural strength of $552 \pm 68\ \text{MPa}$ for the solid parts and $89 \pm 11\ \text{MPa}$ for the porous grid-like parts (porosity of macropores = 56.5%). SEM images of the fractured surface of the samples after flexural testing (Fig. 9) showed a combination of intergranular and transgranular fracture modes. The bottom region of the samples, under tension in the four-point tests, apparently showed a larger amount of intergranular fracture than the top region (under compression during the tests). However, there was no marked difference in fracture morphology between the parts with the solid architecture and the porous grid-like architecture.

Discussion

The development of an aqueous paste composed of a fine commercial Si_3N_4 powder, commonly-used sintering additives ($\text{Y}_2\text{O}_3 + \text{Al}_2\text{O}_3$) and organic processing additives allowed the continuous and reproducible robocasting of green parts with different geometry and architecture. A combination of sintering and hot isostatic pressing (sinter/HIP) resulted in the production of parts without any observable shape deformation and with an almost fully dense Si_3N_4 phase composed of rod-like grains. Testing of as-fabricated dense parts in four-point bending showed an average flexural strength of 552 MPa. The fabrication process used in the present study could provide a viable manufacturing strategy for the creation of Si_3N_4 implants with complex architectures and anatomically-relevant shapes for applications in orthopedic surgery.

Paste development and robotic deposition

The structural integrity of green parts created by robocasting is strongly dependent on the rheological properties of the paste (or slurry) and on the drying of the deposited layers. In addition to high solids loading, the slurry should have the requisite rheology to flow through the nozzle but then set rapidly to maintain the desired 3D shape and architecture. In general, this means that the slurry should show pseudoplastic behavior with a yield stress that is high enough to prevent deformation of the printed structure under its own weight.³¹

Difficulties were encountered in our preliminary robocasting experiments to continuously extrude filaments from an aqueous paste composed of the Si_3N_4 powder, a commercial anionic polyelectrolyte dispersant, Darvan 821A (a solution of 40 wt. % ammonium polyacrylate) and a flocculating agent (ammonium nitrate), as reported in a previous study for a different commercial Si_3N_4 powder.²⁷ Presumably the negative surface charge of the Si_3N_4 particles and the highly negative charge of the anionic polyelectrolyte at basic pH values (7.8 to 8.5) used in that study inhibited adsorption of the polyelectrolyte on the particle surface. In general, Si_3N_4 powders produced by different manufacturers have different physical characteristics (e.g., surface area) and surface chemistry which can have a strong effect on colloidal and rheological properties.

The use of a cationic polyelectrolyte, PEI, in the present study allowed the development of a paste formulation that provided continuous robocasting of simple and complex structures without observable flaws. The addition of PEI to deionized water resulted in an increase in pH of the solution to highly basic values (~ 11.4), due to adsorption of hydrogen (or hydronium) ions.²⁹ At these pH values, the surface of the Si_3N_4 particles and the Y_2O_3 and Al_2O_3 particles used as sintering aids are negatively charged. As the surface of the particles and the PEI are oppositely charged, adsorption by electrostatic attraction is favored.

Lower molecular weight PEI is often better suited for use as a dispersant whereas higher molecular weight PEI can serve as both a dispersant and an effective binder.³¹ The use of a combination of 4.0 wt. % L-PEI and 4.0 wt. % H-PEI resulted in the formation of pastes with an optimal combination of viscosity and solids content. However, upon robocasting, the extruded filaments did not maintain their shape, particularly for articles having a complex shape or a porous grid-like architecture. The addition of HPMC vastly improved the ability to form parts continuously without observable flaws. HPMC can act as a viscosifying agent and its addition presumably altered the rheological response of the paste, preventing phase separation during extrusion and improving the ability of the as-formed structure to maintain its geometry.

Microstructure of debinded and fired parts

In general, the microstructure of the debinded (or green) parts provides a useful indication of their sinterability. Homogeneous random particle packing and pores of low coordination number (fine pores) are beneficial for sintering. SEM images of the surface and cross section of the extruded filaments after debinding (Fig. 5) indicate that these requirements were achieved to a large extent. Neighboring regions with markedly different packing density were apparently absent and the largest pores were smaller than 1 to 2 μm .

Based on the formulation given in Table I, the solids content of the paste used for robocasting was ~ 35 vol. %. Because of this low solids content, the parts showed a fairly large shrinkage of 27.8% during firing (sinter/HIP). However, despite the low solids content of the paste, the Si_3N_4 phase in both the macroporous grid-like parts and the solid

parts reached almost full density during sinter/HIP. In the sinter/HIP route (which avoids the use of an encapsulating glass or metal can), parts have to be sintered to closed porosity (total porosity less than 5 to 10%, depending on the particle packing homogeneity of the green part) for the HIP step to be effective in removing the remaining porosity. If open pores are present, the high gas pressure used in the HIP step would prevent them from shrinking. Consequently, despite the low solids content of the paste, the green parts experienced considerable densification. While the density of the parts was not measured after the sintering step, it is reasonable to assume that the parts were sintered to a porosity lower than 5 to 10%.

In addition to the nearly full density of the Si_3N_4 phase, there was no observable deformation of the filaments in the macroporous grid-like architecture or the external geometry of the fired parts (Fig. 3 and Fig. 6). Studies in the ceramic literature show that some green articles, particularly articles formed from fine particles, can be sintered to almost full density despite a low particle packing density (<40 to 50%).³¹ Homogeneous particle packing and fine pores in the green parts formed by robocasting in this study (Fig. 5) were presumably beneficial for uniform shrinkage and considerable densification without deformation of the fired parts.

Despite the ability to produce macroporous and solid parts composed of a dense Si_3N_4 phase which showed no observable distortion, an increase in the particle packing density of the green parts (while maintaining the homogeneous packing) would be useful. A higher particle packing density leads to a reduction in the shrinkage required to achieve a given density during firing, which is useful for better controlling the dimensions of the fabricated part, particularly in the production of large parts. This might be achieved by improved treatment of the starting powder (Si_3N_4 and sintering aids) prior to paste formulation. In the present study, a powder blend formed by mixing the as-received starting powders was used in the paste formulation. This powder blend was provided by Amedica Corporation and is typically used to form Si_3N_4 green articles by pressing. Although the powder blend was sieved to remove agglomerates larger than $\sim 100\text{ }\mu\text{m}$ in the present study, the use of additional treatments should be studied. The as-received Si_3N_4 powder should be attrition milled to break up agglomerates. Thereafter, the powder

should be attrition milled a second time with the sintering aids (Y_2O_3 and Al_2O_3 powders) to achieve a well-mixed powder free from large agglomerates.

Mechanical properties

Si_3N_4 can be produced with high flexural strength (>1 GPa) and fracture toughness of up to $\sim 10 \text{ MPa m}^{1/2}$ but this requires careful control of the size and amount of well-dispersed large elongated grains in a fine-grained matrix.⁵ The use of $\beta\text{-Si}_3\text{N}_4$ seed particles and controlled hot pressing conditions have been found to be useful in achieving a well-controlled grain distribution. Significantly lower flexural strength and fracture toughness are often obtained when the Si_3N_4 has an unregulated microstructure composed of a broad grain distribution. The flexural strength is also dependent on the present (or absence) of surface flaws. Typically, specimens used in flexural testing have their surfaces finished with diamond grinding to provide a controlled surface free from large flaws.

In the present study, the specimens were tested in the as-fabricated state and without surface grinding. This is because Si_3N_4 implants are typically used in the as-fabricated state (after sterilization) in spinal fusion applications. The fibrous surface morphology of the as-fabricated material has also been reported to endow the Si_3N_4 implants with antibacterial activity.⁹ Consequently, the flexural strength of the as-fabricated material provides a better approximation to the flexural strength of Si_3N_4 constructs that are implanted clinically. When compared to the flexural strength reported in some studies,⁵ the lower flexural strength of the solid specimens in the present study ($552 \pm 68 \text{ MPa}$) is presumably due to an unregulated grain distribution and a lack of surface machining. A standard sinter/HIP schedule without seed particles was used. As the specimens were tested in the as-fabricated state, their surfaces consisted of a random arrangement of protruding fibrous grains (Fig. 8c). The surface of these as-fabricated specimens can be approximated to a surface with a distribution of flaw sizes. It is well known that the strength of brittle materials varies inversely as the square root of the largest flaw size.

In general, the Si_3N_4 parts fabricated in the present study have strengths that are more than adequate for orthopedic applications coupled with a fibrous surface

morphology that is reported to be beneficial for antibacterial activity. The compressive and flexural strengths of human cortical bone are in the range 100 to 150 MPa. The flexural strength of the solid Si_3N_4 specimens (552 ± 68 MPa) is considerably higher than cortical bone. The compressive strength was too high to be measured with the available testing machine but, like ceramics in general, it is expected to be several times the flexural strength. Specimens with a porous grid-like architecture (porosity = 56.5%; pore width ~ 350 μm) showed a flexural strength (89 ± 11 MPa) comparable to human cortical bone. Macroporous Si_3N_4 implants with a gradient in porosity to mimic human cortical bone could provide flexural strengths that are higher than the porous grid-like parts created in the present study in addition to interconnected pores with the requisite size for bone infiltration.

Conclusions

An aqueous paste composed of Si_3N_4 , sintering additives and organic processing additives was developed for continuous robocasting of green parts with different geometry and architecture. Sintering followed by hot isostatic pressing (sinter/HIP) produced macroporous parts with a grid-like architecture and solid parts with an almost full dense Si_3N_4 phase (density 3.23 ± 0.02 g/cm^3) and a microstructure of fibrous grains typical of *in situ* toughened Si_3N_4 . Four-point bending tests of as-fabricated solid samples in the shape of beams showed a flexural strength of 552 ± 68 MPa. Samples with a macroporous grid-like architecture (porosity = 56.5%; pore width = 350 μm) showed a flexural strength of 89 ± 11 MPa. Together, the results indicate that robocasting combined with the sinter/HIP technique could provide a viable approach to create Si_3N_4 implants with anatomically relevant shapes and internal architectures for applications in orthopedic surgery.

Acknowledgements: This work was funded by Missouri University of Science and Technology, Center for Biomedical Science and Engineering, and the University of Missouri, Columbia.

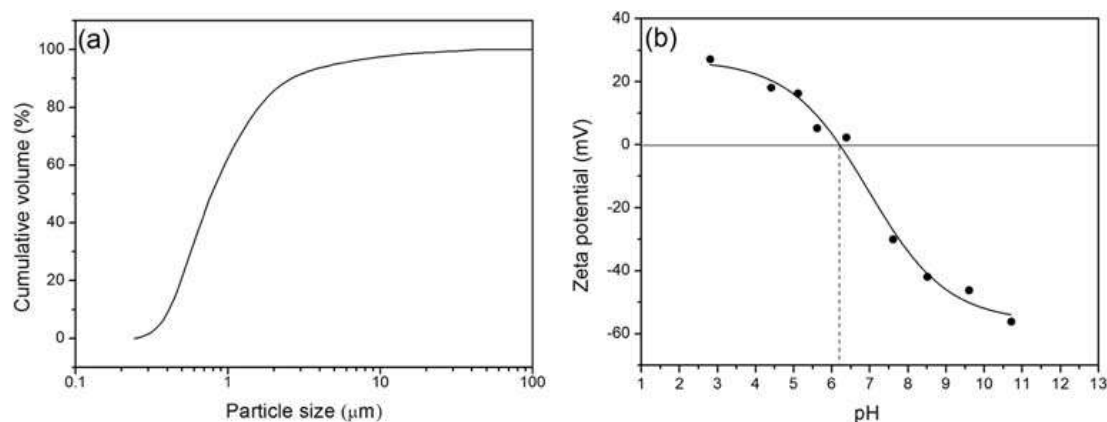
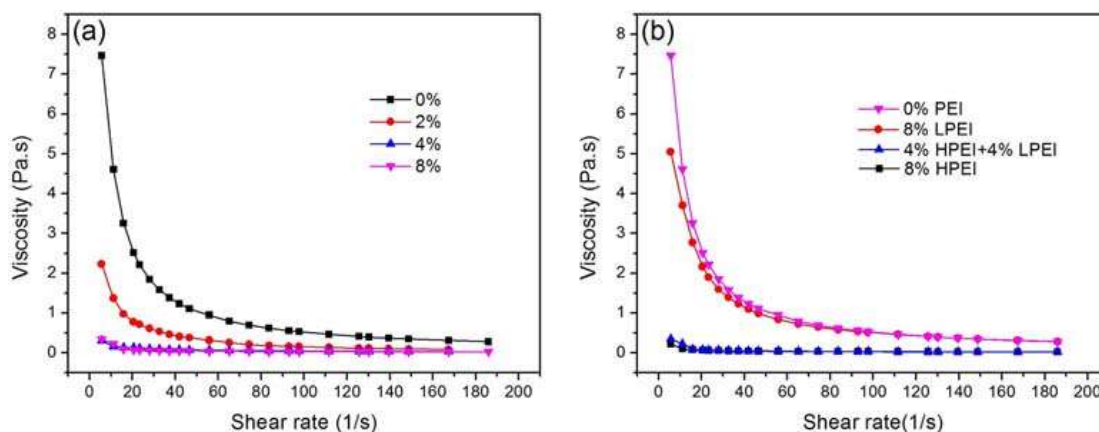
References

1. F. L. Riley, Silicon nitride and related materials, *J. Am. Ceram. Soc.*, 83, 245–65 (2000).
2. H. Klemm, Silicon nitride for high-temperature applications, *J. Am. Ceram. Soc.*, 93, 1501–22 (2010).
3. M. H. Bocanegra-Bernal and B. Matovic, Mechanical properties of silicon nitride-based ceramics and its use in structural applications at high temperatures, *Mater. Sci. Eng. A*, 527, 1314–38 (2010).
4. P. Sagalik, J. Dusza, and M. J. Hoffmann, Relationship between microstructure, toughening mechanisms, and fracture toughness of reinforced silicon nitride ceramics, *J. Am. Ceram. Soc.*, 78, 2619–24 (1995).
5. P. F. Becher, E. Y. Sun, K. P. Plunkett, K. B. Alexander, C.-H. Hsueh, H.T. Lin, S. B. Waters, C. G. Westmoreland, E.-S. Kang, K. Hirao, and M. E. Brito, Microstructural design of silicon nitride with improved toughness: I, effects of grain shape and size, *J. Am. Ceram. Soc.*, 81, 2821–30 (1998).
6. C. R. Howlett, E. McCartney, and W. Ching, The effect of silicon nitride ceramic on rabbit skeletal cells and tissue. An in vitro and in vivo investigation, *Clin. Orthop. Relat. Res.*, 244, 293–304 (1989).
7. B. Cappi, S. Neuss, J. Salber, R. Telle, R. Knuchel, and H. Fischer, Cytocompatibility of high strength non-oxide ceramics, *J. Biomed. Mater. Res. A*, 93, 67–76 (2010).
8. M. N. Rahaman, B. S. Bal, J. P. Garino, M. Ries, and A. Yao, Ceramics for prosthetic hip and knee joint replacement, *J. Am. Ceram. Soc.*, 90, 1965–88 (2007).
9. B. S. Bal and M. N. Rahaman, Orthopedic applications of silicon nitride ceramics, *Acta Biomater.*, 82, 2889–98 (2012).
10. B. J. McIntyre, B. S. Bal, M. N. Rahaman, J. Chevalier, and G. Pezzotti, Ceramics and ceramic coatings for total joint arthroplasty – a review, *J. Eur. Ceram. Soc.*, 25, 4327–69 (2015).
11. C. L. Quackenbush, K. French, and J. T. Neil, Fabrication of sinterable silicon nitride by injection molding, *Ceram. Eng. Sci. Proc.*, 3(1–2), Chap. 3 (1982).
12. A. J. Millan, M. I. Nieto, and R. Moreno, Aqueous injection moulding of silicon nitride, *J. Europ. Ceram. Soc.*, 20, 2661–6 (2000).
13. M. P. Albano and L. B. Garrido, Processing of concentrated aqueous silicon nitride slips by slip casting, *J. Am. Ceram. Soc.*, 81, 837–44 (1998).
14. S. Li, K. Sassa, and S. Asai, Preferred orientation of Si_3N_4 ceramics by slip casting in a high magnetic field, *J. Am. Ceram. Soc.*, 87, 1384–7 (2004).
15. T. Wan, T. Yao, H. Hu, Y. Xia, K. Zuo, and Y. Zheng, Fabrication of porous Si_3N_4 ceramics through a novel gelcasting method, *Mater. Lett.*, 133, 190–2 (2014).

16. J.-M. Wu, X.-Y. Zhang, and J.-L. Yang, Novel porous Si₃N₄ ceramics prepared by aqueous gelcasting using Si₃N₄ poly-hollow microspheres as pore-forming agent, *J. Eur. Ceram. Soc.*, 34, 1089–96 (2014).
17. J. Cesarano III, R. Segalman, and P. Calvert P, Robocasting provides moldless fabrication from slurry deposition, *Ceram. Ind.*, 148(4), 94–102 (1998).
18. J. A. Lewis, J. E. Smay, J. Stuecker, and J. Cesarano III, Direct ink writing of three-dimensional ceramic structures, *J. Am. Ceram. Soc.*, 89, 3599–3609 (2006).
19. E. Feilden, E. G.-T. Blanca, F. Giuliani, and L. Vandeperre, Robocasting of structural ceramic parts with hydrogel inks, *J. Eur. Ceram. Soc.*, 36, 2525–33 (2016).
20. K. Cai, B. Roman-Manso, J. E. Smay, J. Zhou, M. I. Osendi, M. Blemonte, and P. Miranzo, Geometrically complex silicon carbide structures fabricated by robocasting, *J. Am. Ceram. Soc.*, 95, 2660–6 (2012).
21. P. Miranda, A. Pajares, E. Saiz, A. P. Tomsia, and F. Guiberteau, Mechanical properties of calcium phosphate scaffolds fabricated by robocasting, *J. Biomed. Mater. Res. A*, 85, 218–27 (2008).
22. P. Miranda, E. Saiz, K. Gryn, and A. P. Tomsia, Sintering and robocasting of β -tricalcium phosphate scaffolds for orthopaedic applications, *Acta Biomater.*, 2, 457–66 (2006).
23. Y. Maazouz, E. B. Montufar, J. Guillem-Marti, I. Fleps, C. Ohman, C. Persson, and M. P. Ginebra, Robocasting of biomimetic hydroxyapatite scaffolds using self-setting inks, *J. Mater. Chem. B*, 2, 5378–86 (2014).
24. Q. Fu, E. Saiz, and A. P. Tomsia, Direct ink writing of highly porous and strong glass scaffolds for load-bearing bone defects repair and regeneration, *Acta Biomater.*, 7, 3547–54 (2011).
25. X. Liu, M. N. Rahaman, G. E. Hilmas, and B. S. Bal, Mechanical properties of bioactive glass (13-93) scaffolds fabricated by robotic deposition for structural bone repair, *Acta Biomater.*, 9, 7025–34 (2013).
26. W. Xiao, M. A. Zaeem, B. S. Bal, and M. N. Rahaman, Creation of bioactive glass (13–93) scaffolds for structural bone repair using a combined finite element modeling and rapid prototyping approach, *Mater. Sci. Eng. C*, 68, 651–62 (2016).
27. G. P. He, D. A. Hirschfeld, J. Cesarano III, and J. N. Stuecker, Robocasting and mechanical testing of aqueous silicon nitride slurries, Technical Report, Sandia National Laboratory, SAND2000-1493C (2000).
28. M. A. Janney, O. O. Omatete, C. A. Walls, S. A. Nunn, R. J. Ogle, and G. Westmoreland, Development of low-toxicity gelcasting systems, *J. Am. Ceram. Soc.*, 81, 581–91 (1998).
29. E. Poptoshev and P. M. Claesson, Forces between glass surfaces in aqueous polyethylenimine solutions, *Langmuir*, 18, 2590–4 (2002).
30. L. Bergstrom and R. J. Pugh, Interfacial characterization of silicon nitride powders, *J. Am. Ceram. Soc.*, 73, 103–9 (1989).
31. M. N. Rahaman, *Ceramic Processing*, CRC Press, Boca Raton, FL, 2007, Chap. 7.

Table I. Composition of slurry used in robocasting of Si_3N_4

Material	Composition (wt. %)
$\text{Si}_3\text{N}_4 + \text{Y}_2\text{O}_3 + \text{Al}_2\text{O}_3$	61.8
H-PEI (high molecular wt. PEI)	2.5
L-PEI (low molecular wt. PEI)	2.5
HPMC (hydroxypropyl methyl cellulose)	0.9
Deionized water	32.3

Fig. 1. (a) Particle size distribution and (b) zeta potential vs. pH for as-received Si_3N_4 powder (without sintering additives).Fig. 2. Viscosity vs. shear rate for aqueous suspensions composed of 20 vol. % Si_3N_4 particles and varying amounts of (a) high molecular weight polyethylenimine (H-PEI) and (b) a combination of H-PEI and low molecular weight PEI (L-PEI). The amount of PEI is expressed as a percentage of the weight of the Si_3N_4 powder.

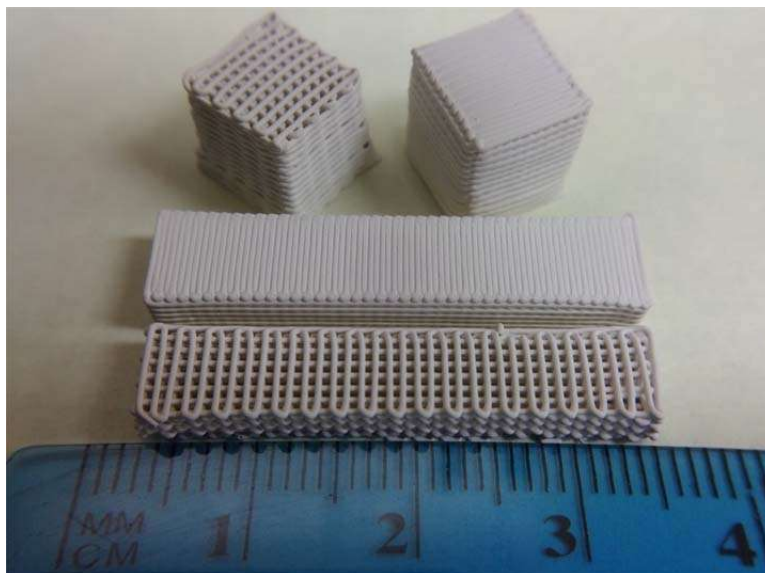


Fig. 3. Optical photographs of Si_3N_4 green parts with a porous grid-like architecture or a solid architecture and with the geometry of a cube or a beam.

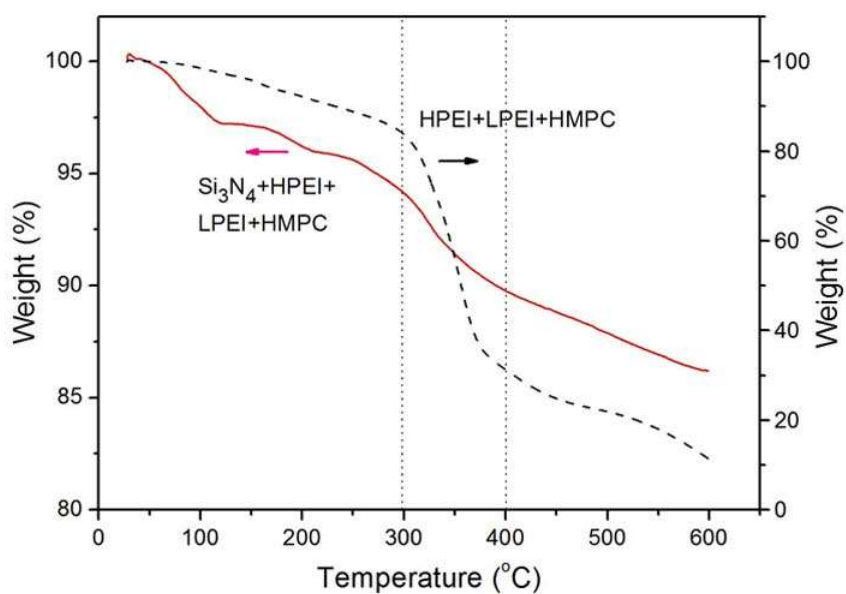


Fig. 4. Thermogravimetric analysis (TGA) curves for the binder system alone (4.0 wt. % H-PEI + 4.0 wt. % L-PEI + 1.5 wt. % HPMc based on the weight of the Si_3N_4 particles used in the robocasting paste) and the paste (binder system plus Si_3N_4 powder) used in the robocasting experiments. The samples were heated in air at 5 °C/min to 600 °C.

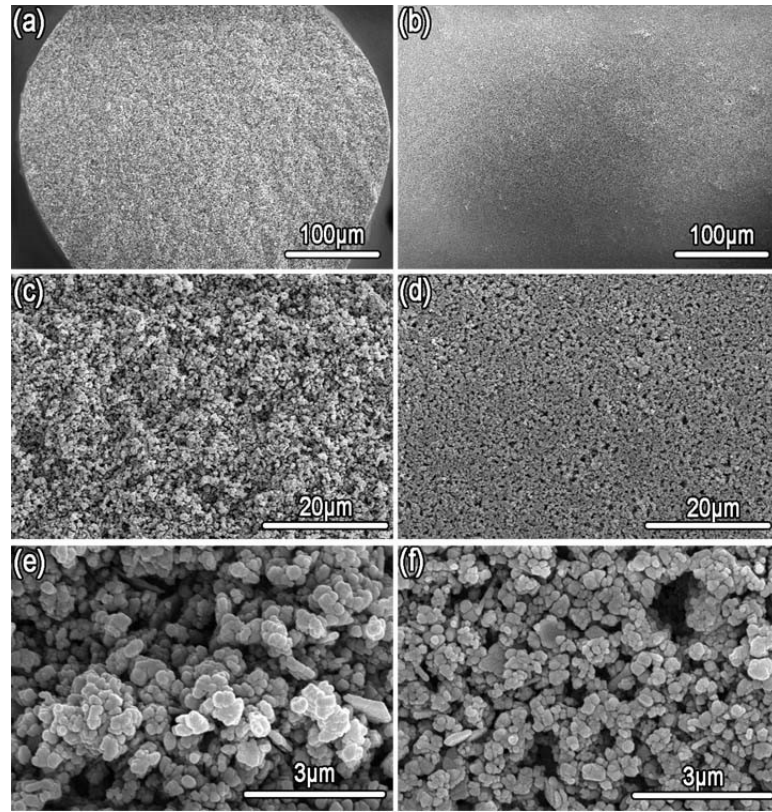


Fig. 5. SEM images of the filaments in debinded parts with a porous grid-like architecture. The fractured cross section (a, c, e) and surface (b, d, f) of the filaments are shown.

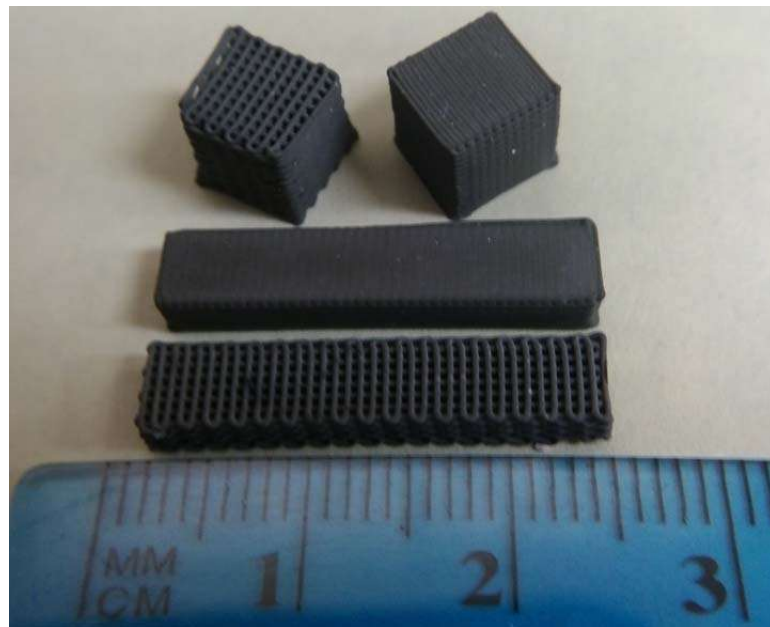


Fig. 6. Optical images of Si_3N_4 parts after sintering and hot isostatic pressing (sinter/HIP).

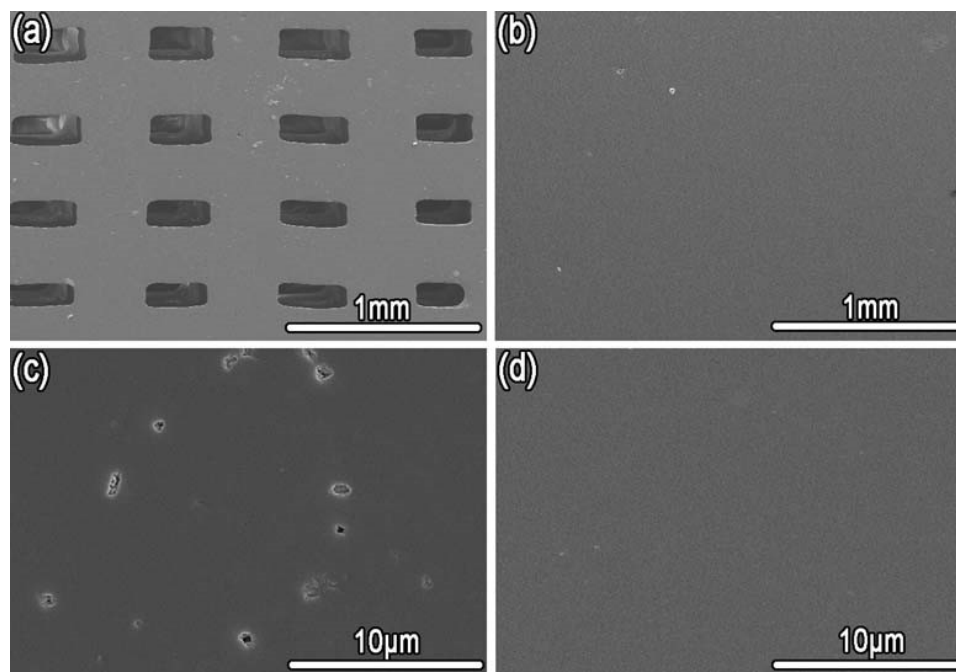


Fig. 7. SEM images of the polished cross-section of fired Si₃N₄ parts with a porous grid-like architecture (a, c) and with a solid architecture (b, d) at different magnifications.

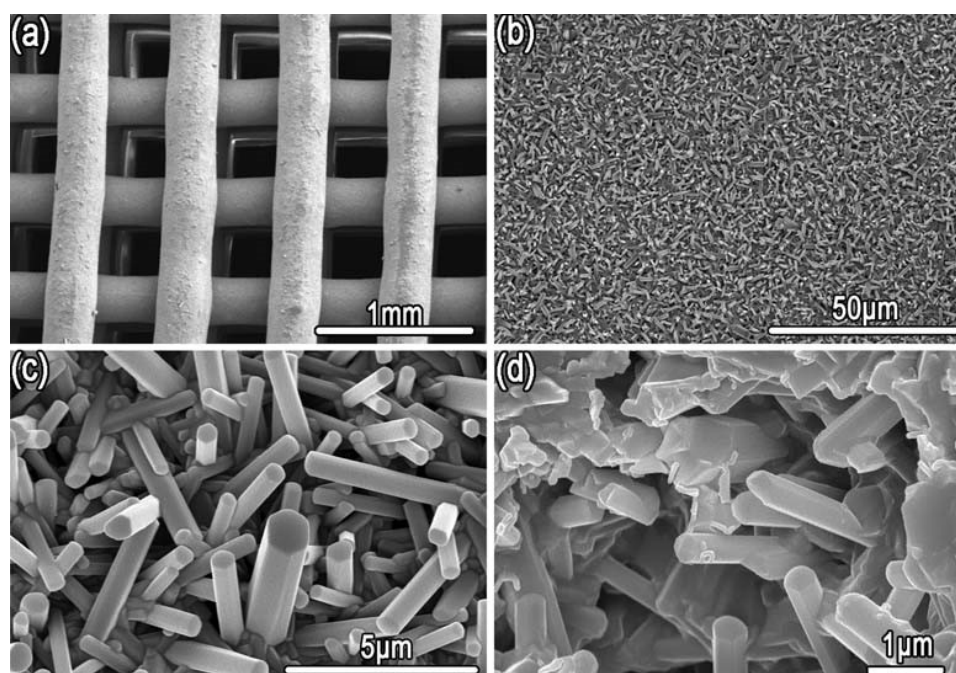


Fig. 8. SEM images of a fired Si₃N₄ part with a porous grid-like architecture showing (a) the filaments in the part, (b, c) the surface of a filament at lower and higher magnification, and (d) the fractured cross section of a filament.

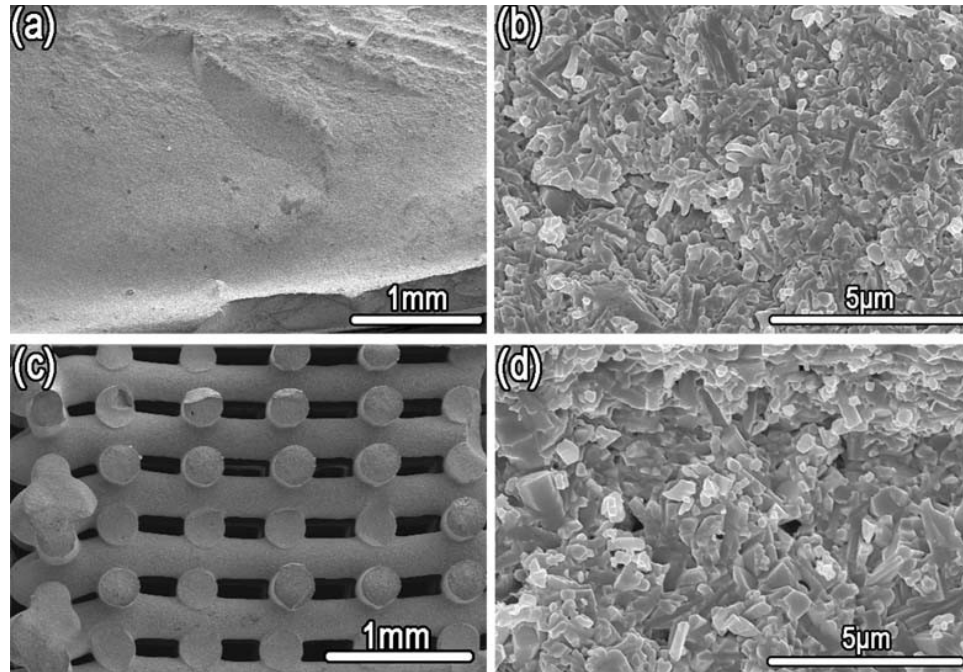


Fig. 9. SEM images of the fractured surface of fired parts with a solid architecture (a, b) and a porous grid-like architecture (c, d) after failure in four-point bending.

VITA

Wei Xiao was born in 1987 in Yiyang, Jiangxi, China. In August, 2004, he started his undergraduate education at Tongji University in Shanghai, China. After graduating with a B.S. degree in Materials Science and Engineering, Wei began his graduate study in August 2008 at Tongji University under the supervision of Dr. Wenhai Huang. He received his M.S. degree in Materials Science and Engineering in 2011.

Driven by his curiosity in the area of novel materials research, in June 2012, Wei started his Ph.D. study under the supervision of Dr. Mohamed N. Rahaman at Missouri University of Science and Technology, Rolla, Missouri, USA. He worked mainly on developing implants composed of bioactive materials for bone repair. His doctoral research resulted in 7 journal papers (5 published and two submitted), 4 of which he is the first author, 5 conference proceedings and 3 presentations at international conferences in the United States. In December 2016, he received his Ph.D. in Materials Science and Engineering from the Missouri University of Science and Technology, Rolla, Missouri, USA.